Spin Waves and Supercritical Motion in Superfluid ^{3}He

Sami Laine

University of Oulu Graduate School
University of Oulu
Faculty of Science
Nano and Molecular Systems Research Unit

Academic Dissertation to be presented with the assent of the Faculty of Science, University of Oulu, for public discussion in the Auditorium L10, on June 28th, 2019, at 12 o'clock noon.

REPORT SERIES IN PHYSICAL SCIENCES Report No. 127
OULU 2019 • UNIVERSITY OF OULU

Opponent
Dr. Mikhail Silaev, Department of Physics, Nanoscience Center,
University of Jyväskylä, Jyväskylä, Finland.

Reviewers
Dr. Sungkit Yip, Institute of Atomic and Molecular Sciences,
Academia Sinica, Taipei, Taiwan.

Prof. Dr. Nils Schopohl, Institute for Theoretical Physics,
Eberhard-Karls-Universität Tübingen, Tübingen, Germany.

Custos
Prof. Erkki Thuneberg, Department of Applied Physics,
Aalto University, Espoo, Finland.

ISBN 978-952-62-2292-9
ISBN 978-952-62-2293-6 (PDF)
ISSN 1239-4327
A. J. Mattilan Kirjapaino Oy
Kempele 2019

Abstract

Helium is the second most abundant element in the Universe. It is the only known substance that can exist in liquid state at absolute zero. There are two stable isotopes of helium, fermionic ^{3}He and bosonic ^{4}He. At sufficiently low temperatures, both isotopes undergo a phase transition into a superfluid state. These superfluids are usually characterised by their ability to flow without resistance, but this is by no means their only remarkable property.

In this thesis, we study theoretically superfluid ^{3}He. The work consists of two separate projects. First, we study the effect of a quantised vortex line to spin dynamics of the superfluid. We find that the interplay between the vortex and the magnetisation of the liquid generates spin waves, dissipating energy. We find that the theoretically predicted energy dissipation is in agreement with experimental data, implying that spin-wave radiation can be an important mechanism of magnetic relaxation in superfluid ^{3}He.

Second, we study the drag force acting on an object moving through zero-temperature superfluid at a constant velocity. The drag arises if momentum is transferred from the object to the fluid. At low velocities, no such mechanism exist and thus the drag vanishes. If the velocity exceeds the Landau velocity v_L, it becomes possible for the object to create quasiparticle excitations that could, in principle, transfer momentum away from the object. Thus, v_L has been generally assumed to be the critical velocity, that is, the velocity above which the drag force starts to increase rapidly towards the normal-state value. We find that this is not necessarily the case. Objects much larger than the superfluid coherence length modify the superfluid flow field around them. The spatial variation of the flow field can shield the object, preventing quasiparticles from transferring momentum away from the object. This leads to a critical velocity greater than v_L.

Keywords: Superfluid ^{3}He, Vortices, Spin waves, Landau velocity, Critical velocity

Acknowledgments

The work presented here was carried out in the group of theoretical physics at the University of Oulu. The research was funded by the Academy of Finland, the Jenny and Antti Wihuri Foundation, and the Vilho, Yrjö and Kalle Väisälä Foundation of the Finnish Academy of Science and Letters.

I am deeply grateful to my principal supervisor, professor Erkki Thuneberg, for introducing me to the fascinating field of superfluid ^{3}He, sharing his vast knowledge on the subject and physics in general, and providing guidance whenever needed. I am equally grateful to my second supervisor, docent Jani Tuorila, for providing guidance on both physics and practical matters throughout my doctoral studies.

I would like to thank professor Matti Alatalo for acting as the chair of the follow-up group and as the degree supervisor, as well as dealing with various other administrative tasks. I would also like to thank the other members of the follow-up group, docent Saana-Maija Huttula and professor Ville-Veikko Telkki, for their time and effort. I want to express my gratitude to professor Nils Schopohl and professor Sungkit Yip for their work as the pre-examiners of this thesis.

I want to thank my fellow doctoral students Juri Kuorelahti and Iivari Pietikäinen for, together with Jani, making the past few years an unforgettable journey. I wish to thank docent Matti Silveri for many a fruitful discussion, and the personnel of the theoretical physics group for creating a pleasant environment to work in.

Last but not least, I want to thank my family and friends for their unwavering support.

Kempele, May 2019 Sami Laine

List of original publications

The present thesis contains an introductory part and the following publications which will be referred to in the text by their Roman numerals.

I S. M. Laine and E. V. Thuneberg, *Calculation of Leggett–Takagi Relaxation in Vortices of Superfluid* ^{3}*He-B*, J. Low Temp. Phys. **183**, 222 (2016).

II J. A. Kuorelahti, S. M. Laine, and E. V. Thuneberg, *Models for supercritical motion in a superfluid Fermi liquid*, Phys. Rev. B **98**, 144512 (2018).

III S. M. Laine and E. V. Thuneberg, *Spin-wave radiation from vortices in* ^{3}*He-B*, Phys. Rev. B **98**, 174516 (2018).

The author has had a central role in all three publications. He has done the major part of the analytical work in Pubs. I and III, a large part of the analytical work in Pub. II, contributed to the numerical work in Pub. II, written the initial drafts of Pubs. I and III, and contributed to writing of all three publications.

Contents

Chapter 1

Introduction

For decades, liquid ^{3}He has served as a playground for physicists to study peculiarities of quantum many body systems. Due to the light mass of ^{3}He atoms, their quantum mechanical zero-point motion is so significant that the liquid does not solidify, not even at zero temperature, provided that the external pressure is sufficiently low ($p \lesssim 34$ bar) [1]. This makes low-temperature ^{3}He a paradigm of fermionic quantum liquid.

Even though ^{3}He atoms interact strongly with each other, at sufficiently low temperatures ($T \lesssim 100$ mK) liquid ^{3}He behaves like a system of weakly interacting *quasiparticles*. The quasiparticles are particle-like objects whose properties may differ from those of the bare ^{3}He atoms. For example, the effective mass m^* of a quasiparticle is larger than the mass m of a ^{3}He atom by a factor of ~ 5, depending on pressure. Such behaviour of ^{3}He is successfully described by the Fermi liquid theory [2, 3], originally developed by Lev Landau [4, 5].

At even lower temperatures ($T \lesssim 1$ mK), a curious phenomenon occurs: the quasiparticles start to form pairs. These so-called *Cooper pairs*, named after Leon Cooper who first studied the problem [6], comprise two fermions near the Fermi surface and are thus bosons. Unlike the fermionic quasiparticles by themselves, the bosonic Cooper pairs can condense into the same quantum state, a phenomenon similar to Bose–Einstein condensation [7]. This *condensate* forms a superfluid with numerous interesting properties, such as zero viscosity, successfully described by the Bardeen–Cooper–Schrieffer (BCS) theory [8, 1], which was originally developed to explain superconductivity in metals [9, 10]. Since the formation of Cooper pairs is energetically favourable, breaking a pair costs energy. This means that the spectrum of elementary excitations has an energy gap.

Cooper pairs in conventional superconductors form in a state with orbital angular momentum quantum number $l = 0$ and spin quantum number $s = 0$, meaning that the pairs are structureless [11]. In superfluid ^{3}He, however, the pairing state is a p-wave ($l = 1$) spin triplet ($s = 1$), and thus the pairs have a more complicated internal structure [11]. To describe the state of a pair, one needs $(2l + 1) \times (2s + 1) = 9$ complex parameters. A convenient way to write the state vector $|\Psi\rangle$ of the pair is to use the basis states

$$|b_1^{(\lambda)}\rangle = \frac{-|\lambda_z = 1\rangle + |\lambda_z = -1\rangle}{\sqrt{2}}, \tag{1.1}$$

$$|b_2^{(\lambda)}\rangle = i\frac{|\lambda_z = 1\rangle + |\lambda_z = -1\rangle}{\sqrt{2}}, \tag{1.2}$$

$$|b_3^{(\lambda)}\rangle = |\lambda_z = 0\rangle \tag{1.3}$$

in both the orbital space ($\lambda =$ "l") and the spin space ($\lambda =$ "s"). Here, the states $|\lambda_z = 0, \pm 1\rangle$ are the standard eigenstates of the (arbitrarily chosen) z component of the angular momentum. The tensor product states $|b_i^{(s)}\rangle \otimes |b_j^{(l)}\rangle$ form a basis for the state vector, and we can write

$$|\Psi\rangle = \sum_{i=1}^{3}\sum_{j=1}^{3} A_{ij}|b_i^{(s)}\rangle \otimes |b_j^{(l)}\rangle. \tag{1.4}$$

The coefficients A_{ij} define a 3×3 matrix A, which is commonly used as an order parameter in the theory of superfluidity [1]. In contrast to Eq. (1.4), the pair wave function in a conventional superconductor is simply proportional to the state $|s = 0, s_z = 0\rangle \otimes |l = 0, l_z = 0\rangle$. From the definition above, one can show that the tuple $(A_{1j}, A_{2j}, A_{3j})^T$, with $j = 1, 2, 3$, transforms as a vector under rotations in the spin space. Similarly, the tuple $(A_{i1}, A_{i2}, A_{i3})^T$, with $i = 1, 2, 3$, transforms as a vector under rotations in the orbital space. A more formal definition of A in the language of quantum field theory can be found, for example, in Refs. [1, 12]. For a detailed discussion on the similarities between superfluid ^{3}He and particle physics, see Ref. [12].

Due to the nontrivial internal structure of the Cooper pairs, several superfluid phases may exist in ^{3}He, each with a different order parameter A. In the absence of external fields, there are two stable phases in bulk ^{3}He, the A phase [13, 14, 15] and the B phase [16, 15]. Of these two, the B phase is more common; the A phase is only stable near the superfluid transition temperature T_c at relatively high pressures ($p \gtrsim 20$ bar). For details on the bulk phases and their phase diagram, see Ref. [1].

In addition to the bulk phases A and B, more phases can be stabilised by means of an external influence. If a magnetic field is applied, a phase called A$_1$ appears [17, 18]. Walls change the structure of the order parameter by making it inhomogeneous [19, 1, 20]. If the superfluid flows, the order parameter is suppressed along the flow [21, 22, 23]. Impurities such as aerogel also affect the superfluid state [24, 25, 26]. Particularly interesting are anisotropic aerogels which stabilise the polar phase [27, 28, 29, 26]. If the container holding the superfluid is rotated, an array of quantised vortices is formed [30, 31, 1]. There are five different types of vortices in the A phase [31]. In the B phase, there are two stable vortex structures [32, 33, 31]: the axisymmetric A-phase-core vortex, the core of which resembles the A phase [34], and the non-axisymmetric double-core vortex, the core of which is split into two half cores [35]. Of these two, the double-core vortex occupies the greater part of the T-p phase diagram [31]. In the polar phase, a half-quantum vortex has been observed [36].

Although our work is purely theoretical, it has been inspired by experiments. Thus, a few words about experimental methods are in order. Ever since the discovery of the superfluid phase transition in ^{3}He, nuclear magnetic resonance (NMR) has played an important role in experimental studies of the superfluid phases. This is due to the fact that the magnetic properties of the various phases differ not only from those of the normal phase but also from each other. Two methods are traditionally used. In continuous-wave NMR, one uses a time-dependent magnetic field to drive the magnetisation of the sample and studies the power absorption as a function of the drive frequency. Quantities of interest are the positions and the widths of the resonance peaks, and the amount of absorption. In pulsed NMR, one uses a time-dependent magnetic field to perturb the magnetisation of the sample from the equilibrium, turns the perturbing field off, and observes the free time evolution of the magnetisation (known as free induction decay). This provides information on magnetic relaxation phenomena.

Another widely used experimental method is to study motion of various objects immersed in the liquid. This provides information on hydrodynamic properties of the liquid, which are directly related to superfluidity. The object can be charged, such as an ion or an electron, in which case one can move it using an electric field. In such case, the studied quantity is the mobility of the object, that is, the relation between the velocity of the object and the applied electric field. The object can also be electrically neutral. Some examples are vibrating wires, torsional oscillators, walls, and pendula. Two methods are traditionally used. The object can either be driven by an external force, in which case one measures the velocity response of the object to the applied force as a function of the drive frequency (cf. continuous-wave NMR), or free, in which case one first sets the object in motion, and then observes damping of the motion (cf. pulsed NMR). For details on the experimental methods, see Refs. [1, 37, 38, 39] and references therein.

The work reported in this thesis consists of two separate projects. In the first project, we study magnetic relaxation caused by vortices in ^{3}He-B under uniformly precessing magnetisation, see Pubs. I and III, and Chap. 2. Experimentally, magnetic relaxation measurements at large tipping angles of the magnetisation provide a more sensitive tool to distinguish between the two vortex core structures than frequency shift measurements at small tipping angles [40, 41]. Theoretical understanding of the effect of vortices on the relaxation has, however, been incomplete. Our study shows that one needs to take into account a previously neglected relaxation mechanism: generation of *spin waves*. Under precessing magnetisation, the interaction between the order parameter and the magnetisation leads to oscillations of the order parameter near the vortex. These oscillations give rise to waves of magnetisation, that is, spin waves. The phenomenon is similar to an oscillating charge emitting electromagnetic radiation. The generation of spin waves dissipates energy. We find that the predicted dissipation is in good qualitative agreement with experiments. This leads to the conclusion that generation of spin waves is a significant relaxation mechanism for vortices.

The second project concerns supercritical motion in the B phase at zero temperature, see Pub. II and Chap. 3. Until recently, the prevailing assumption has been that once an object moving in the superfluid reaches the so-called Landau velocity v_L [42], the force it experiences starts to rise rapidly towards the normal-state value. In other words, Landau velocity is considered to be the *critical velocity* v_c for the object, that is, the velocity above which dissipationless (or low-dissipation if $T > 0$) motion is not possible. This seems plausible since v_L is the velocity above which the object can create elementary excitations (quasiparticles) that should be able to transfer momentum away from the object. Other dissipation mechanisms, such as vortex formation, can set in at lower velocities, decreasing the critical velocity from the Landau velocity, but v_L has been thought to be the upper limit for v_c. A recent experiment by Bradley et al. [43] challenges this view. They observe no sudden onset of drag force at v_L for a macroscopic wire moving at constant velocity in low-temperature ^{3}He-B, only a small, continuous, gradually increasing force up to velocities $\sim 2.5v_L$. We find that v_L is indeed the critical velocity for a microscopic object of size much less than the superfluid coherence length ξ_0, but things get more complicated when the object is macroscopic, that is, much larger than ξ_0. This is because a macroscopic object moving in the superfluid results in a spatially varying flow field around the object. The flow field can then shield the object, preventing the created elementary excitations from leaving the vicinity of the object. This suppresses momentum transfer from the object to the fluid, and thus increases the critical velocity.

In this thesis, I shall review and supplement the main results of Pubs. I, II, and III. Chapter 2 concerns spin dynamics of ^{3}He-B in the presence of a single vortex line. Chapter 3 concerns motion in zero-temperature ^{3}He-B at velocities of the order of v_L. In Chap. 4, a short summary of the results is given.

Chapter 2

Spin dynamics of vortices in ^{3}He-B

In this chapter, we study spin dynamics of the B phase of superfluid ^{3}He in the presence of a single vortex line. In Sec. 2.1, we recall some static properties of ^{3}He-B and vortices therein. In Sec. 2.2, we introduce the Leggett theory of spin dynamics in Lagrangian formulation. In Sec. 2.3, we discuss spin dynamics of bulk ^{3}He-B. In Sec. 2.4, we apply the Leggett theory to study spin dynamics of a vortex line under uniformly precessing magnetisation. We solve the equations of spin dynamics in two different approximations, and find that the vortex radiates spin waves. These waves carry energy, causing dissipation in the system. We compare the predicted dissipation to experimental observations, and find a good agreement between the two.

2.1 Static properties of the B phase

Let us first recall some static properties of the B phase. We use the hydrostatic theory [44], which is valid at all temperatures, but restricted to length scales much larger than the superfluid coherence length $\xi_0 \sim 10$ nm, as well as to weak external fields. This means, among other things, that the detailed structure of the vortex core cannot be studied within the hydrostatic theory since the core radius is of the order of ξ_0. We can, however, study the structure of the vortex farther away from the core by using the (numerically) known core structure as a boundary condition, as we show below.

2.1.1 Hydrostatic theory

The order parameter of the B phase is given by [44, 8, 1]

$$\mathsf{A} = e^{i\phi}\Delta_B \mathsf{R}(\boldsymbol{\theta}), \tag{2.1}$$

where ϕ is the phase of the order parameter, Δ_B is the magnitude of the superfluid energy gap, and $\mathsf{R}(\boldsymbol{\theta})$ is a rotation matrix which describes a rotation by the angle

$\theta = |\boldsymbol{\theta}|$ around the axis $\hat{\boldsymbol{\theta}} = \boldsymbol{\theta}/\theta$. The form of the order parameter is determined by the superfluid condensation energy, which also determines the magnitude of Δ_B. The phase ϕ and the rotation matrix R are, however, not constrained by the condensation energy. These so-called soft variables are the subjects of study in the hydrostatic theory. In general, ϕ and R can depend on position, but the gap Δ_B is constant.

The phase ϕ is related to the superfluid velocity $\boldsymbol{v}_s$ by [44]

$$\boldsymbol{v}_s = \frac{\hbar}{2m}\boldsymbol{\nabla}\phi, \tag{2.2}$$

where $\hbar$ is the reduced Planck's constant and m is the mass of a ^{3}He atom. In the absence of external fields, the mass current density is proportional to $\boldsymbol{v}_s$. Conservation of mass then implies $\boldsymbol{\nabla}\cdot\boldsymbol{v}_s = 0$, or [44]

$$\nabla^2\phi = 0, \tag{2.3}$$

meaning that the phase ϕ can be solved from the Laplace equation. External fields have only a small effect, which can be neglected in the first approximation.

The rotation matrix $\mathsf{R}(\boldsymbol{\theta})$ is affected by a number of energy terms arising from different sources. Each of the energies is small compared to the condensation energy, and thus the explicit form (2.1) of the order parameter is not altered, only $\boldsymbol{\theta}$. The free energy associated with R can be written as

$$F = \int_V d^3r f, \tag{2.4}$$

where $f = f(\mathsf{R})$ is the free energy density and V is the region of interest. The largest contributions to f are given by the dipole energy [44]

$$f_D = \lambda_D(R_{ii}R_{jj} + R_{ij}R_{ji}) = 4\lambda_D\cos\theta(1 + 2\cos\theta), \tag{2.5}$$

which originates from the dipole-dipole interaction between the ^{3}He atoms, and the gradient energy [44]

$$f_G = \lambda_{G1}\frac{\partial R_{ki}}{\partial r_i}\frac{\partial R_{kj}}{\partial r_j} + \lambda_{G2}\frac{\partial R_{ki}}{\partial r_j}\frac{\partial R_{ki}}{\partial r_j}, \tag{2.6}$$

which is caused by inhomogeneity of the order parameter. Here, λ_D is the dipole coupling parameter, while λ_{G1} and λ_{G2} are the gradient coupling parameters. They depend on temperature and pressure. In addition, R_{ij} and r_i are the components of the rotation matrix R and the position vector $\boldsymbol{r}$, respectively, in some fixed Cartesian coordinate system. The indices i, j, and k range from 1 to 3, and summation over repeated indices is implied. In calculating the second equality in Eq. (2.5), we have used the formula [45]

$$R_{ij}(\boldsymbol{\theta}) = \cos\theta\delta_{ij} + (1-\cos\theta)\hat{\theta}_i\hat{\theta}_j - \sin\theta\varepsilon_{ijk}\hat{\theta}_k. \tag{2.7}$$

Equation (2.5) shows that the dipole energy depends only on the rotation angle θ, not on the direction $\hat{\boldsymbol{\theta}}$ of the rotation axis. If the system is homogeneous, θ can be determined by minimising the dipole energy with respect to θ. This yields $\theta = \theta_L$ (or $\theta = 2\pi - \theta_L$, but this is equivalent to a rotation by θ_L about the axis $-\hat{\boldsymbol{\theta}}$), where

$$\theta_L = \arccos(-1/4) \approx 104^\circ \tag{2.8}$$

is the so-called Leggett angle.

The gradient energy and the dipole energy define a characteristic length scale of the system, known as the dipole length $\xi_D = \sqrt{\lambda_{G2}/\lambda_D} \sim 10\ \mu\text{m}$. This is the shortest length scale at which the rotation angle θ can vary in space. More rapid variations of θ would cost too much gradient energy in relation to the dipole energy.

In addition to f_D and f_G, there are a number of smaller contributions to f stemming from interplay between the order parameter and, for example, external magnetic field, flow field, and walls immersed in the fluid. These determine how the rotation axis $\hat{\boldsymbol{\theta}}$ varies in space (known as the texture). There is a characteristic length scale related to each of these energies. Since the energies are small compared to the dipole energy, the characteristic lengths are long compared to ξ_D. The shortest of these defines the shortest length scale at which $\hat{\boldsymbol{\theta}}$ can vary.

2.1.2 Vortices in the B phase

Let us consider a static vortex line in the B phase. We define a Cartesian coordinate system with basis vectors $\hat{\boldsymbol{x}}$, $\hat{\boldsymbol{y}}$, and $\hat{\boldsymbol{z}}$. We assume that the z axis coincides with the vortex axis. The external magnetic field $\boldsymbol{B}$ fixes the direction of the x axis (and therefore also the direction of the y axis, since $\hat{\boldsymbol{z}}$ is already fixed) by $\hat{\boldsymbol{B}} = \cos\eta\hat{\boldsymbol{z}} + \sin\eta\hat{\boldsymbol{x}}$. Here, η is the angle between the vortex axis and the magnetic field. Recall that there are two stable vortex structures in the B phase. Since the double-core vortex is asymmetric, we need to specify its orientation in the xy plane. This is done using the anisotropy vector $\hat{\boldsymbol{b}} = \cos\zeta\hat{\boldsymbol{y}} - \sin\zeta\hat{\boldsymbol{x}}$, which points from one of the half cores to the other. The A-phase-core vortex is symmetric, and thus one cannot distinguish its orientation in the xy plane. The definitions of the angles η and ζ are shown in Fig. 2.2. We shall also use the standard cylindrical coordinates (r, φ, z), where r measures distance from the z axis and φ is the azimuthal angle in the xy plane, measured anticlockwise from the x axis. The standard basis vectors in the cylindrical coordinate system are $\hat{\boldsymbol{r}} = \cos\varphi\hat{\boldsymbol{x}} + \sin\varphi\hat{\boldsymbol{y}}$, $\hat{\boldsymbol{\varphi}} = -\sin\varphi\hat{\boldsymbol{x}} + \cos\varphi\hat{\boldsymbol{y}}$, and $\hat{\boldsymbol{z}}$.

The order parameter of a vortex line can be written as [35]

$$\mathsf{A}_v = e^{i\varphi}\Delta_B \mathsf{R}(\boldsymbol{\theta}_B) \cdot \tilde{\mathsf{A}}_v. \tag{2.9}$$

Here, Δ_B is the bulk energy gap of the B phase and $\mathsf{R}(\boldsymbol{\theta}_B)$ is a rotation by $\boldsymbol{\theta}_B$. The rotation vector $\boldsymbol{\theta}_B$ is determined by the bulk. We can assume that it is spatially constant: First of all, the dipole energy fixes the magnitude θ_B to θ_L in the bulk, and a single vortex line cannot change this. Secondly, while the orientation $\hat{\boldsymbol{\theta}}_B$ may vary in space due to several different effects, the length scale of this variation is so large that, at least within a few dipole lengths from the core, $\hat{\boldsymbol{\theta}}_B$ is essentially constant.

The matrix $\tilde{\mathsf{A}}_v$ differs significantly from a rotation matrix in the core region of size $\sim \xi_0$. This means that we cannot use the hydrostatic theory of the B phase to study the core. Instead, one has to rely on more complex numerical calculations using either the Ginzburg-Landau theory [35] or the quasiclassical theory [46, 47]. Moving away from the core, the numerical calculations show that $\tilde{\mathsf{A}}_v$ behaves as [47]

$$\tilde{\mathsf{A}}_v = \mathsf{R}(\boldsymbol{\theta}_v) + \mathcal{O}(r^{-2}), \tag{2.10}$$

where $\mathsf{R}(\boldsymbol{\theta}_v)$ is a small rotation by an angle $|\boldsymbol{\theta}_v| \propto r^{-1}$ about an axis $\hat{\boldsymbol{\theta}}_v$, with $\hat{\boldsymbol{\theta}}_v \cdot \hat{\boldsymbol{z}} = 0$. This means that we can approximate the order parameter of the vortex line in the hydrostatic region $r \gg \xi_0$ by a B phase order parameter,

$$\mathsf{A}_v \approx e^{i\varphi} \Delta_B \mathsf{R}(\boldsymbol{\theta}_B) \mathsf{R}(\boldsymbol{\theta}_v), \tag{2.11}$$

and use the numerical solution as a boundary condition for $\boldsymbol{\theta}_v$. Note that the total rotation is now a combination of two rotations, one caused by the vortex and the other by the bulk. Equation (2.11) shows that the superfluid velocity far from the core is given by $\boldsymbol{v}_s = (\hbar/2m)\boldsymbol{\nabla}\varphi = (\hbar/2mr)\hat{\boldsymbol{\varphi}}$. Thus, the flow is around the core, as expected. Near the core, the flow pattern is more complicated due to the intricate form of $\tilde{\mathsf{A}}_v$.

In order to determine $\boldsymbol{\theta}_v$, we need to minimise the hydrostatic free energy (2.4). As we discussed earlier, the most important contributions to f are the dipole energy (2.5) and the gradient energy (2.6). Expanded to second order in small quantities $|\boldsymbol{\theta}_v|$ and $|\boldsymbol{\nabla}\boldsymbol{\theta}_v|$, these are given by

$$f_D \approx -\frac{\lambda_D}{2} + \frac{15}{2}\lambda_D(\hat{\boldsymbol{\theta}}_B \cdot \boldsymbol{\theta}_v)^2 \tag{2.12}$$

and

$$f_G \approx 2\lambda_{G2}\left[(1+c)\frac{\partial \theta_{v,k}}{\partial r_i}\frac{\partial \theta_{v,k}}{\partial r_i} - c\frac{\partial \theta_{v,k}}{\partial r_i}\frac{\partial \theta_{v,i}}{\partial r_k}\right]. \tag{2.13}$$

The coefficient

$$c = \frac{\lambda_{G1}}{2\lambda_{G2}} \tag{2.14}$$

is of the order of unity. In fact, $c = 1$ if we assume that the antisymmetric Fermi liquid parameters F_1^a and F_3^a vanish [44].

Let us first consider the region $\xi_0 \ll r \ll \xi_D$, where the hydrostatic theory can be used but the distance from the vortex core is still much less than the dipole length. In this region, the dipole energy cannot affect $\boldsymbol{\theta}_v$ significantly, and it is therefore sufficient to minimise the gradient energy. This leads to the partial differential equation

$$(1+c)\nabla^2\boldsymbol{\theta}_v - c\boldsymbol{\nabla}(\boldsymbol{\nabla} \cdot \boldsymbol{\theta}_v) = 0. \tag{2.15}$$

Based on the numerical structure of the vortex core, we seek a solution of the form $\boldsymbol{\theta}_v(r,\varphi,z) = r^{-1}[\theta_r(\varphi)\hat{\boldsymbol{r}} + \theta_\varphi(\varphi)\hat{\boldsymbol{\varphi}}]$. Substituting this ansatz into Eq. (2.15) yields

$$\begin{aligned}\boldsymbol{\theta}_v &= r^{-1}\left(A_1 + A_2\sin\varphi\cos\varphi + A_4\sin^2\varphi\right)\hat{\boldsymbol{r}} \\ &\quad + r^{-1}(1+c)\left(A_3 + A_4\sin\varphi\cos\varphi - A_2\sin^2\varphi\right)\hat{\boldsymbol{\varphi}},\end{aligned} \tag{2.16}$$

where A_i are adjustable parameters. Using symmetries of the vortices, some of these can be eliminated. The solution for the A-phase-core vortex is given by [48]

$$\boldsymbol{\theta}_v(r,\varphi) = (C_1/r)\hat{\boldsymbol{\varphi}}, \tag{2.17}$$

where C_1 is an adjustable parameter. The double-core vortex is less symmetric. In this case, the solution is given by [47]

$$\begin{aligned}\boldsymbol{\theta}_v(r,\varphi) = {}& \frac{(C_1 - C_2)\sin[2(\varphi-\zeta)]}{2(1+c)r}\hat{\boldsymbol{r}} \\ &+ \frac{(C_1 + C_2) + (C_1 - C_2)\cos[2(\varphi-\zeta)]}{2r}\hat{\boldsymbol{\varphi}}.\end{aligned} \tag{2.18}$$

Here, C_1 and C_2 are adjustable parameters. The orientation of the double-core vortex is determined by the external magnetic field. The preferred orientation in a tilted magnetic field ($\eta > 0$) is $\zeta = \pm\pi/2$ [35]. Note that Eq. (2.17) is a special case of Eq. (2.18) with $C_2 = C_1$. Thus, we can use Eq. (2.18) to discuss both types of vortices.

The parameters C_1 and C_2 can be determined by fitting the order parameter to the numerical solution of the vortex core. As already mentioned, $C_2 = C_1$ for the A-phase-core vortex. In the case of the double-core vortex, $C_1 \gg C_2$. It is convenient to measure the parameters C_i in units of

$$R_0 = (1 + F_1^s/3)\xi_0. \tag{2.19}$$

Here, F_1^s is the first symmetric Fermi liquid parameter, related to the effective mass of the quasiparticle by $m^*/m = 1 + F_1^s/3$. For example, numerical calculations [47] predict that $C_1 = C_2 = 1.33R_0$ for the A-phase-core vortex and $C_1 = 3.00R_0$, $C_2 = 0.08R_0$ for the double-core vortex at $T = 0.6T_c$, $p = 29.3$ bar, and $c = 1$. Equation (2.18) shows that the magnitude of $\boldsymbol{\theta}_v$ is proportional to R_0/r, which is small if $r \gg \xi_0$. The bulk order parameter is thus only slightly modified by the vortex in the hydrostatic region.

Farther away from the core, we need to take into account also the dipole energy. Minimising the free energy leads to the partial differential equation

$$(1+c)\nabla^2\boldsymbol{\theta}_v - c\boldsymbol{\nabla}(\boldsymbol{\nabla}\cdot\boldsymbol{\theta}_v) - \frac{15}{4}\xi_D^{-2}\hat{\boldsymbol{\theta}}_B(\hat{\boldsymbol{\theta}}_B\cdot\boldsymbol{\theta}_v) = 0. \tag{2.20}$$

We do not solve this here. We studied a similar problem in Pub. I. Although the equation there was slightly different, we still expect the solution to behave in roughly the same manner, that is, $|\boldsymbol{\theta}_v| \sim e^{-r/(2\xi_D/\sqrt{15})}$ as $r \to \infty$.

Before moving on to spin dynamics, let us introduce the Fourier transform, which we shall use later. Since we assume that the vortex is uniform in the z direction, a two-dimensional transform is sufficient. We use the convention

$$\mathcal{F}\{f(\boldsymbol{r})\}(\boldsymbol{k}) = f(\boldsymbol{k}) = \iint d^2 r e^{-i\boldsymbol{k}\cdot\boldsymbol{r}} f(\boldsymbol{r}), \tag{2.21}$$

$$\mathcal{F}^{-1}\{f(\boldsymbol{k})\}(\boldsymbol{r}) = f(\boldsymbol{r}) = \frac{1}{(2\pi)^2} \iint d^2 k e^{i\boldsymbol{k}\cdot\boldsymbol{r}} f(\boldsymbol{k}). \tag{2.22}$$

Here, $f(\boldsymbol{r})$ is an arbitrary function of position (and possibly other parameters not shown explicitly), $\boldsymbol{r} = x\hat{\boldsymbol{x}} + y\hat{\boldsymbol{y}} = r\cos\varphi\hat{\boldsymbol{x}} + r\sin\varphi\hat{\boldsymbol{y}}$, and $\boldsymbol{k} = k_x\hat{\boldsymbol{x}} + k_y\hat{\boldsymbol{y}} = k\cos\varphi_k\hat{\boldsymbol{x}} + k\sin\varphi_k\hat{\boldsymbol{y}}$. As an example, the Fourier transform of $\boldsymbol{\theta}_v(\boldsymbol{r})$ in Eq. (2.18) is given by

$$\begin{aligned}\boldsymbol{\theta}_v(\boldsymbol{k}) = &- i\pi\frac{(C_1 - C_2)\sin[2(\varphi_k - \zeta)]}{k}\hat{\boldsymbol{k}} \\ &- i\pi\frac{(1+c)(C_1 + C_2) + (C_1 - C_2)\cos[2(\varphi_k - \zeta)]}{(1+c)k}\hat{\boldsymbol{\varphi}}_k.\end{aligned} \tag{2.23}$$

Here, $\hat{\boldsymbol{k}} = \cos\varphi_k\hat{\boldsymbol{x}} + \sin\varphi_k\hat{\boldsymbol{y}}$ and $\hat{\boldsymbol{\varphi}}_k = -\sin\varphi_k\hat{\boldsymbol{x}} + \cos\varphi_k\hat{\boldsymbol{y}}$. The double integral in Eq. (2.21) was calculated in polar coordinates (r, φ).

2.2 Lagrangian formulation of spin dynamics

We base our study of spin dynamics of superfluid ^{3}He on the phenomenological theory originally developed by Leggett [49]. Good reviews of the theory are given in Refs. [8, 1]. To keep the discussion simple, we neglect the intrinsic Leggett–Takagi relaxation mechanism [50]. We estimate its effect in Sec. 2.4.3, where we compare theory with experiments.

The main insight of the Leggett theory is the so-called adiabatic approximation. The interesting and nontrivial part of spin dynamics is caused by the dipole coupling between ^{3}He atoms. However, as we discussed in Sec. 2.1.1, this coupling is weak compared to the superfluid condensation energy. This means that the time scale $\tau_D \sim 10$ μs associated with the motion generated by the dipole coupling is long compared to other intrinsic time scales of the system, such as the gap time $\tau_\Delta = \hbar/\Delta \sim 1$ ns (here Δ is the average value of the superfluid energy gap) or the quasiparticle relaxation time $\tau_Q \sim 100$ ns. One can therefore make an assumption that, if studying the system at time scale τ_D, all the nonconserved degrees of freedom have relaxed to their equilibrium configurations. The only variables that are not relaxed to equilibrium at this time scale are the spin density of the liquid, $\boldsymbol{S}$, and the direction of the order parameter in spin space. The latter condition means that we may write the time dependence of A as

$$\mathsf{A}(t) = \mathsf{R}(t)\cdot\mathsf{A}(0). \tag{2.24}$$

Here, R is a rotation matrix satisfying $\mathsf{R}(0) = \mathsf{I}$ and I is the unit matrix.

Equation (2.24) shows that the motion of the order parameter is purely rotational. The rate of change of A is therefore completely determined by an angular velocity vector $\boldsymbol{\omega}$ (cf. rigid body dynamics), which is related to the time derivative of R via [45]

$$\dot{R}_{ij} = \varepsilon_{ikl}\omega_k R_{lj}. \tag{2.25}$$

Here, ε_{ijk} is the Levi-Civita symbol which satisfies $\varepsilon_{123} = 1$, $\varepsilon_{ijk} = -\varepsilon_{jik} = -\varepsilon_{kji}$. A dot over a symbol denotes time derivative. The spin density of the liquid is related to the angular velocity by [1]

$$\boldsymbol{S} = \frac{1}{\mu_0\gamma_0^2}\overset{\leftrightarrow}{\boldsymbol{\chi}} \cdot (\boldsymbol{\omega} - \boldsymbol{\omega}_L), \tag{2.26}$$

where μ_0 is the vacuum permeability, γ_0 is the gyromagnetic ratio of ^{3}He, $\boldsymbol{\omega}_L = -\gamma_0\boldsymbol{B}$ is the Larmor frequency vector, $\boldsymbol{B}$ is the external magnetic field, and $\overset{\leftrightarrow}{\boldsymbol{\chi}}$ is the magnetic susceptibility tensor.

The Leggett theory can be formulated in the framework of classical Lagrangian field theory. This was first done by Maki [51]. The advantage of the Lagrangian formulation is that it simplifies the use of different parametrisations for R. The Lagrangian density of the system is [1]

$$\mathcal{L} = \frac{1}{2\mu_0\gamma_0^2}\left(\boldsymbol{\omega} - \boldsymbol{\omega}_L\right) \cdot \overset{\leftrightarrow}{\boldsymbol{\chi}} \cdot \left(\boldsymbol{\omega} - \boldsymbol{\omega}_L\right) - f_D - f_G. \tag{2.27}$$

In general, the dipole energy f_D, the gradient energy f_G, the angular velocity $\boldsymbol{\omega}$, and the magnetic susceptibility tensor $\overset{\leftrightarrow}{\boldsymbol{\chi}}$ depend on the time-dependent order parameter (2.24).

2.3 Spin dynamics in the bulk B phase

Let us apply the theory of spin dynamics to the bulk B phase, the order parameter and the spin density of which are homogeneous. We derive the Leggett equations of spin dynamics from the Lagrangian density (2.27), and use these to study homogeneous precession of spin density about an external, static magnetic field.

2.3.1 Derivation of the equations of motion

In the B phase, the magnetic susceptibility is isotropic [1],

$$\overset{\leftrightarrow}{\boldsymbol{\chi}} = \chi\mathsf{I}, \tag{2.28}$$

and the order parameter is given by Eq. (2.1). Since the order parameter is already proportional to a rotation matrix, and the product of two rotations is also a rotation, we can include the time dependence into $\boldsymbol{\theta}$ instead of using Eq. (2.24) directly.

Simplifying Eq. (2.27), the Lagrangian density is given by

$$\mathcal{L} = \frac{\chi}{2\mu_0\gamma_0^2}|\boldsymbol{\omega} - \boldsymbol{\omega}_L|^2 - f_D, \tag{2.29}$$

where f_D is given by Eq. (2.5). Using Eqs. (2.7) and (2.25), the angular velocity $\boldsymbol{\omega}$ is

$$\boldsymbol{\omega} = \mathsf{M}(\boldsymbol{\theta}) \cdot \dot{\boldsymbol{\theta}}, \tag{2.30}$$

where the components of the matrix M are given by

$$\begin{aligned} M_{ij} &= -\frac{1}{2}\varepsilon_{ikl}\frac{\partial R_{km}}{\partial \theta_j}R_{lm} \\ &= \frac{\sin\theta}{\theta}\delta_{ij} + \frac{\theta - \sin\theta}{\theta}\hat{\theta}_i\hat{\theta}_j - \frac{1-\cos\theta}{\theta}\varepsilon_{ijk}\hat{\theta}_k. \end{aligned} \tag{2.31}$$

There are different possible routes to follow. One way is to study the Lagrangian equations of motion [52]

$$\frac{d}{dt}\frac{\partial\mathcal{L}}{\partial\dot{\boldsymbol{\theta}}} - \frac{\partial\mathcal{L}}{\partial\boldsymbol{\theta}} = 0. \tag{2.32}$$

Instead, we use the Hamiltonian formalism. The momentum density conjugate to $\boldsymbol{\theta}$ is [52]

$$\boldsymbol{\pi} = \frac{\partial\mathcal{L}}{\partial\dot{\boldsymbol{\theta}}} = \frac{\chi}{\mu_0\gamma_0^2}\mathsf{M}^T \cdot (\boldsymbol{\omega} - \boldsymbol{\omega}_L), \tag{2.33}$$

where M^T is the transpose of M. Comparing this with Eq. (2.26), we find that $\boldsymbol{\pi}$ and $\boldsymbol{S}$ are related by

$$\boldsymbol{\pi} = \mathsf{M}^T \cdot \boldsymbol{S}. \tag{2.34}$$

By definition, the Hamiltonian density is given by [52]

$$\begin{aligned} \mathcal{H} &= \boldsymbol{\pi} \cdot \dot{\boldsymbol{\theta}} - \mathcal{L} \\ &= \frac{\mu_0\gamma_0^2}{2\chi}|\mathsf{M}^{-T} \cdot \boldsymbol{\pi}|^2 + \boldsymbol{\omega}_L \cdot (\mathsf{M}^{-T} \cdot \boldsymbol{\pi}) + f_D \\ &= \frac{\mu_0\gamma_0^2}{2\chi}S^2 + \boldsymbol{\omega}_L \cdot \boldsymbol{S} + f_D, \end{aligned} \tag{2.35}$$

which is the familiar Leggett Hamiltonian density [49, 8, 1]. The Hamiltonian equations of motion are [52]

$$\dot{\theta}_i = \frac{\partial\mathcal{H}}{\partial\pi_i}, \tag{2.36}$$

$$\dot{\pi}_i = -\frac{\partial\mathcal{H}}{\partial\theta_i}. \tag{2.37}$$

Since $\boldsymbol{S}$ and $\boldsymbol{\pi}$ are closely related, we can replace the second equation by an equivalent equation for $\boldsymbol{S}$. This equation can be obtained using the general formula [52]

$$\frac{d\boldsymbol{S}}{dt} = \{\boldsymbol{S}, \mathcal{H}\} + \frac{\partial \boldsymbol{S}}{\partial t}, \tag{2.38}$$

where the Poisson bracket is defined as

$$\{\boldsymbol{S}, \mathcal{H}\} = \frac{\partial \boldsymbol{S}}{\partial \theta_i}\frac{\partial \mathcal{H}}{\partial \pi_i} - \frac{\partial \boldsymbol{S}}{\partial \pi_i}\frac{\partial \mathcal{H}}{\partial \theta_i}. \tag{2.39}$$

Straightforward calculation leads to the familiar Leggett equations of spin dynamics [49, 8, 1],

$$\dot{\boldsymbol{S}} = \boldsymbol{\omega}_L \times \boldsymbol{S} + 4\lambda_D \frac{\sin\theta}{\theta}(1 + 4\cos\theta)\boldsymbol{\theta}, \tag{2.40}$$

$$\dot{\boldsymbol{\theta}} = \mathsf{M}^{-1}(\boldsymbol{\theta}) \cdot \left(\frac{\mu_0\gamma_0^2}{\chi}\boldsymbol{S} + \boldsymbol{\omega}_L\right). \tag{2.41}$$

2.3.2 Static equilibrium and longitudinal resonance

The simplest solution to the Leggett equations (2.40) and (2.41) is the static equilibrium, where both $\boldsymbol{S}$ and $\boldsymbol{\theta}$ are independent of time, $\boldsymbol{S}(t) = \boldsymbol{S}_{eq}$ and $\boldsymbol{\theta}(t) = \boldsymbol{\theta}_{eq}$. In such case, Eq. (2.41) implies that

$$\boldsymbol{S}_{eq} = -\frac{\chi}{\mu_0\gamma_0^2}\boldsymbol{\omega}_L. \tag{2.42}$$

In addition, Eq. (2.40) requires that either $\sin\theta_{eq} = 0$ or $1 + 4\cos\theta_{eq} = 0$, that is, $\theta_{eq} = 0$, $\theta_{eq} = \pi$, or $\theta_{eq} = \theta_L$ (remember that we can restrict the rotation angle to the interval $[0, \pi]$, since a rotation by θ about $\hat{\boldsymbol{\theta}}$ is equivalent to a rotation by $2\pi - \theta$ about $-\hat{\boldsymbol{\theta}}$). The Leggett angle θ_L is defined in Eq. (2.8). The angles 0 and π are maxima of the dipole energy (2.5), and thus the solutions $\theta_{eq} = 0$ and $\theta_{eq} = \pi$ are unstable. The angle θ_L, on the other hand, is a minimum of the dipole energy (2.5), and thus the solution $\theta_{eq} = \theta_L$ is stable. In equilibrium, the rotation axis is aligned along the external magnetic field, $\hat{\boldsymbol{\theta}}_{eq} = \hat{\boldsymbol{B}}$, since this is energetically favourable [44].

Let us consider small, harmonic oscillations of $\boldsymbol{S}$ and $\boldsymbol{\theta}$ about the equilibrium solution, that is, $\boldsymbol{S}(t) = \boldsymbol{S}_{eq} + \delta\boldsymbol{S}e^{-i\omega t}$ and $\boldsymbol{\theta}(t) = \boldsymbol{\theta}_{eq} + \delta\boldsymbol{\theta}e^{-i\omega t}$, where $\delta\boldsymbol{S}$ and $\delta\boldsymbol{\theta}$ are constant vectors. Substituting these into the Leggett equations (2.40) and (2.41), keeping only first-order terms in $\delta\boldsymbol{S}$ and $\delta\boldsymbol{\theta}$, and eliminating $\delta\boldsymbol{\theta}$ from the resulting linear system yields

$$-\omega^2\delta\boldsymbol{S} + i\omega\omega_L\hat{\boldsymbol{B}} \times \delta\boldsymbol{S} + \Omega^2\hat{\boldsymbol{B}}(\hat{\boldsymbol{B}} \cdot \delta\boldsymbol{S}) = \boldsymbol{0}, \tag{2.43}$$

where

$$\Omega = \sqrt{\frac{15\mu_0\gamma_0^2\lambda_D}{\chi}}. \tag{2.44}$$

Equation (2.43) shows that in ^{3}He-B, there is a longitudinal resonance mode in which the magnetisation oscillates along the external magnetic field at frequency $\omega = \Omega$ [49]. Such a phenomenon does not occur in the normal state.

2.3.3 Brinkman–Smith mode

Let us assume that $\boldsymbol{S}(0)$ is tipped by an angle β from $\hat{\boldsymbol{S}}_{eq} = -\hat{\boldsymbol{B}}$. If the dipole coupling constant λ_D vanishes, Eq. (2.40) shows that $\boldsymbol{S}$ precesses uniformly about $\hat{\boldsymbol{S}}_{eq}$ with Larmor frequency ω_L. It is interesting to study whether the uniform precession is also possible if $\lambda_D \neq 0$. It turns out that it is indeed, as we show below. This solution is called the Brinkman–Smith mode [53].

Let us look for a solution $\boldsymbol{S}(t) = \boldsymbol{S}_{BS}(t)$, where

$$\boldsymbol{S}_{BS}(t) = \mathsf{R}(\boldsymbol{\omega}_{BS}t) \cdot \boldsymbol{S}_{BS}^{(0)} \tag{2.45}$$

and $\boldsymbol{\omega}_{BS} = \omega_{BS}\hat{\boldsymbol{B}}$. We allow the precession frequency ω_{BS} to differ from the Larmor value ω_L, but we assume that the direction of precession remains unchanged, that is, $\omega_{BS} > 0$. The constant vector $\boldsymbol{S}_{BS}^{(0)}$ satisfies $\hat{\boldsymbol{S}}_{BS}^{(0)} \cdot \hat{\boldsymbol{S}}_{eq} = \cos\beta$, with $0 < \beta < \pi$. Using the Leggett equations (2.40) and (2.41), one can show (see App. A) that $\boldsymbol{\theta}$ has to be of the same form as $\boldsymbol{S}$, that is, $\boldsymbol{\theta}(t) = \boldsymbol{\theta}_{BS}(t)$, where

$$\boldsymbol{\theta}_{BS}(t) = \mathsf{R}(\boldsymbol{\omega}_{BS}t) \cdot \boldsymbol{\theta}_{BS}^{(0)} \tag{2.46}$$

and $\boldsymbol{\theta}_{BS}^{(0)}$ is a nonzero constant vector. We see that the magnitude of $\boldsymbol{\theta}_{BS}$ is constant, $\theta_{BS} = \theta_{BS}^{(0)}$. However, contrary to the case of static equilibrium (see Sec. 2.1.1), the rotation angle θ_{BS} is not necessarily equal to the Leggett angle θ_L. Plugging $\boldsymbol{S}$ and $\boldsymbol{\theta}$ into Eqs. (2.40) and (2.41) yields (see App. A for details)

$$(\boldsymbol{\omega}_{BS} - \boldsymbol{\omega}_L) \times \boldsymbol{s}_{BS} = \frac{4\Omega^2}{15} \sin\theta_{BS}(1 + 4\cos\theta_{BS})\hat{\boldsymbol{\theta}}_{BS}^{(0)}, \tag{2.47}$$

$$\boldsymbol{0} = \frac{1}{2}\cot\left(\frac{\theta_{BS}}{2}\right)\boldsymbol{s}_{BS} + \left(\frac{\boldsymbol{s}_{BS}}{2} - \boldsymbol{\omega}_{BS}\right) \times \hat{\boldsymbol{\theta}}_{BS}^{(0)}, \tag{2.48}$$

$$\hat{\boldsymbol{\theta}}_{BS}^{(0)} \cdot \boldsymbol{s}_{BS} = 0, \tag{2.49}$$

where $\boldsymbol{s}_{BS} = \mu_0\gamma_0^2\boldsymbol{S}_{BS}^{(0)}/\chi + \boldsymbol{\omega}_L$ and Ω is the longitudinal resonance frequency defined in Eq. (2.44). The unknowns here are ω_{BS}, $S_{BS} = S_{BS}^{(0)}$, $\theta_{BS} = \theta_{BS}^{(0)}$, and $\hat{\boldsymbol{\theta}}_{BS}^{(0)}$.

Consider first the case where the precession frequency is not shifted from the Larmor frequency, that is, $\omega_{BS} = \omega_L$. Equation (2.47) shows that either $\theta_{BS} = \pi$ or $\theta_{BS} = \theta_L$. Linear stability analysis shows that the solution with $\theta_{BS} = \pi$ is not stable, and we shall not consider it further. Taking the dot product between Eq. (2.48) and $\boldsymbol{s}_{BS}/2 - \boldsymbol{\omega}_L$ shows that $S_{BS} = \chi\omega_L/\mu_0\gamma_0^2$. Taking the norm on both sides of Eq. (2.48) gives $(\hat{\boldsymbol{B}} \cdot \hat{\boldsymbol{\theta}}_{BS}^{(0)})^2 = (1 + 4\cos\beta)/5$. This implies that $0 < \beta \leq \theta_L$, and so the solution $\omega_{BS} = \omega_L$ is not possible for tipping angles larger than θ_L. The orientation of $\hat{\boldsymbol{\theta}}_{BS}^{(0)}$ in the plane perpendicular to $\hat{\boldsymbol{B}}$ depends on the orientation of $\hat{\boldsymbol{S}}_{BS}^{(0)}$, which in turn depends on the zero of time.

Let us proceed to the case $\omega_{BS} \neq \omega_L$. Equation (2.47) shows that $\hat{\boldsymbol{\theta}}_{BS}^{(0)}$ points along the direction of $\hat{\boldsymbol{B}} \times \hat{\boldsymbol{s}}_{BS}$, which means that $\hat{\boldsymbol{B}} \cdot \hat{\boldsymbol{\theta}}_{BS}^{(0)} = \boldsymbol{s}_{BS} \cdot \hat{\boldsymbol{\theta}}_{BS}^{(0)} = 0$, and thus Eq. (2.49) is satisfied automatically. To determine the remaining unknowns ω_{BS}, S_{BS}, and θ_{BS}, we need three equations. First, we take the norm on both sides of Eq. (2.47). Second, we calculate the dot product between Eq. (2.48) and $\boldsymbol{s}_{BS}/2 - \boldsymbol{\omega}_{BS}$. Third, we substitute $\hat{\boldsymbol{\theta}}_{BS}^{(0)}$ from Eq. (2.47) into Eq. (2.48). Eliminating S_{BS} and θ_{BS}, we are left with an equation for ω_{BS},

$$\begin{aligned}\omega_L - \frac{5}{4}\omega_{BS} - \frac{15}{16}\frac{\omega_{BS}^2}{\Omega^2}(\omega_{BS} - \omega_L) = \\ \cos\beta\sqrt{\omega_L^2 + \frac{5}{2}\omega_{BS}(\omega_{BS} - \omega_L) + \frac{15}{8}\frac{\omega_{BS}^2}{\Omega^2}(\omega_{BS} - \omega_L)^2}.\end{aligned} \tag{2.50}$$

Once ω_{BS} is known, we can calculate θ_{BS} and S_{BS} using

$$\cos\theta_{BS} = -\frac{1}{4} - \frac{15}{16}\frac{\omega_{BS}(\omega_{BS} - \omega_L)}{\Omega^2}, \tag{2.51}$$

$$\frac{\mu_0\gamma_0^2 S_{BS}}{\chi} = \frac{\sin\theta_{BS}}{\sin\beta}\omega_{BS}. \tag{2.52}$$

Linear stability analysis shows that a stable solution exists only for tipping angles $\beta > \theta_L$.

We have therefore seen that there exists a solution with uniformly precessing magnetisation at all tipping angles β. Figure 2.1 shows the quantities ω_{BS}/ω_L, $\mu_0\gamma_0^2 S_{BS}/\chi\omega_L$, and $\cos\theta_{BS}$ as a function of β for different values of ω_L. The rotation axis $\hat{\boldsymbol{\theta}}_{BS}^{(0)}$ satisfies

$$(\hat{\boldsymbol{\theta}}_{BS}^{(0)} \cdot \hat{\boldsymbol{B}})^2 = \begin{cases}(1 + 4\cos\beta)/5, & 0 < \beta \leq \theta_L, \\ 0, & \theta_L < \beta < \pi.\end{cases} \tag{2.53}$$

2.4 A vortex line in the Brinkman–Smith mode

How does a single vortex line affect the Brinkman–Smith mode? We shall use the same notation as we did in Sec. 2.1.2: the z axis coincides with the vortex axis, the external magnetic field $\boldsymbol{B}$ points in the direction $\hat{\boldsymbol{B}} = \cos\eta\hat{\boldsymbol{z}} + \sin\eta\hat{\boldsymbol{x}}$, the anisotropy vector of the double-core vortex is $\hat{\boldsymbol{b}} = \cos\zeta\hat{\boldsymbol{y}} - \sin\zeta\hat{\boldsymbol{x}}$, and the standard cylindrical coordinates are denoted by (r, φ, z). In addition, we denote the tipping angle of the spin density $\boldsymbol{S}$ from the equilibrium direction $-\hat{\boldsymbol{B}}$ by β, as we did in Sec. 2.3.3. Figure 2.2 shows the various definitions in a pictorial form.

For simplicity, we consider here only tipping angles $\beta \leq \theta_L$. This is sufficient to make comparisons with experiments. The analysis for higher tipping angles is

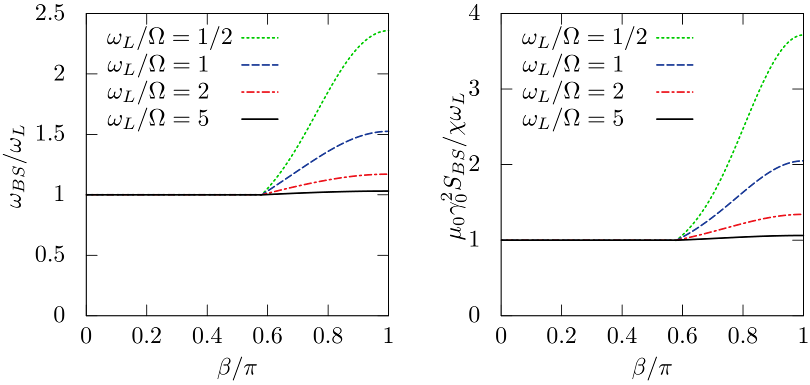

(a) ω_{BS}/ω_L

(b) $\mu_0\gamma_0^2 S_{BS}/\chi\omega_L$

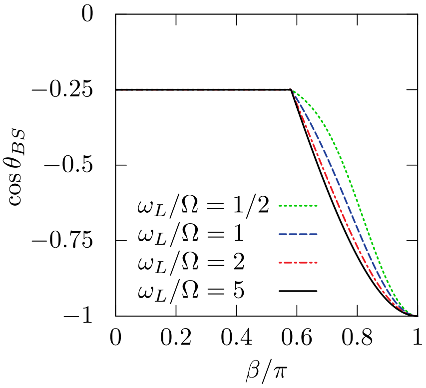

(c) $\cos\theta_{BS}$

Figure 2.1: Important parameters of the Brinkman–Smith mode as a function of the tipping angle β at four different values of the Larmor frequency ω_L. For $\beta > \theta_L \approx 0.58\pi$, the curves are obtained from Eqs. (2.50), (2.51), and (2.52).

essentially identical, but more cumbersome due to the more complicated properties of the Brinkman–Smith mode (see Sec. 2.3.3). The case of $\beta > \theta_L$ is discussed in Pub. III.

In the discussion of the properties of a static vortex line in Sec. 2.1.2, we restricted our attention to the hydrostatic region $r \gg \xi_0$ and used the detailed structure of the vortex core only as a boundary condition to determine the asymptotic solution (2.18) (valid at $\xi_0 \ll r \ll \xi_D$). It turns out that this is also enough for us to study spin dynamics of a vortex line in the Brinkman–Smith mode; we do not need to consider what happens in the core region of the vortex. We can calculate the energy flux density of spin waves using the asymptotic solution, and the result thus obtained converges to a finite value even in the limit $r \to 0$, despite the fact that $\boldsymbol{\theta}_v$ diverges. This is in contrast with the Leggett–Takagi

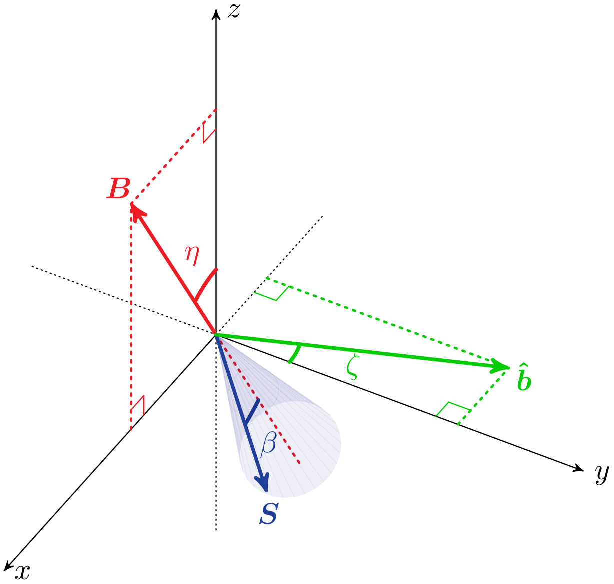

Figure 2.2: Definitions of the angles β, ζ, and η. The vortex axis coincides with the z axis, $\boldsymbol{B}$ is the static external magnetic field, $\hat{\boldsymbol{b}}$ is the anisotropy vector of the double-core vortex, pointing from one of the half cores to the other, and $\boldsymbol{S}$ is the spin density which precesses uniformly about $-\boldsymbol{B}$ with tipping angle β. The figure was originally published in Pub. III.

relaxation, where we have to introduce a cut-off radius near the core in order to avoid logarithmic divergence, see Pub. I for details.

Combining the results from the hydrostatic theory of vortices [see Eq. (2.11)] and from the Leggett theory [see Eq. (2.24)], we can write the order parameter of the system as

$$\mathsf{A} \approx e^{i\varphi}\Delta_B \mathsf{R}(\boldsymbol{\theta}_{BS})\mathsf{R}(\boldsymbol{\theta})\mathsf{R}(\boldsymbol{\theta}_v). \tag{2.54}$$

Here $\boldsymbol{\theta}_{BS}(t)$ is the rotation vector of the bulk Brinkman–Smith mode (see Sec. 2.3.3) and $\boldsymbol{\theta}_v(\boldsymbol{r})$ is the rotation vector of the static vortex line (see Sec. 2.1.2). Since the Brinkman–Smith mode interacts with the vortex, we need an additional rotation $\boldsymbol{\theta}(\boldsymbol{r},t)$ to describe the dynamics of the order parameter.

There are two implicit assumptions made when writing the order parameter in the form (2.54). First, the vortex core is assumed to be stationary, meaning that $\boldsymbol{\theta}_v$, determined by the core, is constant in time. The second point is more subtle. Since we assume that $\boldsymbol{\theta}_{BS}$ is a given function of time, determined by the Brinkman–Smith mode, we are quietly assuming that there must be an external agent acting on the system, trying to keep the Brinkman–Smith mode unchanged. This is a common situation in problems of Lagrangian mechanics, where one can impose constraints on the system under study by choosing the coordinates conveniently, and not care how these constraints are actually implemented. An alternative way, which allows to calculate the forces of constraint, is to use Lagrange multipliers [52, 45]. We show in Sec. 2.4.3 that in order to sustain the Brinkman–Smith mode, energy is needed from the environment. Experimentally, this can be done using time-dependent magnetic fields, but here we do not have to worry about that, since the formulation of the problem takes it into account automatically.

We saw in Sec. 2.1.2 that $|\boldsymbol{\theta}_v| \ll 1$. Thus, we expect that the effect of the vortex line on the Brinkman–Smith mode is small, so that $|\boldsymbol{\theta}| \ll 1$. Based on this, we shall study linear dynamics of $\boldsymbol{\theta}$. For $\boldsymbol{\theta}_v$, we can use the solution which minimises the gradient energy, Eq. (2.18), since it behaves correctly near the core. The dipole energy is taken into account via $\boldsymbol{\theta}$. As a boundary condition for $\boldsymbol{\theta}$, we demand that $\lim_{r\to 0}\boldsymbol{\theta} = \mathbf{0}$, so that the order parameter of the static vortex is not modified near the core.

The equations can be simplified using dimensionless variables. For each variable q, we define a corresponding dimensionless variable $\tilde{q}$ and a unit q_u in which we want to measure q, so that $q = \tilde{q}q_u$. We measure time in units of Ω^{-1} and length in units of v/Ω. Here, Ω is the longitudinal resonance frequency of the B phase, defined in Eq. (2.44), and v is a characteristic spin wave velocity, defined by

$$v = \sqrt{\frac{4\mu_0\gamma_0^2\lambda_{G2}}{\chi}}. \tag{2.55}$$

All angular velocities, such as ω_L and ω_{BS}, are measured in units of Ω. The parameters C_1 and C_2 describing the structure of the vortex [see Eq. (2.18)] are measured in units of R_0 [see Eq. (2.19)]. Energy densities, such as $\mathcal{L}$ and f_D, are measured in units of $\chi\Omega^4R_0^2/\mu_0\gamma_0^2v^2$. Spin density is measured in units of $\chi\Omega^2R_0/\mu_0\gamma_0^2v$. Finally, although $\boldsymbol{\theta}$ and $\boldsymbol{\theta}_v$ are already dimensionless, we measure them (but not $\boldsymbol{\theta}_{BS}$) in units of $R_0\Omega/v$. This is a small quantity $\sim \xi_0/\xi_D$, which we use as an expansion parameter below. Equation (2.18) shows that $|\tilde{\boldsymbol{\theta}}_v| \sim 1$, and we assume that the same is true also for $\tilde{\boldsymbol{\theta}}$. For simplicity, we shall drop the tildes from the dimensionless variables. This should not cause any confusion, since we shall use the dimensionless variables for the rest of this chapter.

The Lagrangian density of the system can be obtained using Eqs. (2.27), (2.54), (2.5), (2.6), and (2.25). Expanding the Lagrangian density in powers of $\varepsilon = R_0\Omega/v \ll 1$, we obtain

$$\mathcal{L} = \varepsilon^{-2}\mathcal{L}_{-2} + \varepsilon^{-1}\mathcal{L}_{-1} + \mathcal{L}_0 + \mathcal{O}(\varepsilon). \tag{2.56}$$

Here,

$$\mathcal{L}_{-2} = \frac{\omega_L^2}{2} + \frac{1}{30}, \tag{2.57}$$

$$\mathcal{L}_{-1} = -\omega_L\hat{\boldsymbol{B}}\cdot\dot{\boldsymbol{\theta}}. \tag{2.58}$$

Their contribution to the motion of $\boldsymbol{\theta}$ vanishes identically, as we show below. The first nontrivial term in the Lagrangian density is

$$\begin{aligned}\mathcal{L}_0 = \frac{1}{2}|\dot{\boldsymbol{\theta}}|^2 - \frac{\omega_L}{2}\hat{\boldsymbol{B}}\cdot(\boldsymbol{\theta}\times\dot{\boldsymbol{\theta}}) - \frac{1}{2}[\hat{\boldsymbol{\theta}}_{BS}\cdot(\boldsymbol{\theta}+\boldsymbol{\theta}_v)]^2 \\ - \frac{1+c}{2}\frac{\partial(\theta_j+\theta_{v,j})}{\partial r_i}\frac{\partial(\theta_j+\theta_{v,j})}{\partial r_i} + \frac{c}{2}\frac{\partial(\theta_j+\theta_{v,j})}{\partial r_i}\frac{\partial(\theta_i+\theta_{v,i})}{\partial r_j}.\end{aligned} \tag{2.59}$$

This describes linear motion of $\boldsymbol{\theta}$, since it is quadratic in $\boldsymbol{\theta}$. We shall neglect the higher order terms, and concentrate on linear dynamics. The equation of motion for $\boldsymbol{\theta}$ can be obtained from the usual Euler–Lagrange equation [52]

$$\frac{\partial}{\partial t}\frac{\partial\mathcal{L}}{\partial\dot{\theta}_i} + \partial_j\frac{\partial\mathcal{L}}{\partial\partial_j\theta_i} - \frac{\partial\mathcal{L}}{\partial\theta_i} = 0. \tag{2.60}$$

Plugging in the Lagrangian density (2.56), it is easy to see that neither $\mathcal{L}_{-2}$ nor $\mathcal{L}_{-1}$ contribute to the dynamics of $\boldsymbol{\theta}$. As a result, we obtain the linearised equation of motion for $\boldsymbol{\theta}$,

$$\ddot{\boldsymbol{\theta}} - \omega_L\hat{\boldsymbol{B}}\times\dot{\boldsymbol{\theta}} + \hat{\boldsymbol{\theta}}_{BS}(\hat{\boldsymbol{\theta}}_{BS}\cdot\boldsymbol{\theta}) - (1+c)\nabla^2\boldsymbol{\theta} + c\boldsymbol{\nabla}(\boldsymbol{\nabla}\cdot\boldsymbol{\theta}) = \boldsymbol{\rho}, \tag{2.61}$$

which looks like a generalisation of the standard wave equation [54]. Indeed, we show in Secs. 2.4.1 and 2.4.2 that waves constitute a part of the solution. The function on the right-hand side,

$$\boldsymbol{\rho} = (1+c)\nabla^2\boldsymbol{\theta}_v - c\boldsymbol{\nabla}(\boldsymbol{\nabla}\cdot\boldsymbol{\theta}_v) - \hat{\boldsymbol{\theta}}_{BS}(\hat{\boldsymbol{\theta}}_{BS}\cdot\boldsymbol{\theta}_v), \tag{2.62}$$

is the source term which drives $\boldsymbol{\theta}$. Since $\boldsymbol{\theta}_v$ is given by Eq. (2.18), the source reduces to $\boldsymbol{\rho} = -\hat{\boldsymbol{\theta}}_{BS}(\hat{\boldsymbol{\theta}}_{BS}\cdot\boldsymbol{\theta}_v)$.

The general solution to Eq. (2.61) seems to be quite difficult to obtain due to the presence of both $\hat{\boldsymbol{\theta}}_{BS}\hat{\boldsymbol{\theta}}_{BS}$ (which depends on time) and $\boldsymbol{\nabla\nabla}$. We have therefore considered two different approximations. In Sec. 2.4.1, we assume that $c = 0$, which means that the term $\boldsymbol{\nabla\nabla}$ vanishes from Eq. (2.61). In Sec. 2.4.2, we assume that the external magnetic field is large ($\omega_L \gg 1$). This allows us to neglect the time dependent coefficient $\hat{\boldsymbol{\theta}}_{BS}\hat{\boldsymbol{\theta}}_{BS}$ from the equation.

Once $\boldsymbol{\theta}$ is known, the spin density can be calculated using Eq. (2.26). We obtain

$$\boldsymbol{S} = \varepsilon^{-1}\boldsymbol{S}_{-1} + \boldsymbol{S}_0 + \mathcal{O}(\epsilon), \tag{2.63}$$

where

$$\boldsymbol{S}_{-1} = -\omega_L\mathsf{R}(\boldsymbol{\theta}_{BS})\cdot\hat{\boldsymbol{B}}, \tag{2.64}$$

$$\boldsymbol{S}_0 = \mathsf{R}(\boldsymbol{\theta}_{BS})\cdot\dot{\boldsymbol{\theta}}. \tag{2.65}$$

We see that the vortex perturbs the uniformly precessing magnetisation $\varepsilon^{-1}\boldsymbol{S}_{-1}$ of the Brinkman–Smith mode, but the effect is relatively small since ϵ^{-1} is large.

The Hamiltonian density $\mathcal{H}$ can be expanded in powers of ε as

$$\begin{aligned}\mathcal{H} &= \dot{\boldsymbol{\theta}} \cdot \frac{\partial \mathcal{L}}{\partial \dot{\boldsymbol{\theta}}} - \mathcal{L} \\ &= \varepsilon^{-2}\mathcal{H}_{-2} + \mathcal{H}_0 + \mathcal{O}(\varepsilon),\end{aligned} \tag{2.66}$$

where

$$\mathcal{H}_{-2} = \dot{\boldsymbol{\theta}} \cdot \frac{\partial \mathcal{L}_{-2}}{\partial \dot{\boldsymbol{\theta}}} - \mathcal{L}_{-2} = -\frac{\omega_L^2}{2} - \frac{1}{30} \tag{2.67}$$

and

$$\begin{aligned}\mathcal{H}_0 &= \dot{\boldsymbol{\theta}} \cdot \frac{\partial \mathcal{L}_0}{\partial \dot{\boldsymbol{\theta}}} - \mathcal{L}_0 \\ &= \frac{1}{2}|\dot{\boldsymbol{\theta}}|^2 + \frac{1}{2}[\hat{\boldsymbol{\theta}}_{BS} \cdot (\boldsymbol{\theta} + \boldsymbol{\theta}_v)]^2 + \frac{1+c}{2}\frac{\partial(\theta_j + \theta_{v,j})}{\partial r_i}\frac{\partial(\theta_j + \theta_{v,j})}{\partial r_i} \\ &- \frac{c}{2}\frac{\partial(\theta_j + \theta_{v,j})}{\partial r_i}\frac{\partial(\theta_i + \theta_{v,i})}{\partial r_j}.\end{aligned} \tag{2.68}$$

Here, $\varepsilon^{-2}\mathcal{H}_{-2}$ is the energy density of the Brinkman–Smith mode, while $\mathcal{H}_0$ is the energy density related to the motion of $\boldsymbol{\theta}$. In general, the Hamiltonian density obeys the continuity equation [52]

$$\frac{\partial \mathcal{H}}{\partial t} + \boldsymbol{\nabla} \cdot \boldsymbol{\Sigma} = -\left(\frac{\partial \mathcal{L}}{\partial t}\right)_{\text{explicit}}. \tag{2.69}$$

Here, the time derivative of $\mathcal{H}$ is calculated after substituting in the solution $\boldsymbol{\theta}$, while the time derivative of $\mathcal{L}$ measures the explicit time dependence of $\mathcal{L}$. The vector $\boldsymbol{\Sigma}$ is the energy flux density, defined by

$$\Sigma_i = \frac{\partial \mathcal{L}}{\partial(\partial\theta_j/\partial r_i)}\frac{\partial \theta_j}{\partial t}. \tag{2.70}$$

Equation (2.69) is similar to Poynting's theorem in electromagnetism [55, 56].

The energy stored inside a volume V (which has to exclude the vortex core according to assumptions made in the beginning of the section) is

$$E = \int_V d^3r\mathcal{H}. \tag{2.71}$$

Using the continuity equation (2.69) and the divergence theorem (Gauss' theorem) [57], we calculate the rate of change of energy inside V as

$$\frac{dE}{dt} = -\int_{\partial V} \boldsymbol{\Sigma} \cdot d\boldsymbol{A} + \int_V d^3rp, \tag{2.72}$$

where

$$\Sigma_i = -(1+c)\dot{\theta}_j\frac{\partial(\theta_j + \theta_{v,j})}{\partial r_i} + c\dot{\theta}_j\frac{\partial(\theta_i + \theta_{v,i})}{\partial r_j} \tag{2.73}$$

and

$$p = [\hat{\boldsymbol{\theta}}_{BS} \cdot (\boldsymbol{\theta} + \boldsymbol{\theta}_v)][\dot{\hat{\boldsymbol{\theta}}}_{BS} \cdot (\boldsymbol{\theta} + \boldsymbol{\theta}_v)]. \tag{2.74}$$

Equation (2.72) states the conservation of energy. The Brinkman–Smith mode interacts with the vortex, driving $\boldsymbol{\theta}$ and thus pumping energy into V. This is represented by the volume integral of p. The motion of $\boldsymbol{\theta}$ then generates a flow of energy, carrying energy through the surface ∂V of V. This is represented by the surface integral of $\boldsymbol{\Sigma}$. The total change in energy is due to these two contributions. In steady state, which we are interested in, the time average of dE/dt vanishes.

2.4.1 Isotropic approximation

Let us consider the equation of motion (2.61) in the limit $c = 0$ [in which case $\lambda_{G1} = 0$, see Eqs. (2.14) and (2.6)]. This means that we neglect the anisotropic gradient term $\boldsymbol{\nabla\nabla}$ from Eq. (2.61), and only keep the isotropic Laplacian part ∇^2.

The rotation vector of the Brinkman–Smith mode, given by Eq. (2.46), can be written as

$$\boldsymbol{\theta}_{BS} = \mathsf{R}(\eta\hat{\boldsymbol{y}})\mathsf{R}(\omega_L t\hat{\boldsymbol{z}}) \cdot \boldsymbol{\theta}_{BS}^{(00)}, \tag{2.75}$$

where $\boldsymbol{\theta}_{BS}^{(00)} = \mathsf{R}(-\eta\hat{\boldsymbol{y}}) \cdot \boldsymbol{\theta}_{BS}^{(0)}$. Using Eq. (2.53) and choosing the zero of time appropriately, we obtain

$$\hat{\boldsymbol{\theta}}_{BS}^{(00)} = \sqrt{\frac{4 - 4\cos\beta}{5}}\hat{\boldsymbol{y}} + \sqrt{\frac{1 + 4\cos\beta}{5}}\hat{\boldsymbol{z}}. \tag{2.76}$$

Inspired by the form of $\boldsymbol{\theta}_{BS}$, we define a new variable $\boldsymbol{\alpha}$ satisfying

$$\boldsymbol{\theta} = \mathsf{R}(\eta\hat{\boldsymbol{y}})\mathsf{R}(\omega_L t\hat{\boldsymbol{z}}) \cdot \boldsymbol{\alpha}. \tag{2.77}$$

Substituting this into Eq. (2.61) yields

$$\ddot{\boldsymbol{\alpha}} + \omega_L\hat{\boldsymbol{z}} \times \dot{\boldsymbol{\alpha}} + \hat{\boldsymbol{\theta}}_{BS}^{(00)}(\hat{\boldsymbol{\theta}}_{BS}^{(00)} \cdot \boldsymbol{\alpha}) - \nabla^2\boldsymbol{\alpha} = \tilde{\boldsymbol{\rho}}, \tag{2.78}$$

where

$$\tilde{\boldsymbol{\rho}} = \mathsf{R}(-\omega_L t\hat{\boldsymbol{z}})\mathsf{R}(-\eta\hat{\boldsymbol{y}}) \cdot \boldsymbol{\rho}. \tag{2.79}$$

We emphasise that there is no explicit time dependence in the coefficients of $\boldsymbol{\alpha}$ on the left-hand side of (2.78). This simplifies the subsequent analysis significantly. The source term $\tilde{\boldsymbol{\rho}}$ can be written as

$$\tilde{\boldsymbol{\rho}} = \Re\left\{\tilde{\boldsymbol{\rho}}_0 + e^{-i\omega_L t}\tilde{\boldsymbol{\rho}}_1\right\}, \tag{2.80}$$

where $\Re$ denotes the real part,

$$\tilde{\boldsymbol{\rho}}_0 = -\hat{\boldsymbol{\theta}}_{BS}^{(00)}\left[\hat{\boldsymbol{\theta}}_{BS}^{(00)} \cdot \mathsf{M}_0 \cdot \mathsf{R}(-\eta\hat{\boldsymbol{y}}) \cdot \boldsymbol{\theta}_v\right], \tag{2.81}$$

$$\tilde{\boldsymbol{\rho}}_1 = -\hat{\boldsymbol{\theta}}_{BS}^{(00)}\left[\hat{\boldsymbol{\theta}}_{BS}^{(00)} \cdot \mathsf{M}_- \cdot \mathsf{R}(-\eta\hat{\boldsymbol{y}}) \cdot \boldsymbol{\theta}_v\right], \tag{2.82}$$

and

$$\mathsf{M}_0 = \begin{pmatrix} 0 & 0 & 0 \\ 0 & 0 & 0 \\ 0 & 0 & 1 \end{pmatrix}, \qquad \mathsf{M}_- = \begin{pmatrix} 1 & i & 0 \\ -i & 1 & 0 \\ 0 & 0 & 0 \end{pmatrix}. \tag{2.83}$$

We are interested in the steady-state solution, and so we can assume that the time dependence of $\boldsymbol{\alpha}$ is of the same form as the time dependence of $\tilde{\boldsymbol{\rho}}$, that is,

$$\boldsymbol{\alpha} = \Re\left\{\boldsymbol{\alpha}_0 + e^{-i\omega_L t}\boldsymbol{\alpha}_1\right\}. \tag{2.84}$$

Substituting this into Eq. (2.78), we obtain the equations

$$\mathsf{K}_0(\boldsymbol{\nabla}) \cdot \boldsymbol{\alpha}_0 = \tilde{\boldsymbol{\rho}}_0, \tag{2.85}$$

$$\mathsf{K}_1(\boldsymbol{\nabla}) \cdot \boldsymbol{\alpha}_1 = \tilde{\boldsymbol{\rho}}_1, \tag{2.86}$$

where

$$\mathsf{K}_0(\boldsymbol{\nabla}) = -\nabla^2 + \hat{\boldsymbol{\theta}}^{(00)}_{BS}\hat{\boldsymbol{\theta}}^{(00)}_{BS}, \tag{2.87}$$

$$\mathsf{K}_1(\boldsymbol{\nabla}) = \mathsf{K}_0(\boldsymbol{\nabla}) - \omega_L^2\mathsf{I} - i\omega_L^2[\hat{\boldsymbol{z}}]_\times, \tag{2.88}$$

and $[\hat{\boldsymbol{z}}]_\times$ denotes the cross product matrix of $\hat{\boldsymbol{z}}$, defined by $[\hat{\boldsymbol{z}}]_\times \cdot \boldsymbol{v} = \hat{\boldsymbol{z}} \times \boldsymbol{v}$ for an arbitrary vector $\boldsymbol{v}$. Since the equations are linear, it is convenient to work in the Fourier space, see Eqs. (2.21) and (2.22). Under Fourier transform, the gradient operator transforms as $\boldsymbol{\nabla} \to i\boldsymbol{k}$. Thus, Eqs. (2.85) and (2.86) are transformed into algebraic equations which are straightforward to solve. We obtain

$$\boldsymbol{\alpha}_0(\boldsymbol{k}) = \mathsf{K}_0^{-1}(i\boldsymbol{k}) \cdot \tilde{\boldsymbol{\rho}}_0(\boldsymbol{k}) = \theta_{v,x}(\boldsymbol{k}) \sin\eta \frac{\boldsymbol{D}_0}{k^2 - k_0^2}, \tag{2.89}$$

$$\boldsymbol{\alpha}_1(\boldsymbol{k}) = \mathsf{K}_1^{-1}(i\boldsymbol{k}) \cdot \tilde{\boldsymbol{\rho}}_1(\boldsymbol{k}) = [\theta_{v,y}(\boldsymbol{k}) - i\theta_{v,x}(\boldsymbol{k})\cos\eta] \sum_{j=1}^{3} \frac{\boldsymbol{D}_j}{k^2 - k_j^2}. \tag{2.90}$$

Here,

$$k_0 = i, \tag{2.91}$$

$$\boldsymbol{D}_0 = -\frac{1}{5}\begin{pmatrix} 0 \\ \sqrt{(4 - 4\cos\beta)(1 + 4\cos\beta)} \\ 1 + 4\cos\beta \end{pmatrix}. \tag{2.92}$$

The wave numbers k_j, $j = 1, 2, 3$, depend on ω_L and β. They can be obtained by solving the determinant equation

$$\det \mathsf{K}(i\boldsymbol{k}) = k^6 - (3\omega_L^2 - 1)k^4 + 2\omega_L^2(\omega_L^2 - 1)k^2 + (1 - n_z^2)\omega_L^4 = 0. \tag{2.93}$$

This is a cubic equation for k^2. It has three solutions, $k_1^2 < 0$, $k_2^2 > 0$, and $k_3^2 > 0$. This means that k_1 is purely imaginary, while k_2 and k_3 are real. We choose

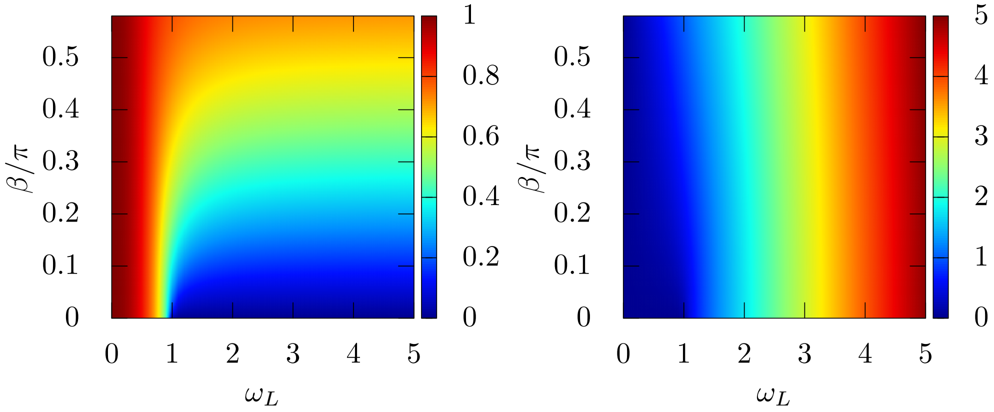

(a) $|k_1|$ (b) $|k_2|$

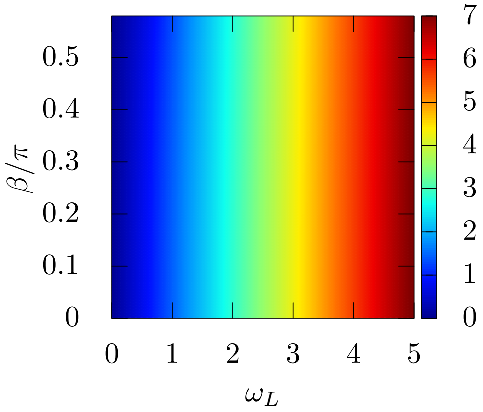

(c) $|k_3|$

Figure 2.3: The magnitudes of the wave numbers k_j appearing in Eqs. (2.90) and (2.104) as a function of ω_L and β. The wave numbers k_j are calculated using Eq. (2.93).

the sign convention $k_1 = i|k_1|$, $k_2 = |k_2|$, and $k_3 = |k_3|$. Figure 2.3 shows the magnitudes $|k_j|$ as a function of ω_L and β. The vectors $\boldsymbol{D}_j$, $j = 1, 2, 3$, depend on ω_L and β. They can be obtained from

$$\boldsymbol{D}_j = \lim_{k \to k_j} \frac{(k^2 - k_j^2)\mathsf{K}_1^{-1}(i\boldsymbol{k}) \cdot \tilde{\boldsymbol{\rho}}_1(\boldsymbol{k})}{\theta_{v,y}(\boldsymbol{k}) - i\theta_{v,x}(\boldsymbol{k}) \cos \eta}. \tag{2.94}$$

Figure 2.4 shows the magnitudes $|\boldsymbol{D}_j|$ as a function of ω_L and β.

Since we are interested in the solution in the position space, we take the inverse

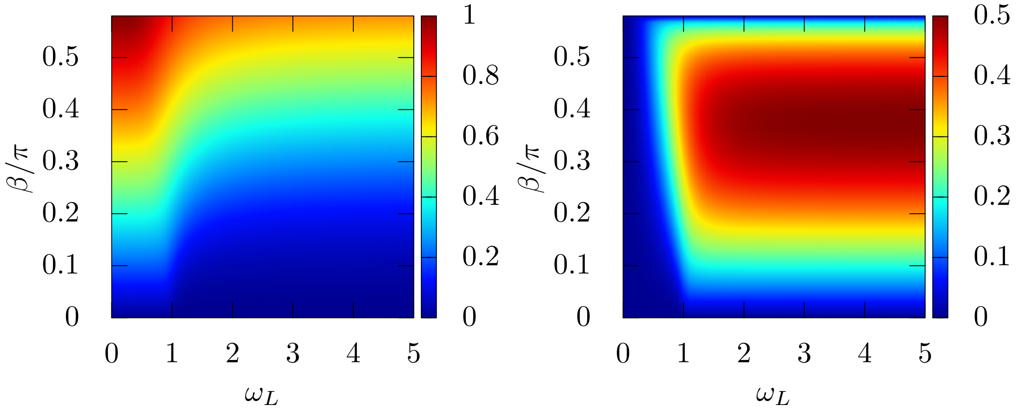

(a) $|\boldsymbol{D}_1|$ (b) $|\boldsymbol{D}_2|$

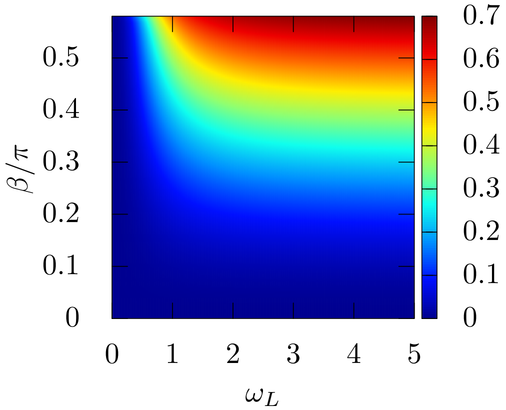

(c) $|\boldsymbol{D}_3|$

Figure 2.4: The magnitudes of the vectors $\boldsymbol{D}_j$ appearing in Eqs. (2.90) and (2.104) as a function of ω_L and β. The vectors $\boldsymbol{D}_j$ are calculated using Eq. (2.94).

transform of Eqs. (2.89) and (2.90). Using Eq. (2.22), we obtain (for $n = 0, 1$)

$$\begin{aligned}\boldsymbol{\alpha}_n(\boldsymbol{r}) &= \frac{1}{(2\pi)^2}\iint d^2k e^{i\boldsymbol{k}\cdot\boldsymbol{r}}\boldsymbol{\alpha}_n(\boldsymbol{k}) \\ &= \frac{1}{(2\pi)^2}\int_0^{2\pi} d\varphi_k \int_0^{\infty} kdke^{ikr\cos(\varphi-\varphi_k)}\boldsymbol{\alpha}_n(k,\varphi_k).\end{aligned} \tag{2.95}$$

To proceed, we use the Jacobi–Anger expansion [58]

$$e^{iz\cos\theta} = J_0(z) + 2\sum_{m=1}^{\infty} i^m J_m(z)\cos(m\theta) \tag{2.96}$$

for the exponential function. Here, J_m are Bessel functions of the first kind. Substituting $\boldsymbol{\alpha}_n(\boldsymbol{k})$ from Eqs. (2.89) and (2.90), using the Fourier transform of $\boldsymbol{\theta}_v$

from Eq. (2.23), and using the orthogonality of trigonometric functions, we obtain

$$\boldsymbol{\alpha}_0(\boldsymbol{r}) = \vartheta_{v,x}(\varphi)\sin\eta \boldsymbol{D}_0 \int_0^\infty dk \frac{J_1(kr)}{k^2 - k_0^2}, \tag{2.97}$$

$$\boldsymbol{\alpha}_1(\boldsymbol{r}) = [\vartheta_{v,y}(\varphi) - i\vartheta_{v,x}(\varphi)\cos\eta] \sum_{j=1}^{3} \boldsymbol{D}_j \int_0^\infty dk \frac{J_1(kr)}{k^2 - k_j^2}, \tag{2.98}$$

where $\boldsymbol{\vartheta}_v(\varphi) \equiv r\boldsymbol{\theta}_v(r,\varphi)$.

The only thing left to do is to evaluate the integral $\int_0^\infty dk J_1(kr)/(k^2 - k_j^2)$. If $k_j^2 > 0$, there is a simple pole at $k = k_j$. We use the standard trick, and shift the pole slightly away from the real axis by addwould like to knowing a small imaginary part to the pole, $k_j \to k_j \pm i\delta$, $\delta > 0$. The resulting integral can be calculated analytically [58], and the result converges to a finite value in the limit $\delta \to 0$. Choosing the positive sign gives

$$\int_0^\infty dk \frac{J_1(kr)}{k^2 - k_j^2} = -\frac{1}{k_j^2 r} + \frac{i\pi}{2k_j} H_1^{(1)}(k_j r), \tag{2.99}$$

while choosing the negative sign gives

$$\int_0^\infty dk \frac{J_1(kr)}{k^2 - k_j^2} = -\frac{1}{k_j^2 r} - \frac{i\pi}{2k_j} H_1^{(2)}(k_j r). \tag{2.100}$$

Here, $H_1^{(1,2)}$ are Hankel functions. How do we know whether to choose the former one or the latter one, or perhaps some linear combination of the two? For this, we need the asymptotic expansions of the Hankel functions at large r [58],

$$H_1^{(1)}(k_j r) \sim \sqrt{\frac{2}{\pi k_j r}} e^{i(k_j r - 3\pi/4)}, \tag{2.101}$$

$$H_1^{(2)}(k_j r) \sim \sqrt{\frac{2}{\pi k_j r}} e^{-i(k_j r - 3\pi/4)}. \tag{2.102}$$

Since the time dependence of $\boldsymbol{\alpha}$ is of the form $e^{-i\omega_L t}\boldsymbol{\alpha}_1$, we see that $H_1^{(1)}$ produces an asymptotic solution $\sim e^{i(k_j r - \omega_L t)}$, which is a wave propagating away from the vortex. On the other hand, $H_1^{(2)}$ produces an asymptotic solution $\sim e^{-i(k_j r + \omega_L t)}$, which is a wave propagating towards the vortex. The latter is unphysical since the vortex is the source of the waves, not a sink. We therefore choose Eq. (2.99). If $k_j^2 < 0$, no such choice is necessary, since the solution obtained using Eq. (2.99) is identical to the solution obtained using Eq. (2.100) due to the properties of the Hankel functions. As a result, we obtain

$$\boldsymbol{\alpha}_0(\boldsymbol{r}) = \vartheta_{v,x}(\varphi)\sin\eta \frac{\boldsymbol{D}_0}{k_0} \left[\frac{i\pi}{2} H_1^{(1)}(k_0 r) - \frac{1}{k_0 r}\right], \tag{2.103}$$

$$\boldsymbol{\alpha}_1(\boldsymbol{r}) = [\vartheta_{v,y}(\varphi) - i\vartheta_{v,x}(\varphi)\cos\eta] \sum_{j=1}^{3} \frac{\boldsymbol{D}_j}{k_j} \left[\frac{i\pi}{2} H_1^{(1)}(k_j r) - \frac{1}{k_j r}\right]. \tag{2.104}$$

Note that both $\boldsymbol{\alpha}_0(\boldsymbol{r})$ and $\boldsymbol{\alpha}_1(\boldsymbol{r})$ are zero at the origin. This means that near the core ($r \ll 1$), the order parameter is that of the static vortex, as we desire.

Using the fact that only k_2 and k_3 are real, the solution far from the core ($r \gg 1$) is given by

$$\boldsymbol{\alpha}(\boldsymbol{r},t) \approx \Re\left\{ [\vartheta_{v,y}(\varphi) - i\vartheta_{v,x}(\varphi)\cos\eta] \sqrt{\frac{\pi}{2r}} \sum_{j=2}^{3} \frac{\boldsymbol{D}_j}{k_j^{3/2}} e^{i(k_j r - \omega_L t - \pi/4)} \right\}. \tag{2.105}$$

We see that the far-field solution consists of waves travelling away from the vortex. Using Eqs. (2.105), (2.77), and (2.65), we can write $\boldsymbol{S}_0$, which measures the deviation of the spin density from the bulk Brinkman–Smith value, as

$$\begin{aligned} \boldsymbol{S}_0(\boldsymbol{r},t) \approx \Re\Big\{ & -i\omega_L\, [\vartheta_{v,y}(\varphi) - i\vartheta_{v,x}(\varphi)\cos\eta] \sqrt{\frac{\pi}{2r}} \\ & \times \mathsf{R}(\eta\hat{\boldsymbol{y}})\mathsf{R}(\omega_L t\hat{\boldsymbol{z}})\mathsf{R}(\boldsymbol{\theta}_{BS}^{(00)}) \cdot \sum_{j=2}^{3} \frac{\boldsymbol{D}_j + i\hat{\boldsymbol{B}} \times \boldsymbol{D}_j}{k_j^{3/2}} e^{i(k_j r - \omega_L t - \pi/4)} \Big\}. \end{aligned} \tag{2.106}$$

We thus see that the vortex radiates spin waves.

In order to gain more insight into the solution, it is instructive to study eigenmodes of the system. The eigenmodes are vector plane waves of the form $\boldsymbol{\alpha} = \boldsymbol{a}e^{i(\boldsymbol{k}\cdot\boldsymbol{r} - \omega t)}$, which satisfy the homogeneous version of Eq. (2.78), that is,

$$\ddot{\boldsymbol{\alpha}} + \omega_L \hat{\boldsymbol{z}} \times \dot{\boldsymbol{\alpha}} + \hat{\boldsymbol{\theta}}_{BS}^{(00)}(\hat{\boldsymbol{\theta}}_{BS}^{(00)} \cdot \boldsymbol{\alpha}) - \nabla^2\boldsymbol{\alpha} = \boldsymbol{0}. \tag{2.107}$$

Substituting the plane wave ansatz yields

$$-\omega^2\boldsymbol{a} - i\omega\omega_L\hat{\boldsymbol{z}} \times \boldsymbol{a} + \hat{\boldsymbol{\theta}}_{BS}^{(00)}(\hat{\boldsymbol{\theta}}_{BS}^{(00)} \cdot \boldsymbol{a}) + k^2\boldsymbol{a} = \boldsymbol{0}, \tag{2.108}$$

which is a linear algebraic equation for $\boldsymbol{a}$. While discussing the eigenmodes, one usually assumes that the wave vector $\boldsymbol{k}$ is given. The unknowns are the dispersion relation $\omega(\boldsymbol{k})$ and the eigenvector $\boldsymbol{a}(\boldsymbol{k})$. In order to guarantee the existence of nontrivial solutions $\boldsymbol{a} \neq \boldsymbol{0}$ in Eq. (2.108), the determinant of the matrix multiplying $\boldsymbol{a}$ has to vanish. This leads to a sixth-order polynomial equation for ω,

$$(\omega^2 - k^2)^2(\omega^2 - k^2 - 1) - \omega_L^2\omega^2\left(\omega^2 - k^2 - \frac{1 + 4\cos\beta}{5}\right) = 0. \tag{2.109}$$

Since there are six solutions to a sixth-order polynomial equation, there are six independent eigenmodes. Looking more closely, the determinant equation (2.109) is actually a third-order equation for ω^2, and therefore the eigenfrequencies come in positive-negative pairs. For real k, the eigenfrequencies are real. We arrange the modes so that $\omega_1(k)$, $\omega_2(k)$, and $\omega_3(k)$ are non-negative, while $\omega_4(k) = -\omega_1(k)$, $\omega_5(k) = -\omega_2(k)$, and $\omega_6(k) = -\omega_3(k)$. Note that the eigenfrequencies depend

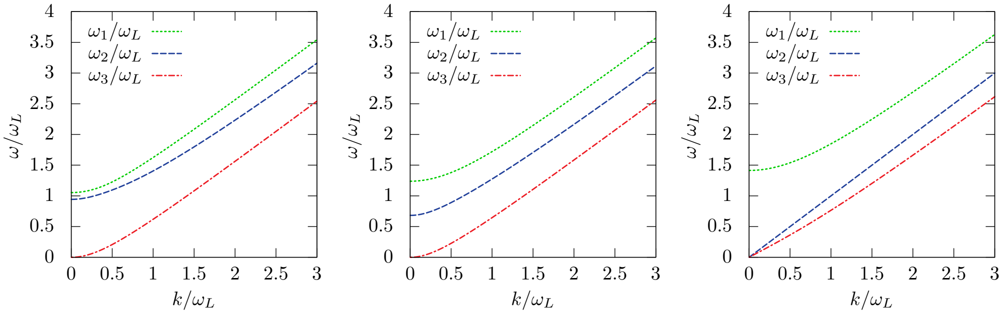

(a) $\omega_L = 1$, $\beta = 10°$ (b) $\omega_L = 1$, $\beta = 50°$ (c) $\omega_L = 1$, $\beta = \theta_L$

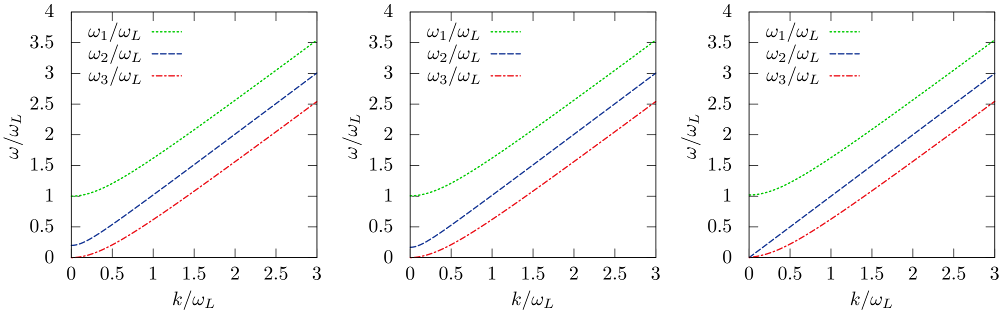

(d) $\omega_L = 5$, $\beta = 10°$ (e) $\omega_L = 5$, $\beta = 50°$ (f) $\omega_L = 5$, $\beta = \theta_L$

Figure 2.5: The positive branches of the dispersion relation of spin waves in the isotropic approximation for different values of ω_L and β, determined by Eq. (2.109).

only on the magnitude of $\boldsymbol{k}$, not on the direction. If $k = 0$, we obtain

$$\omega_1^2(0) = \frac{1+\omega_L^2}{2} + \frac{1}{2\sqrt{5}}\sqrt{5 + 2\omega_L^2(3 - 8\cos\beta) + 5\omega_L^4}, \tag{2.110}$$

$$\omega_2^2(0) = \frac{1+\omega_L^2}{2} - \frac{1}{2\sqrt{5}}\sqrt{5 + 2\omega_L^2(3 - 8\cos\beta) + 5\omega_L^4}, \tag{2.111}$$

$$\omega_3^2(0) = 0. \tag{2.112}$$

These imply that $\omega_1^2(0) \geq \omega_L^2$, $\omega_1^2(0) \geq 1$, $\omega_2^2(0) \leq \omega_L^2$, and $\omega_2^2(0) \leq 1$. At large k, the eigenfrequencies are linear in k, $\omega_i(k) \approx k + b_i$, where $b_1 = \omega_L/2$, $b_2 = 0$, and $b_3 = -\omega_L/2$. Figure 2.5 shows $\omega_1(k)$, $\omega_2(k)$, and $\omega_3(k)$ for different values of the parameters ω_L and β.

How are the eigenmodes related to the vortex problem? The source term $\tilde{\boldsymbol{\rho}}$ on the right-hand side of Eq. (2.78) tries to excite modes with $\omega(k) = 0$ or $\omega(k) = \omega_L$, according to Eq. (2.80). Note that in this case it is the frequency that is fixed, not the wave number. Equation (2.109) can then be used to determine the value (or rather, values) of k for a given ω. For each of the six modes, a solution exists, but it may be complex. A real k corresponds to a propagating wave, while a complex k corresponds to a wave with exponentially decaying amplitude (in r). The general solution can be written as a linear combination of the eigenmodes.

In Eq. (2.103), the vector $\boldsymbol{D}_0$ is an eigenvector of mode 2 at $\omega = 0$ and $k = k_0$. Since k_0 is imaginary, the mode is not propagating. All the other modes are absent from $\boldsymbol{\alpha}_0$ (have zero weight). In Eq. (2.104), the vectors $\boldsymbol{D}_j$ are eigenvectors of modes $j = 1, 2, 3$ at $\omega = \omega_L$ and $k = k_j$. The wavenumber k_1 is imaginary, while k_2 and k_3 are real. Thus, the only propagating modes the vortex can excite are modes 2 and 3, whereas mode 1 is decaying (in space). The reason for this is clear from the dispersion relation. The dispersion curves $\omega_{1,2,3}(k)$ are increasing functions of k (at positive k), so that $\omega_j(k) \geq \omega_j(0)$. We saw that $\omega_1(0) > \omega_L$, while $\omega_{2,3}(0) < \omega_L$. This means that there is no real value of k for which $\omega_1(k) = \omega_L$. On the other hand, there are always real values of k for which $\omega_{2,3}(k) = \omega_L$. The modes $j = 4, 5, 6$ are absent because they correspond to waves travelling towards the vortex core.

2.4.2 High-field approximation

The equation of motion (2.61) can be solved (semi-)analytically also if the magnetic field is high, that is, $\omega_L \gg 1$. In this high-field approximation, c can be non-zero. Inspired by the asymptotic solution (2.105) in the isotropic approximation, let us look for a solution where both temporal and spatial variations of $\boldsymbol{\theta}$ occur at scale $\sim \omega_L^{-1}$. Looking at the left-hand side of Eq. (2.61), we see that the term $\hat{\boldsymbol{\theta}}_{BS}(\hat{\boldsymbol{\theta}}_{BS} \cdot \boldsymbol{\theta})$ is by a factor of ω_L^{-2} smaller than the other terms, and can be neglected. We can thus approximate the equation of motion (2.61) as

$$\ddot{\boldsymbol{\theta}} - \omega_L \hat{\boldsymbol{B}} \times \dot{\boldsymbol{\theta}} - (1+c)\nabla^2 \boldsymbol{\theta} + c\boldsymbol{\nabla}\left(\boldsymbol{\nabla} \cdot \boldsymbol{\theta}\right) \approx \boldsymbol{\rho}. \tag{2.113}$$

Similar to the isotropic approximation, we have been able to transform the equation of motion with time-dependent coefficients into a one with time-independent coefficients. This simplifies the solution procedure significantly.

The source term can be written as

$$\boldsymbol{\rho} = \Re\left\{\boldsymbol{\rho}_0 + e^{-i\omega_L t}\boldsymbol{\rho}_1 + e^{-2i\omega_L t}\boldsymbol{\rho}_2\right\}. \tag{2.114}$$

We seek a solution of the same form, and thus write

$$\boldsymbol{\theta} = \Re\left\{\boldsymbol{\theta}_0 + e^{-i\omega_L t}\boldsymbol{\theta}_1 + e^{-2i\omega_L t}\boldsymbol{\theta}_2\right\}. \tag{2.115}$$

Substituting these into Eq. (2.113) yields

$$-(1+c)\nabla^2 \boldsymbol{\theta}_0 + c\boldsymbol{\nabla}\left(\boldsymbol{\nabla} \cdot \boldsymbol{\theta}_0\right) = \boldsymbol{\rho}_0, \tag{2.116}$$

$$-\omega_L^2 \boldsymbol{\theta}_1 + i\omega_L^2 \hat{\boldsymbol{B}} \times \boldsymbol{\theta}_1 - (1+c)\nabla^2 \boldsymbol{\theta}_1 + c\boldsymbol{\nabla}\left(\boldsymbol{\nabla} \cdot \boldsymbol{\theta}_1\right) = \boldsymbol{\rho}_1, \tag{2.117}$$

$$-4\omega_L^2 \boldsymbol{\theta}_2 + 2i\omega_L^2 \hat{\boldsymbol{B}} \times \boldsymbol{\theta}_2 - (1+c)\nabla^2 \boldsymbol{\theta}_2 + c\boldsymbol{\nabla}\left(\boldsymbol{\nabla} \cdot \boldsymbol{\theta}_2\right) = \boldsymbol{\rho}_2. \tag{2.118}$$

We neglect $\boldsymbol{\theta}_0$ since it is not consistent with our assumption that the temporal variation occurs at scale ω_L^{-1}. This should not cause any problems since $\boldsymbol{\theta}_0$ only determines the static background for $\boldsymbol{\theta}$, and thus we lose no information about the dynamics of $\boldsymbol{\theta}$. Both $\boldsymbol{\theta}_1$ and $\boldsymbol{\theta}_2$ can be solved in the Fourier space. By defining

$$\mathsf{L}_1(\boldsymbol{\nabla}) = -\omega_L^2 \mathsf{I} + i\omega_L^2[\hat{\boldsymbol{B}}]_\times - (1+c)\nabla^2 + c\boldsymbol{\nabla}\boldsymbol{\nabla}, \tag{2.119}$$

$$\mathsf{L}_2(\boldsymbol{\nabla}) = -4\omega_L^2 \mathsf{I} + 2i\omega_L^2[\hat{\boldsymbol{B}}]_\times - (1+c)\nabla^2 + c\boldsymbol{\nabla}\boldsymbol{\nabla}, \tag{2.120}$$

we obtain [cf. Eqs. (2.89) and (2.90)]

$$\boldsymbol{\theta}_n(\boldsymbol{k}) = \mathsf{L}_n^{-1}(i\boldsymbol{k}) \cdot \boldsymbol{\rho}_n(\boldsymbol{k}) = \frac{1}{k}\sum_{j=1}^{3} \frac{\boldsymbol{D}_{n,j}(\varphi_k)}{k^2 - k_{n,j}^2(\varphi_k)}, \tag{2.121}$$

where $n = 1, 2$. The factor $1/k$ comes from $\boldsymbol{\theta}_v(\boldsymbol{k})$, see Eq. (2.23). The wave numbers $k_{n,j}$ depend on φ_k, ω_L, η, and c, but only the dependence on φ_k is indicated explicitly, since this is needed in the following discussion. One of the wave numbers, $k_{1,1}$, is identically zero. This is an artifact caused by our use of the approximate equation of motion (2.113). In reality, $k_{1,1}$ is similar to k_1 of the isotropic approximation, which is purely imaginary and remains bounded at large ω_L, see Fig. 2.3. The remaining $k_{n,j}$ are positive and proportional to ω_L. The vectors $\boldsymbol{D}_{n,j}$ depend on φ_k, ω_L, η, β, and c, as well as on the parameters characterising the vortex core, that is, C_1, C_2, and ζ.

In the position space, the spatial variation of each of the terms in Eq. (2.121) occurs at scale $k_{n,j}^{-1}$. This means that the term proportional to $\boldsymbol{D}_{1,1}$ does not satisfy our initial assumption, and is therefore neglected. Other terms are consistent with the assumption.

The next step is to calculate $\boldsymbol{\theta}_n(\boldsymbol{r})$ by taking the inverse Fourier transform of Eq. (2.121). In the isotropic approximation, the inverse transforms of $\boldsymbol{\alpha}_0(\boldsymbol{k})$ and $\boldsymbol{\alpha}_1(\boldsymbol{k})$ were calculated exactly, see Eqs. (2.95)–(2.104). Here, things are more complicated since the wave numbers $k_{n,j}$ depend on the angle φ_k. We take a different route, and only calculate the asymptotic solution, that is, the solution at $r \gg 1$. This is done (semi-)analytically. By definition,

$$\begin{aligned}
\boldsymbol{\theta}_n(\boldsymbol{r}) &= \frac{1}{(2\pi)^2}\iint d^2k e^{i\boldsymbol{k}\cdot\boldsymbol{r}}\boldsymbol{\theta}_n(\boldsymbol{k}) \\
&= \frac{1}{(2\pi)^2}\int_0^{2\pi} d\varphi_k \int_0^\infty dk k e^{ikr\cos(\varphi-\varphi_k)}\boldsymbol{\theta}_n(k,\varphi_k) \\
&= \frac{1}{(2\pi)^2}\int_0^{2\pi} d\varphi_k \int_0^\infty dk k e^{ikr\cos\varphi_k}\boldsymbol{\theta}_n(k,\varphi_k+\varphi) \\
&= \frac{1}{(2\pi)^2}\sum_j \int_0^{2\pi} d\varphi_k \boldsymbol{D}_{n,j}(\varphi_k+\varphi)\int_0^\infty dk \frac{e^{ikr\cos\varphi_k}}{k^2 - k_{n,j}^2(\varphi_k+\varphi)},
\end{aligned} \tag{2.122}$$

where in the penultimate equality we changed the integration variable from φ_k to $\varphi_k - \varphi$, and used the 2π periodicity of the integrand to change the limits of integration back to $[0, 2\pi]$. Remember that the term $j = 1$ is neglected from the sum for $n = 1$.

To proceed, we need to calculate the integral $\int_0^\infty dk e^{ikr\cos\varphi_k}/(k^2 - k_{n,j}^2)$ (we assume that n and j are fixed). We do this by extending the integration to complex plane. The integration contour we use depends on the sign of $\cos\varphi_k$, since we want the exponential factor to converge, not diverge. If $\cos\varphi_k > 0$, we choose the contour $C_+ = [0, R] \cup C_R^+ \cup [iR, 0]$, where $C_R^+ = \{Re^{is} | s \in [0, \pi/2]\}$ is an arc of a circle of radius $R > 0$ in the first quadrant of the complex plane. Similarly, if $\cos\varphi_k < 0$, we choose the contour $C_- = [0, R] \cup C_R^- \cup [-iR, 0]$, where $C_R^- = \{Re^{is} | s \in [0, -\pi/2]\}$ is an arc of a circle of radius $R > 0$ in the fourth quadrant of the complex plane.

Calculation of the integral over $C_\pm$ requires a detailed consideration of the pole $k_{n,j}$ that lies on the integration contour. We resort again to the standard trick, and add a small imaginary part to $k_{n,j}$, so that $k_{n,j} \to k_{n,j} \pm i\delta$, where $\delta > 0$. Similar to the isotropic approximation, the choice of sign determines the direction of propagation of the wave. The positive sign results in a wave travelling away from the vortex, while the negative sign gives a wave travelling towards the vortex. The former is the correct physical solution, and we therefore choose $k_{n,j} \to \tilde{k}_{n,j} = k_{n,j} + i\delta$.

The integral over $C_\pm$ can be calculated in two ways, either as a sum of integrals over the different parts of the contour or, since the contour is closed, using the residue theorem [57]. Let us first assume that $\cos\varphi_k > 0$. Thus,

$$\begin{aligned}\int_{C_+} dk \frac{e^{ikr\cos\varphi_k}}{k^2 - \tilde{k}_{n,j}^2} &= \int_0^R dk \frac{e^{ikr\cos\varphi_k}}{k^2 - \tilde{k}_{n,j}^2} + \int_{C_R^+} dk \frac{e^{ikr\cos\varphi_k}}{k^2 - \tilde{k}_{n,j}^2} + \int_{iR}^0 dk \frac{e^{ikr\cos\varphi_k}}{k^2 - \tilde{k}_{n,j}^2} \\ &= 2\pi i \mathrm{Res}\left(\frac{e^{ikr\cos\varphi_k}}{k^2 - \tilde{k}_{n,j}^2}, \tilde{k}_{n,j}\right).\end{aligned} \tag{2.123}$$

In the limit $R \to \infty$, the integral over C_R^+ vanishes due to Jordan's lemma [57]. The integral over $[0, R]$ approaches the integral we want to calculate. In the integral over $[iR, 0]$, we make a change of variables $k \to -ik$. The pole $\tilde{k}_{n,j}$ lies inside C_+, and is of first order. Calculating the residue and taking the limits $R \to \infty$ and $\delta \to 0$ leaves us with

$$\int_0^\infty dk \frac{e^{ikr\cos\varphi_k}}{k^2 - k_{n,j}^2} = i\pi \frac{e^{ik_{n,j}r\cos\varphi_k}}{k_{n,j}} - i\int_0^\infty dk \frac{e^{-kr\cos\varphi_k}}{k^2 + k_{n,j}^2}. \tag{2.124}$$

A similar calculation for $\cos\varphi_k < 0$ shows that

$$\int_0^\infty dk \frac{e^{ikr\cos\varphi_k}}{k^2 - k_{n,j}^2} = i\int_0^\infty dk \frac{e^{kr\cos\varphi_k}}{k^2 + k_{n,j}^2}. \tag{2.125}$$

Note that there is no contribution from the residue, since we shifted the pole to the upper half-plane, and therefore there are no poles inside C_-.

Plugging the integrals calculated above into Eq. (2.122) and using the symmetries $k_{n,j}(\varphi_k+\pi)=k_{n,j}(\varphi_k)$, $\boldsymbol{D}_{n,j}(\varphi_k+\pi)=-\boldsymbol{D}_{n,j}(\varphi_k)$, we obtain

$$\begin{aligned}\boldsymbol{\theta}_n(\boldsymbol{r}) = &\frac{i}{4\pi}\sum_j \int_{-\pi/2}^{\pi/2} d\varphi_k \frac{\boldsymbol{D}_{n,j}(\varphi_k+\varphi)}{k_{n,j}(\varphi_k+\varphi)} e^{ik_{n,j}(\varphi_k+\varphi)r\cos\varphi_k} \\ &- \frac{i}{2\pi^2}\sum_j \int_{-\pi/2}^{\pi/2} d\varphi_k \boldsymbol{D}_{n,j}(\varphi_k+\varphi)\int_0^\infty dk \frac{e^{-kr\cos\varphi_k}}{k^2+k_{n,j}^2(\varphi_k+\varphi)}.\end{aligned} \tag{2.126}$$

Here, the first term is dominant if $r \gg 1$. We show that it behaves as $r^{-1/2}$. With some analytic manipulation, one can show that the second term vanishes at least as fast as r^{-1}. We therefore neglect it and approximate

$$\boldsymbol{\theta}_n(\boldsymbol{r}) \approx \frac{i}{4\pi}\sum_j \int_{-\pi/2}^{\pi/2} d\varphi_k \frac{\boldsymbol{D}_{n,j}(\varphi_k+\varphi)}{k_{n,j}(\varphi_k+\varphi)} e^{ik_{n,j}(\varphi_k+\varphi)r\cos\varphi_k}. \tag{2.127}$$

The integral over φ_k is in general impossible to calculate analytically. However, we can again make use of the fact that $r \gg 1$. This allows us to use the method of stationary phase [59]. It states that

$$\int_{-\pi/2}^{\pi/2} dx f(x) e^{ir\Psi(x)} = \sum_l \sqrt{\frac{2\pi}{r|\Psi''(x_l)|}} f(x_l) e^{ir\Psi(x_l)} e^{i\pi \mathrm{sgn}[\Psi''(x_l)]/4} + \mathcal{O}(r^{-1}). \tag{2.128}$$

Here, x_l are the stationary points of the phase Ψ (which is assumed to be twice continuously differentiable) in the interval $[-\pi/2, \pi/2]$. The stationary points are the points where the derivative of the phase vanishes, $\Psi'(x_l)=0$. The second derivative of Ψ is denoted by Ψ'', sgn is the sign function, and f is an arbitrary continuous function. If x_l is one of the end points, an extra factor of $1/2$ is needed for the corresponding term in the sum.

Let us denote $\Psi_{n,j}(\varphi_k) = k_{n,j}(\varphi_k+\varphi)\cos\varphi_k$ and the corresponding stationary points by $\Phi_{n,j,l}$, so that $\Psi'_{n,j}(\Phi_{n,j,l})=0$. Note that the stationary points depend on φ. Using the stationary phase approximation, we obtain

$$\boldsymbol{\theta}_n(\boldsymbol{r}) \approx \frac{i}{\sqrt{8\pi r}} \sum_{j,l} \frac{\exp\left[i\Psi_{n,j,l}r + i\frac{\pi}{4}\mathrm{sgn}\left(\Psi''_{n,j,l}\right)\right]}{k_{n,j,l}\sqrt{\left|\Psi''_{n,j,l}\right|}} \boldsymbol{D}_{n,j,l}. \tag{2.129}$$

Here, $\Psi_{n,j,l}=\Psi_{n,j}(\Phi_{n,j,l})$, $k_{n,j,l}=k_{n,j}(\varphi+\Phi_{n,j,l})$, $\boldsymbol{D}_{n,j,l}=\boldsymbol{D}_{n,j}(\varphi+\Phi_{n,j,l})$, and $\Psi''_{n,j,l}=\Psi''_{n,j}(\Phi_{n,j,l})$. The solution is of a similar form as the asymptotic solution in the isotropic approximation in Eq. (2.105), meaning that the vortex radiates spin waves also in the high-field approximation. Note that the phases $\Psi_{n,j,l}$ generally depend on φ, unlike the wave numbers k_j in the isotropic approximation. This stems from the fact that here in the high-field approximation, we have included also the anisotropic gradient part $\boldsymbol{\nabla\nabla}$ into the equation of motion, and therefore the velocities (both phase and group) of waves depend on the direction of propagation.

2.4.3 Comparison with experiments

We have seen that the Leggett theory of spin dynamics predicts that a vortex line placed in the Brinkman–Smith mode radiates spin waves. This means that the vortex transfers energy from the Brinkman–Smith mode to the spin waves. In order to maintain the Brinkman–Smith mode with constant tipping angle β, a continuous input of energy is needed from the environment. Otherwise, the tipping angle would relax towards zero, that is, the spin density would relax towards the equilibrium value (2.42). We would like to compare this prediction with experimental data [40, 41], which was obtained by studying energy dissipation caused by an array of vortices under uniformly precessing magnetisation.

The vortex array is formed by rotating the vessel containing the superfluid. The areal density n_v of vortices is related to the angular velocity Ω_{rot} of the vessel by $n_v = 2\Omega_{\text{rot}}/\kappa_0$, where $\kappa_0 = \pi\hbar/m$ is the quantum of circulation. This means that the average distance between two neighbouring vortices is $r_v = \sqrt{\hbar/2m\Omega_{\text{rot}}}$. In the experiments, the vessel rotates at $\Omega_{\text{rot}} \sim 1$ rad/s, and so the inter-vortex separation is $r_v \sim 100$ μm. On the other hand, the natural unit of distance we have used is $v/\Omega \approx 5$ μm. The vortices are therefore far apart, and we should be able to treat the system as multiple isolated vortex lines.

The uniformly precessing magnetisation is achieved using the so-called homogeneously precessing domain (HPD) [60, 61]. By introducing a small gradient ($|\boldsymbol{\nabla} B|/B \sim 10^{-3}$ cm^{-1}) to the magnitude of the external static magnetic field, two domains are formed in the vessel. In one domain, the spins are aligned along the magnetic field. In the second domain, the spins precess uniformly about the external magnetic field with tipping angle $\beta \approx \theta_L$. The precession frequency is approximately equal to the Larmor frequency. Between the two domains is a thin domain wall. Due to dissipation, one needs an additional time-dependent magnetic field to maintain the HPD.

In both experiments, a sample of superfluid is contained inside an NMR cell, which is a cylinder of radius 3.5 mm and height 7 mm. The vortex array fills the entire cell, as does the HPD. The experiments of Ref. [41] were done at $p = 29.3$ bar, $B = 14.2$ mT, $\Omega_{\text{rot}} = 1.49$ rad/s, $0.48 \lesssim T/T_c \lesssim 0.64$, and $0 \leq \eta \leq \pi/2$. The transition temperature between the two core structures was $T_v \approx 0.60T_c$, with the double-core vortex stable at lower temperatures. The experiments of Ref. [40] were done at $p = 29.3$ bar, $B \in \{14.2 \text{ mT}, 28.4 \text{ mT}\}$, $\Omega_{\text{rot}} = 1.0$ rad/s, $0.40 \lesssim T/T_c \lesssim 0.70$, and $0 \leq \eta \leq \pi/2$. The transition temperature between the two core structures was $T_v \approx 0.58T_c$, which, for some reason, is slightly less than in Ref. [41].

For theoretical results, we use the tipping angle $\beta = \theta_L$, since this is approximately the value in the HPD. We set $c = 1$ in the high-field approximation. We use $C_2 = C_1$ for the A-phase-core vortex. Based on the numerical structure of the vortex core, $C_2 \ll C_1$ for the double-core vortex, and so we set $C_2 = 0$ for simplicity. Finally, we set $\zeta = \pi/2$, since this is the orientation favoured by the susceptibility anisotropy of the vortex core. Thus, the only free parameter characterising the vortex is C_1.

Let us determine the energy dissipation rate due to spin-wave radiation. In order to do this, we calculate the rate at which the spin waves carry energy through the surface of a cylinder of radius r centered at the vortex axis. This can be done by integrating the energy flux density vector $\mathbf{\Sigma}$ [see Eq. (2.73)] over the surface of the cylinder. Since the system is homogeneous along the vortex axis, the time-averaged energy flux per vortex length is

$$P(r) = \int_0^{2\pi} d\varphi r \langle \Sigma_r(r,\varphi,t)\rangle_t, \tag{2.130}$$

where $\Sigma_r = \mathbf{\Sigma} \cdot \hat{\boldsymbol{r}}$ and $\langle \cdots \rangle_t$ denotes average over time.

In the isotropic approximation, we solved $\boldsymbol{\theta}$ exactly, see Eqs. (2.77), (2.84), (2.103), and (2.104). If $\beta = \theta_L$, the vectors $\boldsymbol{D}_0$ and $\boldsymbol{D}_2$ vanish. The vectors $\boldsymbol{D}_1$ and $\boldsymbol{D}_3$ are given by

$$\boldsymbol{D}_1 = \frac{1}{2\sqrt{1+4\omega_L^4}} \begin{pmatrix} -2i\omega_L^2 \\ -1-\sqrt{1+4\omega_L^4} \\ 0 \end{pmatrix}, \tag{2.131}$$

$$\boldsymbol{D}_3 = \frac{1}{2\sqrt{1+4\omega_L^4}} \begin{pmatrix} 2i\omega_L^2 \\ 1-\sqrt{1+4\omega_L^4} \\ 0 \end{pmatrix}, \tag{2.132}$$

while the wave numbers k_1, k_2, and k_3 are given by

$$k_1 = 2^{-1/2}\sqrt{2\omega_L^2 - 1 - \sqrt{1+4\omega_L^4}}, \tag{2.133}$$

$$k_2 = \omega_L, \tag{2.134}$$

$$k_3 = 2^{-1/2}\sqrt{2\omega_L^2 - 1 + \sqrt{1+4\omega_L^4}}. \tag{2.135}$$

A straightforward calculation shows that the time-averaged energy flux per vortex length can be written as

$$P(r) = P_0\left[1+\tilde{P}(r)\right]. \tag{2.136}$$

Here, the position-dependent function $\tilde{P}$ is given by

$$\tilde{P}(r) = \frac{-2\omega_L}{2\omega_L^2 - 1 + \sqrt{1+4\omega_L^4}} r\left[|k_1| J_1(k_3 r) K_0(|k_1| r) + k_3 J_0(k_3 r) K_1(|k_1| r)\right], \tag{2.137}$$

where K_n is a modified Bessel function of the second kind. Figure 2.6 shows $P/P_0 = 1+\tilde{P}$ as a function of r at different values of ω_L. We see that the radiation is not generated in the core, but in a region of size $r \sim \omega_L^{-1}$ around the

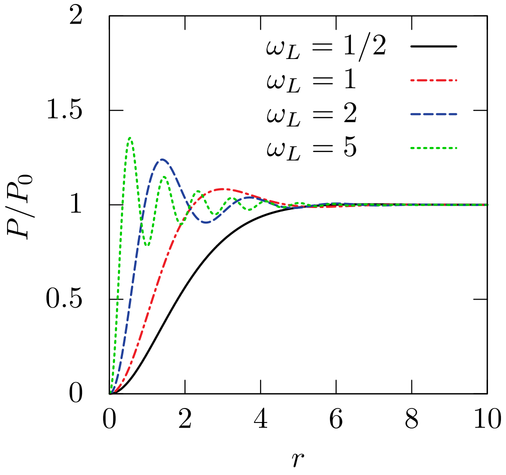

Figure 2.6: The time-averaged energy flux per vortex length P as a function of the radius r in the isotropic approximation, see Eq. (2.136).

core. Moving farther away, there are some transient oscillations due to interference effects. Finally, $\tilde{P}$ vanishes as $e^{-|k_1|r}$ at large r, and thus P approaches P_0 exponentially. This means that P_0 is the total energy dissipation rate per vortex length due to spin-wave radiation for an isolated vortex line, which is the quantity we wanted to determine. It is given by

$$P_0 = \frac{\pi^2}{8}\omega_L \frac{2\omega_L^2 - 1 + \sqrt{1+4\omega_L^4}}{1+4\omega_L^4}(C_2^2 + C_1^2\cos^2\eta). \tag{2.138}$$

This expression is valid for both the A-phase-core vortex ($C_2 = C_1$) and the double-core vortex ($C_2 = 0$).

The experimental value of ω_L at $T = 0.5T_c$ is $\omega_L \approx 2.2$ at $B = 14.2$ mT and twice as large at $B = 28.4$ mT. In both cases, the majority of the transient oscillations of $\tilde{P}$ have decayed at $r \approx 6$, while the inter-vortex separation is $r_v \sim 20$, depending on Ω_{rot}. This shows that the vortices are far apart from the perspective of spin-wave radiation, and therefore the assumption that we can approximate the system as multiple isolated vortices would seem to be a decent one.

A similar calculation can be made also in the high-field approximation. The difference is that we have the solution only at $r \gg 1$. Although we are not able to study what happens at small r, the asymptotic solution is enough to calculate the limiting value $P_0 = \lim_{r\to\infty} P(r)$, that is, the total energy dissipation rate per vortex length due to spin-wave radiation. Analytical result for P_0 seems to be hard to obtain for general η. However, at $\eta = 0$ we obtain

$$P_0 = \frac{\pi^2}{8}\omega_L^{-1}\left[\frac{13}{16}\left(C_1^2 + C_2^2\right) + \frac{3}{8}C_1C_2\right], \tag{2.139}$$

which is again valid for both the A-phase-core vortex and the double-core vortex. A comparison with Eq. (2.138) at $\omega_L \gg 1$ and $\eta = 0$ shows that the two approximations yield equal results for the A-phase-core vortex. For the double-core vortex, the result of Eq. (2.139) is by a factor of 13/16 smaller than the corresponding result of Eq. (2.138).

Let us compare P_0 with the energy dissipation rates observed in the experiments. We use the expression (2.138) obtained in the isotropic approximation, since it is valid for all η and it should be more accurate at low magnetic fields. However, the real value of P_0 is probably slightly smaller due to the fact that $c > 0$ [compare Eqs. (2.138) and (2.139)].

Let us start by considering the dependence of the energy dissipation rate on the external magnetic field $\boldsymbol{B}$, that is, on η and ω_L. Figure 2.7 shows the dependence of P_0 on $\cos^2\eta$. The experimental data is taken from Fig. 2 of Ref. [41], and contains measurements at two temperatures: $T = 0.48T_c$, where only the double-core vortex is stable, and $T = T_v = 0.60T_c$, where both vortex types are stable. As is mentioned in Ref. [41], the measurements seem to obey the relation $P_0(\eta) = a_0 + a_2 \cos^2\eta$, where a_0 and a_2 are temperature-dependent parameters. A similar relationship is predicted by Eq. (2.138), which shows that $a_0 = a_2$ for the A-phase-core vortex and $a_0 = 0$ for the double-core vortex. The experimental values are $a_2/a_0 \approx 1.02$ for the A-phase-core vortex, $a_2/a_0 \approx 4.87$ for the double-core vortex at $T = T_v$, and $a_2/a_0 \approx 10.5$ for the double-core vortex at $T = 0.48T_c$. We see that the prediction for the A-phase-core vortex is in very good agreement with the experiments. The prediction for the double-core vortex is decent, the main difference being that a_0, although small compared to a_2, is not equal to zero in the experiments. A possible reason for this anomaly could be the fact that we assume $C_2 = c = 0$. The theoretical curves shown in Fig. 2.7 are plotted using the values $C_1 = 1.66$ for the A-phase-core vortex, $C_1 = 4.20$ for the double-core vortex at $T = T_v$, and $C_1 = 5.81$ for the double-core vortex at $T = 0.48T_c$. These were obtained from a least-squares fit to the data (as a function of $\cos^2\eta$). The corresponding values of C_1 obtained from the numerical structure of the vortex core are approximately 1.33, 3.00, and 3.86, respectively. The fitted values are thus slightly larger than the ones obtained from theory. The temperature dependence of C_1 for the double-core vortex is similar in both cases: the ratio $C_1(T_v)/C_1(0.48T_c)$ attains the value 0.72 using the parameters C_1 from the theory and 0.78 using the parameters C_1 from the least-squares fit.

The experimental dependence of the energy dissipation rate on ω_L can be obtained from Fig. 1 of Ref. [40]. The figure shows that when the magnetic field is increased from 14.2 mT to 28.4 mT, the measured dissipation rate decreases, which is in agreement with Eq. (2.138). Let us consider the ratio $\varrho = P(28.4\text{mT})/P(14.2\text{mT})$ near T_v. Theory predicts $\varrho = 0.54$ for both vortex types, while the measured value is $\varrho = 0.68$.

Figure 2.8 shows the dependence of the energy dissipation rate per vortex length P_0 on temperature in the case of the double-core vortex. The experimental data is taken from Fig. 1 of Ref. [41]. The theoretical curve shown in Fig. 2.8

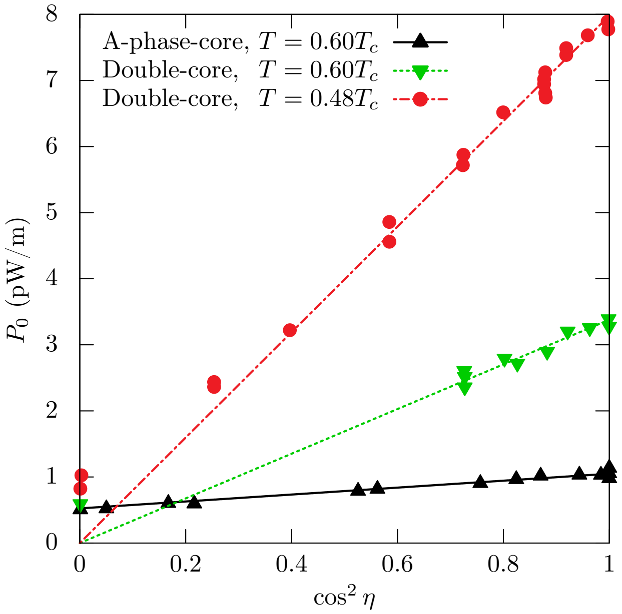

Figure 2.7: The predicted energy dissipation rate per vortex length P_0 in the isotropic approximation [see Eq. (2.138)] as a function of $\cos^2 \eta$ (lines), together with the measured energy dissipation rate per vortex length from Ref. [41] (points). Theoretical lines are plotted using the parameters C_1 obtained from a least-squares fit to the experimental data. As a result, we obtained $C_1 = 1.66$ for the A-phase-core vortex at $T = 0.60T_c$, $C_1 = 5.81$ for the double-core vortex at $T = 0.48T_c$, and $C_1 = 4.20$ for the double-core vortex at $T = 0.60T_c$. The figure was originally published in Pub. III.

assumes that C_1 depends linearly on temperature in the interval $0.48T_c < T < T_v$, so that $C_1(T) = AT/T_c + B$. This should be a decent approximation since the interval is quite narrow. To determine the coefficients A and B, we use the values $C_1(0.48T_c) = 5.81$ and $C_1(T_v) = 4.20$ that we obtained above. These lead to $A = -13.4$ and $B = 12.2$.

One further thing to mention here, discussed in more detail in Pub. III, is the effect of twisting of the double-core vortex on the energy dissipation rate. The precessing magnetisation can rotate the half-cores around each other. At the top and bottom surfaces of the vessel, however, the core is pinned. This may lead to a twisted vortex. We have shown in Pub. III that uniform twisting of the core leads to reduced dissipation. This is in accordance with the experiments of Ref. [41], which show that the energy dissipation rate decreases for twisted vortices.

So far, we have neglected the intrinsic Leggett–Takagi (LT) relaxation mechanism [50] which arises from the conversion of spin between the superfluid component and the normal fluid component (which is always present if $T > 0$) of

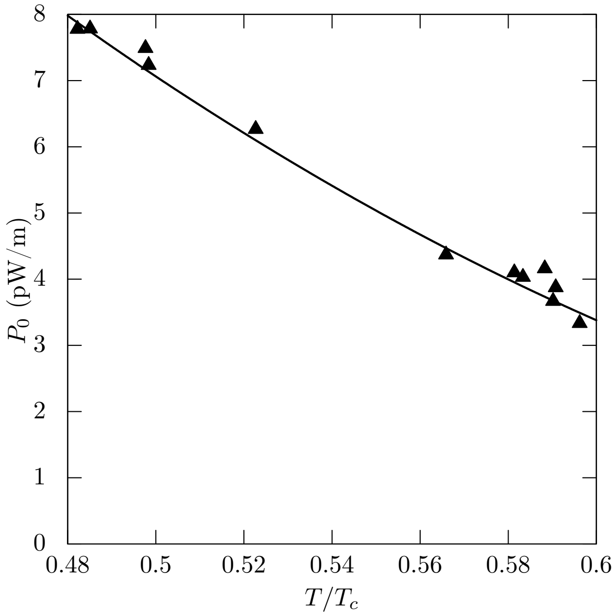

Figure 2.8: The predicted energy dissipation rate per vortex length P_0 in the isotropic approximation [see Eq. (2.138)] as a function of temperature for the double-core vortex (line), together with the measured energy dissipation rate per vortex length from Ref. [41] (points). The theoretical curve assumes that the parameter C_1 depends linearly on temperature in the interval $[0.48T_c, 0.60T_c]$, that is, $C_1(T) = AT/T_c + B$. The coefficients $A = -13.4$ and $B = 12.2$ were calculated using the values $C_1(0.48T_c) = 5.81$ and $C_1(0.60T_c) = 4.20$ that we obtained from the least-squares fit as a function of $\cos^2\eta$, see Fig. 2.7. The figure was originally published in Pub. III.

the liquid. In order to properly take this mechanism into account, one should include it into the equations of spin dynamics. One can, however, estimate its contribution to the energy dissipation rate by using the solution obtained in the absence of the LT mechanism. We have done this in Pub. I, where we solved (approximately) the time average of $\boldsymbol{\theta}$, and used that to estimate the rate of dissipation. A similar calculation can be done using the solution we obtained in the isotropic approximation. The local energy dissipation rate density related to the LT relaxation can be approximated by [50]

$$\begin{aligned} p_{LT} &= -\tilde{\tau}_{LT}|\dot{\boldsymbol{S}} - \boldsymbol{\omega}_L \times \boldsymbol{S}|^2 \\ &= -\tilde{\tau}_{LT}|\ddot{\boldsymbol{\theta}} - \boldsymbol{\omega}_L \times \dot{\boldsymbol{\theta}}|^2 \\ &= -\tilde{\tau}_{LT}|\ddot{\boldsymbol{\alpha}} + \boldsymbol{\omega}_L \times \dot{\boldsymbol{\alpha}}|^2, \end{aligned} \tag{2.140}$$

where $\tilde{\tau}_{LT}$ is the effective Leggett–Takagi relaxation time. We neglect the wave part of $\boldsymbol{\alpha}$, that is, the part proportional to $H_1^{(1)}(k_3 r)$ in Eq. (2.104). The rationale behind this is the following. The wave is generated both with and without the LT mechanism. If the LT mechanism is not included, the wave is not damped, and will carry energy to infinity. If the LT mechanism is included, the wave is damped within some finite radius, and therefore does not carry energy to infinity. However, an equivalent amount of energy is dissipated via the LT mechanism. Thus, the additional dissipation comes from the non-wave-like part of the solution. If we neglect $H_1^{(1)}(k_3 r)$, then $\boldsymbol{\alpha}$ diverges as r^{-1} near the origin. This means that we have to introduce a cut-off radius r_1 near the core, similar to Pub. I. The energy dissipation rate per vortex length due to the LT mechanism, P_{LT}, can be calculated by integrating p_{LT} over the punctured cylinder $r > r_1$. In the leading order in r_1, we obtain

$$P_{LT} \approx -\frac{\pi}{4}\tilde{\tau}_{LT} \log(r_1^{-1})(C_2^2 + C_1^2 \cos^2\eta)\frac{4\omega_L^4}{1+4\omega_L^4}. \tag{2.141}$$

This differs from the result of Pub. I only by the factor $4\omega_L^4/(1+4\omega_L^4)$, which is approximately equal to 1 under the experimental conditions ($\omega_L \gtrsim 1.7$). Thus, the result obtained here is nearly identical to the one obtained in Pub. I, and so the discussion can be based on Pub. I.

The magnitude of P_{LT} contains more uncertainty than P_0 since one needs to know both $\tilde{\tau}_{LT}$ and r_1. The dependence of P_{LT} on η and C_1 is identical to P_0. The dependence of P_{LT} on both the magnetic field B and the temperature T is, however, qualitatively different from P_0 and the experiments. Both P_0 and the experiments show a clear dependence on B and T, whereas P_{LT} does not. We can therefore conclude, based on the qualitative behaviour of the energy dissipation rate, that although the LT mechanism certainly increases the rate of dissipation (by roughly 1 pW/m for the double-core vortex under the experimental conditions of Ref. [41]), radiation of spin waves is a more dominant mechanism.

Chapter 3

Moving cylinder in superfluid ^{3}He

In this chapter, we study the drag force exerted on an object moving in superfluid ^{3}He at zero temperature. In particular, the object we consider is a long, circular cylinder of radius R, moving at constant velocity perpendicular to its axis. In Sec. 3.1, we introduce some important theoretical concepts. In Sec. 3.2, we discuss the problem at a qualitative level. We find that Landau's argument on critical velocity [42] holds true for a microscopic cylinder of radius $R \ll \xi_0$, but a more careful analysis is needed in the case of a macroscopic cylinder of radius $R \gg \xi_0$. In Sec. 3.3, we introduce the theory on a more formal level. In Sec. 3.4, we formulate a diffuse, mesoscopic boundary condition to describe the effect of the cylinder on the superfluid. In Sec. 3.5, we apply the boundary condition to calculate the force exerted on a microscopic cylinder, and find that the critical velocity is indeed the Landau velocity v_L. In Sec. 3.6, we apply the boundary condition to a macroscopic cylinder assuming that there are no collisions between quasiparticles and that the energy gap is isotropic, and find that the critical velocity has increased from v_L to $1.12v_L$. In Sec. 3.7, we study whether quasiparticle collisions could lead to a simple equilibrium with the cylinder, but find that the answer is negative.

3.1 Background

We base our analysis on the quasiclassical formulation of the theory of superfluidity [20]. As we mentioned in the introduction, the Cooper pairs that form the superfluid condensate comprise Landau quasiparticles (the quasiparticles of the Fermi liquid theory) near the Fermi surface. In a purely quantum mechanical theory, the characteristic length and time scales of the system are therefore $\hbar/p_F \sim 0.1$ nm and $\hbar/\epsilon_F \sim 1$ ps, respectively, where p_F is the Fermi momentum and ϵ_F is the Fermi energy. However, practically all interesting physical phenomena related to superfluidity occur at length and time scales much larger than these. The quasiclassical theory makes use of this fact, and integrates out the unnecessary microscopic degrees of freedom.

The characteristic length and time scales of the quasiclassical theory are the coherence length $\xi_0 = \hbar v_F/2\pi k_B T_c \sim 10$ nm and the gap time $\tau_\Delta = \hbar/\Delta \sim 1$ ns. Here, k_B is the Boltzmann constant, v_F is the Fermi velocity, T_c is the superfluid transition temperature, and $\Delta \sim k_B T_c \ll \epsilon_F$ is the average value of the superfluid energy gap. For example, compared to the bulk, the components of the order parameter A are suppressed near a solid wall within a layer of thickness $\sim \xi_0$, while τ_Δ is the natural time scale related to the collective modes of A.

For our purposes, even the quasiclassical scale is too fine. We focus on phenomena occuring at length and time scales that are long compared to ξ_0 and τ_Δ. This approximation of long wave lengths and low frequencies is discussed in Sec. 7 of Ref. [20].

3.1.1 Quasiparticles

The superfluid state can be described using a model of two interpenetrating fluids, superfluid and normal fluid. The Cooper pair condensate constitutes the superfluid part. The normal fluid comprises single-particle excitations known as Bogoliubov quasiparticles [62], which are created in pairs as a Cooper pair breaks. They are composite quasiparticles, superpositions of particle-type and hole-type Landau quasiparticles near the Fermi surface. For the rest of this chapter, the word quasiparticle refers specifically to Bogoliubov quasiparticles.

Quasiparticles move like classical particles, but their internal structure (magnetic character and particle-hole character) must be treated quantum mechanically. There are a total of eight different types of quasiparticles: one nonmagnetic, particle-like quasiparticle; one nonmagnetic, hole-like quasiparticle; three magnetic, particle-like quasiparticles; and three magnetic, hole-like quasiparticles [63]. The magnetic quasiparticles play a central part, for example, in the study of spin dynamics. However, we neglect these in the following, since we do not study magnetic effects.

The mass m^* of a quasiparticle is equal to the mass of a Landau quasiparticle. It is related to the Fermi momentum p_F and the Fermi velocity v_F by $p_F = m^* v_F$, and to the first symmetric Fermi liquid parameter F_1^s by $m^*/m = 1 + F_1^s/3$. The energy of a quasiparticle with momentum $\boldsymbol{p}$ near the Fermi surface is given by [20]

$$\epsilon(\boldsymbol{p}) = \sqrt{[\xi_p + u(\hat{\boldsymbol{p}})]^2 + |\Delta(\hat{\boldsymbol{p}})|^2} + a(\hat{\boldsymbol{p}}). \tag{3.1}$$

Here, u and a are the symmetric $[u(-\hat{\boldsymbol{p}}) = u(\hat{\boldsymbol{p}})]$ and antisymmetric $[a(-\hat{\boldsymbol{p}}) = -a(\hat{\boldsymbol{p}})]$ parts of the quasiparticle potential, respectively, $|\Delta|$ is the magnitude of the superfluid energy gap [with symmetry $|\Delta(-\hat{\boldsymbol{p}})| = |\Delta(\hat{\boldsymbol{p}})|$], and $\xi_p \approx v_F(p - p_F)$. The quasiclassical approximation assumes that all the relevant energies are small compared to the Fermi energy $\epsilon_F = p_F v_F/2$, so that $u, a, |\Delta|, \xi_p \ll \epsilon_F$. Figure 3.1 shows a schematic picture of the dispersion relation $\epsilon(\boldsymbol{p})$ as a function of p at fixed $\hat{\boldsymbol{p}}$. We see from Eq. (3.1) that the minimum energy of a quasiparticle in the

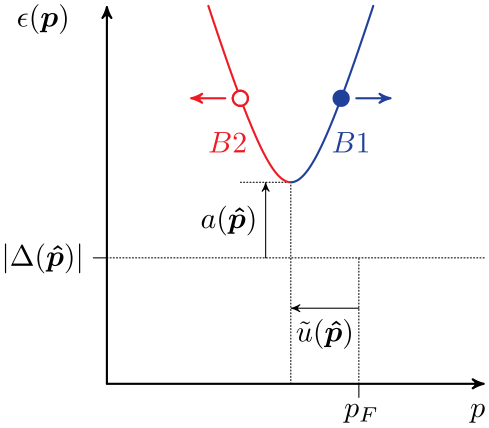

Figure 3.1: A schematic representation of the energy spectrum (3.1) at fixed $\hat{\boldsymbol{p}}$. We have denoted $\tilde{u}(\hat{\boldsymbol{p}}) = u(\hat{\boldsymbol{p}})/v_F$. There are two branches in the spectrum. The quasiparticles from the branch $B1$ are particle-like, and their group velocities point along $\hat{\boldsymbol{p}}$. The quasiparticles from the branch $B2$ are hole-like, and their group velocities point along $-\hat{\boldsymbol{p}}$.

direction $\hat{\boldsymbol{p}}$ is $|\Delta(\hat{\boldsymbol{p}})| + a(\hat{\boldsymbol{p}})$. This is attained at the Fermi surface $\xi_p + u(\hat{\boldsymbol{p}}) = 0$, where $p = p_F(1 - u/2\epsilon_F) \approx p_F$. Note that the symmetric quasiparticle potential u shifts the Fermi surface slightly from p_F. In general, u, a, and $|\Delta|$ can also depend on position and time. We discuss how to calculate them in Sec. 3.3.

The motion of a quasiparticle can be determined by treating the energy (3.1) as an effective Hamiltonian [64]. The equations of motion are then the familiar Hamiltonian equations [52]

$$\dot{\boldsymbol{q}} = \frac{\partial \epsilon}{\partial \boldsymbol{p}}, \tag{3.2}$$

$$\dot{\boldsymbol{p}} = -\frac{\partial \epsilon}{\partial \boldsymbol{q}}, \tag{3.3}$$

where $\boldsymbol{q}$ denotes the position of the quasiparticle. Equation (3.2) shows that the quasiparticle moves at group velocity

$$\boldsymbol{v}_G = \frac{\partial \epsilon}{\partial \boldsymbol{p}} \approx v_F \frac{\xi_p + u}{\sqrt{(\xi_p + u)^2 + |\Delta|^2}} \hat{\boldsymbol{p}}. \tag{3.4}$$

Here, we have kept only the leading order terms in small quantities u/ϵ_F, a/ϵ_F, $|\Delta|/\epsilon_F$, and ξ_p/ϵ_F, in the spirit of the quasiclassical approximation. We see that the magnitude of the group velocity is of the order of the Fermi velocity v_F (assuming that the quasiparticle is not directly at the Fermi surface). Outside the Fermi surface, $\xi_p + u > 0$, the quasiparticles are particle-like. Their group velocities point along $\hat{\boldsymbol{p}}$. We say that these belong to branch $B1$. Inside the Fermi surface, $\xi_p + u < 0$, the quasiparticles are hole-like, and their group velocities point in the direction opposite to $\hat{\boldsymbol{p}}$. We say that these belong to branch $B2$. The two branches are also indicated in Fig. 3.1.

How does the momentum of a quasiparticle change as it moves around? This can be determined from Eq. (3.3). Let us assume that u, a, and $|\Delta|$ are of the order of the B phase energy gap Δ_B (or any energy of similar magnitude), and that they vary in space at length scale r (we neglect time dependence for simplicity). It takes time $\delta t \sim r/v_F$ for the quasiparticle to travel the distance r. A short calculation using Eq. (3.3) shows that $|\dot{\xi}_p| \sim v_F \Delta_B / r$ and $|\dot{\hat{\boldsymbol{p}}}| \sim \Delta_B / p_F r$. We can therefore estimate that the quantities ξ_p and $\hat{\boldsymbol{p}}$ change by $|\delta \xi_p| \sim |\dot{\xi}_p| \delta t \sim \Delta_B$ and $|\delta \hat{\boldsymbol{p}}| \sim |\dot{\hat{\boldsymbol{p}}}| \delta t \sim \Delta_B / p_F v_F \ll 1$, respectively, as the quasiparticle moves. This shows that the relative change in ξ_p can be large, but the direction $\hat{\boldsymbol{p}}$ is more or less constant. In the absence of explicit time dependence, the energy of the quasiparticle remains constant during the motion, and so ξ_p can also be determined directly from Eq. (3.1).

The spatial dependence of a or $|\Delta|$ can lead to an interesting phenomenon known as Andreev reflection [65]. It is possible that a quasiparticle with energy ϵ (which is constant in the absence of explicit time dependence) heads towards a region where $|\Delta| + a > \epsilon$. According to Eq. (3.1), however, this condition is impossible to fulfill, and so the quasiparticle cannot enter such a region. Instead, it is reflected at the boundary $|\Delta| + a = \epsilon$. The reflection is an unusual one. In an ordinary reflection from a solid boundary, the normal component of the momentum of the quasiparticle would flip. In an Andreev reflection, however, the momentum changes only slightly, from one side of the Fermi surface to the other, so that the branch of the quasiparticle changes from $B1$ to $B2$, or vice versa. Consequently, Eq. (3.4) shows that the group velocity is reversed, and thus the quasiparticle undergoes a retroreflection, avoiding the restricted region. A good review on Andreev reflection in superfluid ^{3}He can be found in Ref. [66].

The quasiparticle states in the phase space are occupied according to the distribution function $n(\boldsymbol{p}, \boldsymbol{r}, t)$. In thermal equilibrium, this is given by the Fermi distribution [20], $n = 1/(1+e^{\epsilon/k_B T})$, where ϵ is defined by Eq. (3.1). Instead of the momentum $\boldsymbol{p}$, it is often convenient to choose the energy ϵ and the direction of the momentum $\hat{\boldsymbol{p}}$ as the independent variables. The relation between p and ϵ is given by Eq. (3.1). We see that (see also Fig. 3.1) for a given energy $\epsilon > |\Delta| + a$, there are two values of p which satisfy the equation, $p = p_\pm = p_F \pm \sqrt{(\epsilon - a)^2 - |\Delta|^2}/v_F - u/v_F$. Here, p_+ corresponds to the branch $B1$, while p_- corresponds to the branch $B2$. This means that we need separate distribution functions for the two branches. We denote these by $n_{B1}(\hat{\boldsymbol{p}}, \epsilon, \boldsymbol{r}, t)$ and $n_{B2}(\hat{\boldsymbol{p}}, \epsilon, \boldsymbol{r}, t)$. Note that these are physically meaningful only when $\epsilon \geq a(\hat{\boldsymbol{p}}, \boldsymbol{r}, t) + |\Delta(\hat{\boldsymbol{p}}, \boldsymbol{r}, t)|$. In thermal equilibrium, $n_{Bi} = 1/(1 + e^{\epsilon/k_B T})$.

3.1.2 Semiconductor and excitation pictures

So far, we have described the superfluid state using the so-called quasiparticle picture, where the reference state is the pure superfluid (no normal fluid present). A single quasiparticle with momentum $\boldsymbol{p}$ changes the momentum of the system by $\boldsymbol{p}$ and the energy by $\epsilon(\boldsymbol{p})$. The change in energy can be either positive or negative: even though the square root in Eq. (3.1) is always positive, negative a can result in negative ϵ.

Another way to describe the superfluid state is to use the so-called semiconductor picture [67]. In the semiconductor picture, for every quasiparticle state S with momentum $\boldsymbol{p}$, energy ϵ, and branch i $(= 1, 2)$, there is a corresponding state $\tilde{S}$ with momentum $-\boldsymbol{p}$, energy $-\epsilon$, and branch $3 - i$. If a state S is empty, the corresponding state $\tilde{S}$ is full, and vice versa. The number of states has therefore doubled compared to the quasiparticle picture, but the physical information is still the same. In pure superfluid, the states $\tilde{S}$ are filled, while the states S are empty. The energy spectrum is given by

$$\epsilon(\boldsymbol{p}) = \pm\sqrt{[\xi_p + u(\hat{\boldsymbol{p}})]^2 + |\Delta(\hat{\boldsymbol{p}})|^2} + a(\hat{\boldsymbol{p}}). \tag{3.5}$$

Here, the branch with the plus sign in front of the square root represents the states S, while the branch with the minus sign represents the states $\tilde{S}$. Figure 3.2 shows a schematic picture of the spectrum (3.5) as a function of p at fixed $\hat{\boldsymbol{p}}$. Note that, in Fig. 3.2, the states $B2$ $(B1)$ in the lower part of the spectrum are not the ones corresponding to the states $B1$ $(B2)$ in the upper part of the spectrum since both have the same direction of momentum $\hat{\boldsymbol{p}}$.

Just as in the quasiparticle picture, we introduce distribution functions to specify how the states are occupied. We denote these (in the energy representation) by $\phi_{B1}(\hat{\boldsymbol{p}}, \epsilon, \boldsymbol{r}, t)$ and $\phi_{B2}(\hat{\boldsymbol{p}}, \epsilon, \boldsymbol{r}, t)$. Equation (3.5) shows that $\epsilon \geq a + |\Delta|$ for states S, while $\epsilon \leq a - |\Delta|$ for states $\tilde{S}$. This means that the distribution functions are physically relevant only when $|\epsilon - a(\hat{\boldsymbol{p}}, \boldsymbol{r}, t)| \geq |\Delta(\hat{\boldsymbol{p}}, \boldsymbol{r}, t)|$. We talk more about the distribution functions in Sec. 3.3.

In the semiconductor picture, each physical state is taken into account twice, since saying that a state S is full is equivalent to saying that the corresponding state $\tilde{S}$ is empty, and vice versa. This problem is avoided in the quasiparticle picture by considering only the states S. A third way to describe the superfluid state, also avoiding the double representation, is to use the semiconductor picture, but to consider only the states with non-negative energies, that is, excitations. This is called the excitation picture [67]. In the excitation picture, the reference state is the true zero-temperature ground state. The energy spectrum is still given by Eq. (3.5), but only the states whose energy is greater than or equal to zero are taken into account. The distribution functions are the same as in the semiconductor picture, but restricted to $\epsilon \geq 0$. Figure 3.3 shows the difference between the three pictures. If $|a| \leq |\Delta|$, the quasiparticle picture and the excitation picture are identical. If $|a| > |\Delta|$, all pictures differ from each other.

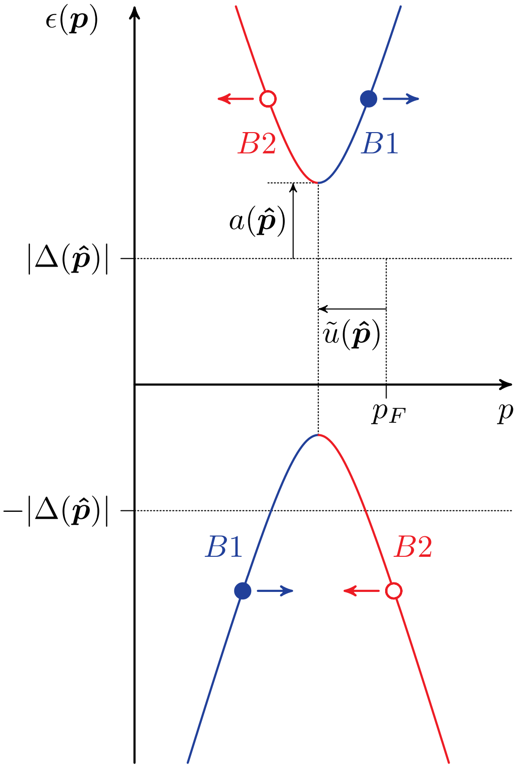

Figure 3.2: A schematic representation of the energy spectrum in the semiconductor picture, Eq. (3.5), at fixed $\hat{\boldsymbol{p}}$. We have denoted $\tilde{u}(\hat{\boldsymbol{p}}) = u(\hat{\boldsymbol{p}})/v_F$.

3.2 Pair breaking by a moving object

We are ready for a qualitative discussion of the problem. We are interested in the force exerted on an object moving in a zero-temperature superfluid. More specifically, the object we study is a long, circular cylinder of radius R, moving at constant velocity perpendicular to its axis. Let us define two frames of reference. The laboratory frame is the frame in which the superfluid is at rest in the absence of the moving object. We fix the Cartesian coordinate axes of the laboratory frame so that $\hat{\boldsymbol{z}}$ points along the cylinder axis and the velocity of the cylinder is $\boldsymbol{v} = v\hat{\boldsymbol{x}}$. The object frame is the rest frame of the cylinder, with the origin at the centre of the cylinder. We choose the basis vectors of the Cartesian coordinate system to coincide with those of the laboratory frame. In addition to the Cartesian coordinate system, we introduce the standard cylindrical coordinate system (r, φ, z) in the object frame. Due to the length of the cylinder, we can assume that the system is translationally invariant in the z direction, and thus no physical variables depend on z. In order to simplify the discussion, we assume

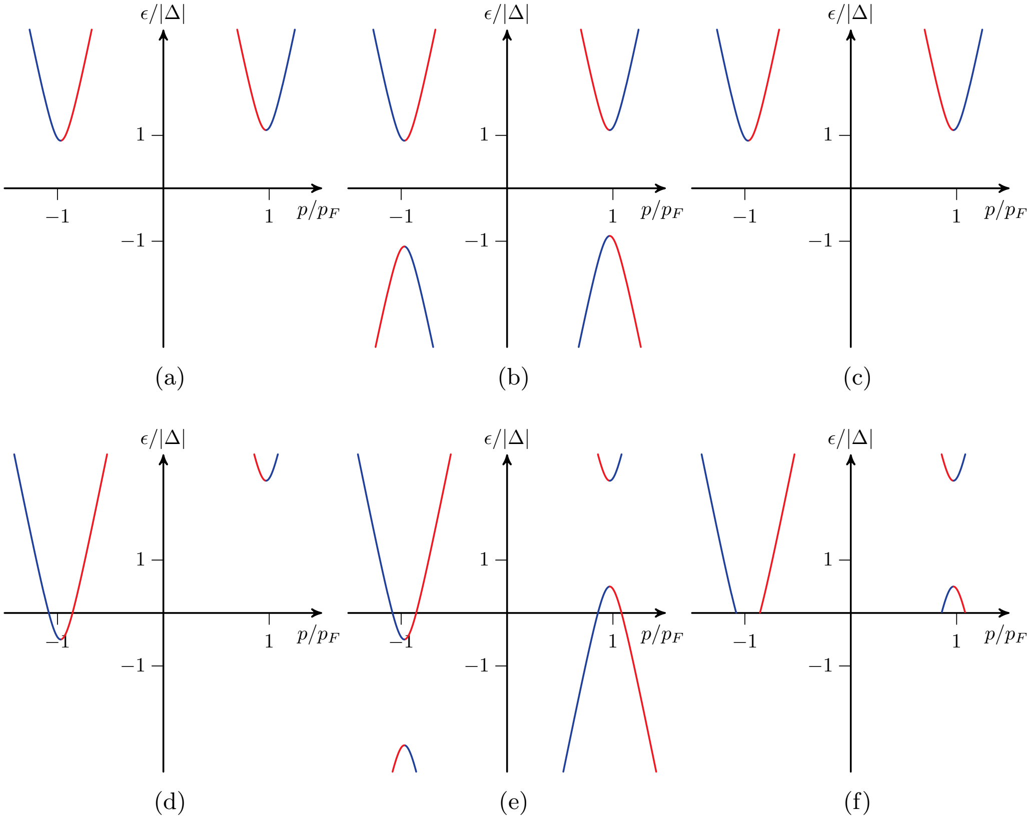

Figure 3.3: A comparison between the energy spectra $\epsilon(\boldsymbol{p})$ in different pictures of superfluidity. We plot $\epsilon(p\hat{\boldsymbol{p}})$ with fixed direction $\hat{\boldsymbol{p}}$ as a function of p in the quasiparticle picture [Eq. (3.1)] assuming (a) $0 < a(\hat{\boldsymbol{p}}) < |\Delta(\hat{\boldsymbol{p}})|$ and (d) $a(\hat{\boldsymbol{p}}) > |\Delta(\hat{\boldsymbol{p}})|$; in the semiconductor picture [Eq. (3.5)] assuming (b) $0 < a(\hat{\boldsymbol{p}}) < |\Delta(\hat{\boldsymbol{p}})|$ and (e) $a(\hat{\boldsymbol{p}}) > |\Delta(\hat{\boldsymbol{p}})|$; and in the excitation picture [Eq. (3.5), $\epsilon \geq 0$] assuming (c) $0 < a(\hat{\boldsymbol{p}}) < |\Delta(\hat{\boldsymbol{p}})|$ and (f) $a(\hat{\boldsymbol{p}}) > |\Delta(\hat{\boldsymbol{p}})|$.

that the gap is isotropic, $|\Delta(\hat{\boldsymbol{p}})| = \Delta$.

What causes the drag on an object as it moves through the superfluid? In general, the force arises from exchange of momentum between the object and the fluid. For example, if a quasiparticle with momentum $\boldsymbol{p}$ collides with the object and as a result scatters to a state with momentum $\tilde{\boldsymbol{p}}$, conservation of momentum requires that the momentum of the object changes by $\delta\boldsymbol{P} = \boldsymbol{p} - \tilde{\boldsymbol{p}}$. If there is, on average, one such collision in a time interval δt, the average force exerted on the object by the fluid is $\boldsymbol{F} = \delta\boldsymbol{P}/\delta t$. To maintain constant velocity, one needs to apply an external force $-\boldsymbol{F}$ on the object. In addition to colliding quasiparticles, momentum is also exhanged if the object breaks Cooper pairs, thus creating quasiparticles which carry momentum. It is important to note, however, that creating bound quasiparticles does not contribute to the force, at least significantly. A bound quasiparticle does not have enough energy to escape from the vicinity of the object to the bulk superfluid. Instead, it undergoes an Andreev reflection at some point along its trajectory. As we discussed in Sec. 3.1.1, Andreev reflection reverses the group velocity of the quasiparticle without affecting the direction of momentum. The magnitude of the momentum changes from one side of the Fermi surface to the other, but the amount of change is minuscule compared to the Fermi momentum p_F. After the Andreev reflection, the quasiparticle returns to the object, giving back the momentum that was lost at the emission.

Let us first consider a microscopically thin cylinder with radius $R \ll \xi_0$. The cylinder acts as a strong perturbing potential for the superfluid, and is able to break Cooper pairs. The situation here is similar to the case of an ion, see, for example, Refs. [68, 20, 69]. The gap is suppressed from the bulk value Δ in the immediate vicinity of the cylinder (at distances $\lesssim \xi_0$). This means that, in addition to the bulk quasiparticle states, there are also bound quasiparticle states near the object. We shall neglect the bound states, since they do not contribute to the force or affect the critical velocity [69].

Let us consider the process of Cooper pair breaking in an inertial frame of reference initially coinciding with the object frame. As a pair breaks, two quasiparticles are created with momenta $\boldsymbol{p}_1$ and $\boldsymbol{p}_2$, and energies $\epsilon(\boldsymbol{p}_1)$ and $\epsilon(\boldsymbol{p}_2)$. If the process is elastic, both momentum and energy are conserved,

$$\mathbf{0} = M\delta\boldsymbol{v} + \boldsymbol{p}_1 + \boldsymbol{p}_2, \tag{3.6}$$

$$0 = \frac{1}{2}M\delta v^2 + \epsilon(\boldsymbol{p}_1) + \epsilon(\boldsymbol{p}_2). \tag{3.7}$$

Here, M is the mass of the cylinder and $\delta\boldsymbol{v}$ denotes the change in the velocity of the cylinder. Eliminating $\delta\boldsymbol{v}$, we obtain

$$\epsilon(\boldsymbol{p}_1) + \epsilon(\boldsymbol{p}_2) = -\frac{|\boldsymbol{p}_1 + \boldsymbol{p}_2|^2}{2M}. \tag{3.8}$$

The energies $\epsilon(\boldsymbol{p}_i)$ are naturally measured in units of Δ. Let us compare the magnitude of the right-hand side to Δ. First of all, we can approximate $p_i \approx p_F$, and so $|\boldsymbol{p}_1 + \boldsymbol{p}_2|^2/2M\Delta \sim p_F^2/M\Delta = 2(\epsilon_F/\Delta)(m^*/M)$. The ratio of the Fermi energy to the energy gap is $\epsilon_F/\Delta \sim 10^3$. The ratio m^*/M, on the other hand, should be many orders of magnitude smaller than unity. For example, assume that the radius of the cylinder is ~ 1 nm, the density of the cylinder is $\sim 10^3$ kg/m^3, and the length of the cylinder is ~ 1 cm. Then $M \sim 10^{-17}$ kg, and thus $m^*/M \sim 10^{-9}$. In any case, $|\boldsymbol{p}_1 + \boldsymbol{p}_2|^2/2M$ is vanishingly small compared to Δ, and can be simply neglected. This leads to the condition

$$\epsilon(\boldsymbol{p}_1) + \epsilon(\boldsymbol{p}_2) = 0. \tag{3.9}$$

We find in Sec. 3.3.2 that $u = 0$ and $a = -p_F\boldsymbol{v}\cdot\hat{\boldsymbol{p}}$ in the object frame, meaning that $\epsilon(\boldsymbol{p}) = \sqrt{\xi_p^2 + \Delta^2} - p_F\boldsymbol{v}\cdot\hat{\boldsymbol{p}}$. The minimum energy of a quasiparticle is therefore

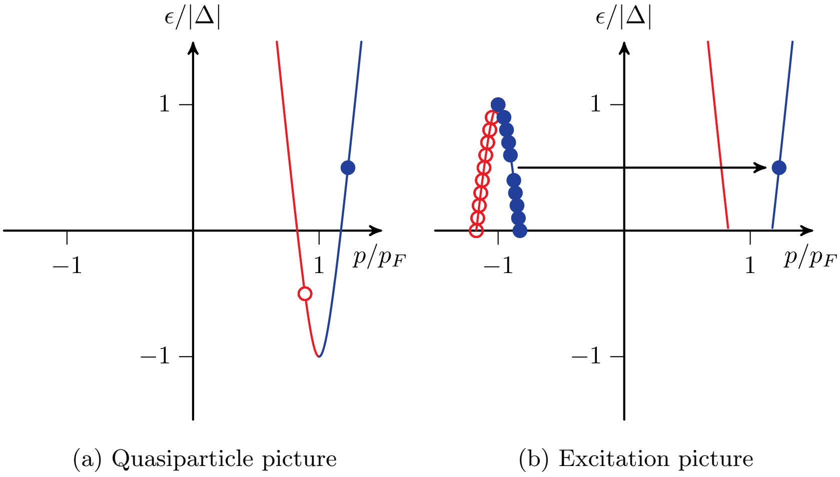

(a) Quasiparticle picture (b) Excitation picture

Figure 3.4: Cooper pair breaking by a moving object in (a) the quasiparticle picture and (b) the excitation picture, seen from the rest frame of the object. In the quasiparticle picture, the pair breaking creates two quasiparticles with opposite energies. In the excitation picture, the pair breaking can be represented as an elastic scattering of an excitation.

$\Delta - p_F v$, and it is attained at $p = p_F$, $\hat{\boldsymbol{p}} = \hat{\boldsymbol{v}}$. Equation (3.9) can be satisfied only if this minimum energy is less than or equal to zero. This is the case if $v \geq v_L$, where

$$v_L = \frac{\Delta}{p_F} \tag{3.10}$$

is the Landau velocity [42]. At velocities larger than v_L, Eq. (3.9) shows that quasiparticles can be created at energies $\Delta - p_F v \leq \epsilon \leq p_F v - \Delta$. At fixed energy ϵ, quasiparticles can be created in a cone $\hat{\boldsymbol{p}} \cdot \hat{\boldsymbol{v}} \geq (\Delta - \epsilon)/p_F v$.

In the excitation picture, a filled quasiparticle state S with negative energy $-\epsilon$ is represented by an empty excitation state $\tilde{S}$ with positive energy ϵ (with opposite momentum and branch). This means that pair breaking can be represented as a simple elastic scattering from a filled, positive-energy state $\tilde{S}$ to an empty state S with equal energy. Figure 3.4 shows an example pair breaking process in both the quasiparticle picture and the excitation picture.

Let us consider a macroscopic cylinder with radius $R \gg \xi_0$. Similar to the microscopic cylinder, the macroscopic cylinder can break Cooper pairs. The gap is suppressed within approximately a coherence length from the surface [19, 20, 1]. We call this region the surface layer. Due to the gap suppression, there are bound quasiparticle states in the surface layer. Unlike the microscopic cylinder, the macroscopic cylinder also affects the fluid outside the surface layer. If the cylinder moves, it has to push the fluid from its path. Conservation of mass then leads to spatial variation of the flow field in a region of size $\sim R$ around the cylinder. We call this the near region. At distances $r \gg R$, the fluid is unaffected

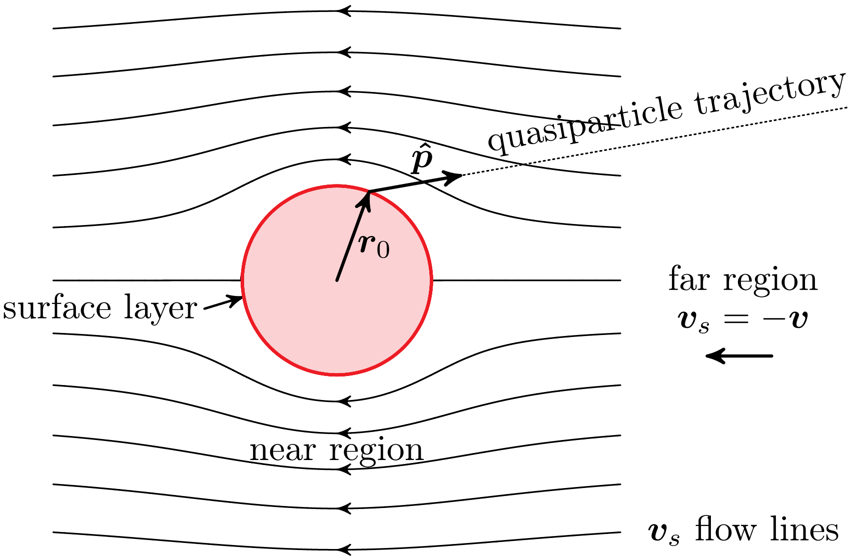

Figure 3.5: Flow around a macroscopic cylinder as seen from the rest frame of the cylinder.

by the cylinder. We call this the far region.

As long as no quasiparticles can escape the surface layer, the superfluid velocity field outside the surface layer is that of an irrotational, incompressible ideal fluid (at zero temperature, the only source of quasiparticles is the cylinder). Seen from the object frame, the flow is static and the superfluid velocity is given by [70, 71]

$$\boldsymbol{v}_s = v\cos\varphi\left(\frac{R^2}{r^2}-1\right)\hat{\boldsymbol{r}} + v\sin\varphi\left(\frac{R^2}{r^2}+1\right)\hat{\boldsymbol{\varphi}}. \tag{3.11}$$

The symmetric and antisymmetric quasiparticle potentials for ideal fluid are $u = 0$ and $a = p_F \boldsymbol{v}_s \cdot \hat{\boldsymbol{p}}$, as we show in Sec. 3.3.2. The flow velocity at top and bottom surfaces ($r = R$, $\varphi = \pm\pi/2$) is $2v$, and thus the flow remains ideal up to $v = v_L/2$. At higher velocities, quasiparticles are generated by the cylinder in regions on the surface where the local flow velocity exceeds the Landau velocity. The quasiparticles modify the flow field, making it non-ideal although still irrotational. Furthermore, the form of a becomes more complicated. We shall consider two approximations to calculate the flow field (by which we mean both $\boldsymbol{v}_s$ and a) in the following sections. The main point here, however, is the fact that the flow field varies in space in the near region. Figure 3.5 shows an illustration of the flow field seen form the object frame.

Consider a straight-line trajectory $\boldsymbol{r} = \boldsymbol{r}_0 + s\hat{\boldsymbol{p}}$, $s \in \mathbb{R}$, where $\boldsymbol{r}_0$ is a point on the surface of the cylinder. An example trajectory is shown in Fig. 3.5. A quasiparticle with momentum direction $\pm\hat{\boldsymbol{p}}$ will travel along this trajectory, unless it collides

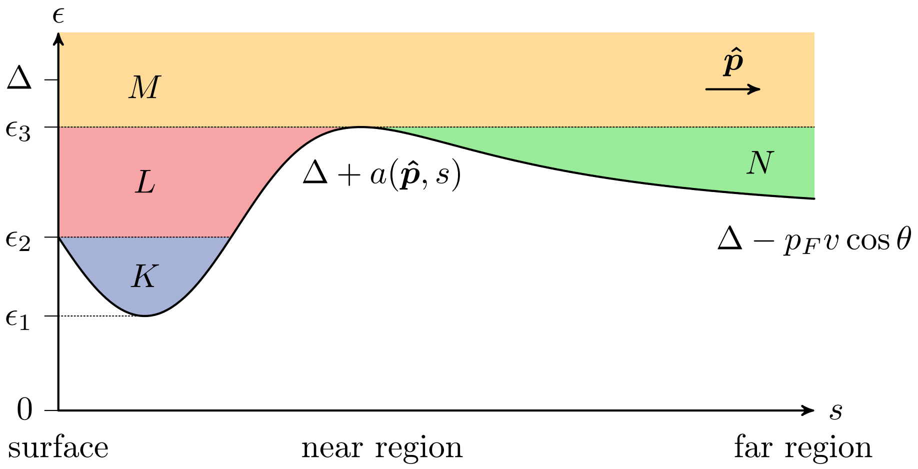

Figure 3.6: Possible variation of $a + \Delta$ along the trajectory shown in Fig. 3.5. The quasiparticle states are divided into different categories, denoted by K, L, M, and N. Quasiparticles in category M are able to move freely between the surface of the cylinder and the far region. Quasiparticles in category N cannot reach the surface of the cylinder. Quasiparticles in category L cannot reach the far region. Finally, quasiparticles in category K are localised somewhere in the flow field. They can reach neither the surface of the cylinder nor the far region.

with another quasiparticle. Figure 3.6 shows a possible variation of $a + \Delta$ along the trajectory. Since $a + \Delta$ is the local minimum energy of a quasiparticle, no quasiparticle states exist below the curve $\epsilon = a + \Delta$. The variation of a along the trajectory divides the quasiparticle states into different categories, denoted by K, L, M, and N in the figure. This has two important implications.

First of all, the flow field can shield the cylinder from incoming quasiparticles. If a quasiparticle (of type $B2$ in Fig. 3.6) from category N approaches the cylinder from the far region, it is Andreev reflected before it can reach the surface. Only quasiparticles with high enough energy (category M) are able to collide with the cylinder. The effect of spatially varying flow field on the damping force due to thermal quasiparticles has been studied in Refs. [72, 73, 74, 75].

The second consequence, more important to us since there are no thermal quasiparticles at zero temperature, is that not all quasiparticles created by the cylinder can escape from the near region, not even if their energy would be sufficient for them to exist in the far region. Consider the example trajectory depicted in Fig. 3.6. The minimum energy that a quasiparticle created by the surface can have is ϵ_2. At energies $\epsilon_2 \leq \epsilon \leq \epsilon_3$ (category L), the quasiparticles are bound to the near region because they do not have enough energy to overcome the potential barrier formed by $a + \Delta$. These do not contribute to the force exerted on the cylinder. Only at higher energies ($\epsilon > \epsilon_3$, category M) are the quasiparticles able to escape to the far region, thus transferring momentum away from the cylinder.

Let us denote $\boldsymbol{v}_0 = \boldsymbol{v}_s(\boldsymbol{r}_0)$. As we have already seen before, if the magnitude of $\boldsymbol{v}_0$ exceeds the Landau velocity, Cooper pair breaking and quasiparticle creation become energetically possible at energies $\Delta - p_F v_0 \leq \epsilon \leq p_F v_0 - \Delta$ (we use the ideal fluid value $a = p_F \boldsymbol{v}_s \cdot \hat{\boldsymbol{p}}$ for simplicity). It would therefore appear that if $p_F v_0 - \Delta$ exceeds ϵ_3, the moving cylinder creates quasiparticles of category M, and thus the critical velocity for the cylinder is the smallest velocity at which $\epsilon_3 \leq p_F v_0 - \Delta$, with all positions $\boldsymbol{r}_0$ and directions $\hat{\boldsymbol{p}}$ taken into account. There is, however, a catch. In order to create a quasiparticle with energy $\epsilon > 0$, one also has to create a quasiparticle with energy $-\epsilon < 0$, see Eq. (3.9). Due to their fermionic nature, two quasiparticles cannot occupy the same state simultaneously (Pauli exclusion principle). This implies that if all the states with energy $-\epsilon$ are already full, it is impossible to break a Cooper pair in a manner which produces a quasiparticle with energy ϵ. As a consequence, in steady state, the cylinder can break a Cooper pair only if the created quasiparticles both belong to category M. If either one would belong to category L, it would be a bound quasiparticle, and this state would already be filled during the transient phase, preventing further pair breaking. If both quasiparticles belong to category M, they are able to escape to the far region, therefore emptying the states, and thus enabling further pair breaking. This is possible only if $\epsilon_3 \leq 0$. The true critical velocity for the cylinder is thus the smallest velocity at which ϵ_3 changes from positive to negative, with all positions $\boldsymbol{r}_0$ and directions $\hat{\boldsymbol{p}}$ taken into account.

As an example, let us consider the ideal flow field [$a = p_F \boldsymbol{v}_s \cdot \hat{\boldsymbol{p}}$ and $\boldsymbol{v}_s$ is given by Eq. (3.11)]. The energy ϵ_3 is defined as the maximum of $a + \Delta$ along the trajectory $\boldsymbol{r} = \boldsymbol{r}_0 + s\hat{\boldsymbol{p}}$ (see Fig. 3.6), and thus depends on $\boldsymbol{r}_0$, $\hat{\boldsymbol{p}}$, and v. For example, if $\boldsymbol{r}_0 = R\hat{\boldsymbol{y}}$ and $\hat{\boldsymbol{p}} = \hat{\boldsymbol{x}}$, then $a = p_F v R^2(s^2 - R^2)/(s^2 + R^2)^2 - p_F v$ and thus $\epsilon_3 = \Delta - 7p_F v/8$ (attained at $s = \sqrt{3}R$). The condition $\epsilon_3 \leq 0$ is satisfied if $v \geq 8v_L/7$, and thus the critical velocity for the trajectory with $\boldsymbol{r}_0 = R\hat{\boldsymbol{y}}$ and $\hat{\boldsymbol{p}} = \hat{\boldsymbol{x}}$ is $8v_L/7$. Similarly, one can calculate the critical velocity for every trajectory, and the critical velocity v_c for the cylinder is the smallest of these. We find (numerically) that $v_c \approx 1.12 v_L$.

We have therefore seen that the Landau velocity is the critical velocity for a microscopic cylinder with radius $R \ll \xi_0$, but it is completely possible that the critical velocity is larger than v_L for a macroscopic cylinder with radius $R \gg \xi_0$.

3.3 Theory

In this section, we introduce the equations which determine the distribution functions ϕ_{Bi}, the quasiparticle potentials u and a, the gap $|\Delta|$, the superfluid velocity $\boldsymbol{v}_s$, and the force $\boldsymbol{F}$ exerted on an object moving in the superfluid; see Refs. [20, 63, 76] for details. We apply these equations to the B phase at zero temperature, and discuss the approximations we use in the studies of the moving cylinder.

3.3.1 Equations

In the semiconductor picture, states are occupied according to the distribution functions $\phi_{B1}(\hat{\boldsymbol{p}},\epsilon,\boldsymbol{r},t)$ and $\phi_{B2}(\hat{\boldsymbol{p}},\epsilon,\boldsymbol{r},t)$. In order to keep the notation simpler, we do not show the dependence on $\boldsymbol{r}$ and t explicitly. Due to the double representation of the physical states, the distribution functions obey the relation $\phi_{B2}(\hat{\boldsymbol{p}},\epsilon) = -\phi_{B1}(-\hat{\boldsymbol{p}},-\epsilon)$. The physically relevant region for the distribution functions is $|\epsilon - a(\hat{\boldsymbol{p}})| \geq |\Delta(\hat{\boldsymbol{p}})|$. Since the two branches coincide if $|\epsilon - a| = |\Delta|$, the distribution functions obey the boundary condition $\phi_{B1}\boldsymbol{(}\hat{\boldsymbol{p}}, a(\hat{\boldsymbol{p}}) \pm |\Delta(\hat{\boldsymbol{p}})|\boldsymbol{)} = \phi_{B2}\boldsymbol{(}\hat{\boldsymbol{p}}, a(\hat{\boldsymbol{p}}) \pm |\Delta(\hat{\boldsymbol{p}})|\boldsymbol{)}$. This condition also takes into account Andreev reflections. The quasiparticle distribution functions n_{Bi} are related to ϕ_{Bi} by $n_{Bi} = \phi_{Bi} + 1/2$. If the magnetic degrees of freedom are taken into account, one needs two additional vector distribution functions $\boldsymbol{\phi}_{B1}(\hat{\boldsymbol{p}},\epsilon)$ and $\boldsymbol{\phi}_{B2}(\hat{\boldsymbol{p}},\epsilon)$. The equilibrium distributions at temperature T are $\phi_{Bi} = -\tanh(\epsilon/2k_BT)/2$. At zero temperature, these reduce to $\phi_{Bi} = 1/2 - \theta(\epsilon)$, where $\theta(x)$ is the unit step function. If we make a Galilei transformation to a moving frame with velocity $\boldsymbol{v}$, $v \ll v_F$, the distribution functions transform as $\phi_{Bi}(\hat{\boldsymbol{p}},\epsilon) \rightarrow \phi_{Bi}(\hat{\boldsymbol{p}},\epsilon + p_F\hat{\boldsymbol{p}}\cdot\boldsymbol{v})$. The density of states, in units of the normal state density of states $2N(0) = m^*p_F/\pi^2\hbar^3$, is given by [20]

$$N(\hat{\boldsymbol{p}},\epsilon) = \nu(\hat{\boldsymbol{p}},\epsilon)\Theta(\hat{\boldsymbol{p}},\epsilon), \tag{3.12}$$

where we have defined

$$\Theta(\hat{\boldsymbol{p}},\epsilon) = \theta([\epsilon - a(\hat{\boldsymbol{p}})]^2 - |\Delta(\hat{\boldsymbol{p}})|^2), \tag{3.13}$$

$$\nu(\hat{\boldsymbol{p}},\epsilon) = \frac{|\epsilon - a(\hat{\boldsymbol{p}})|}{\sqrt{[\epsilon - a(\hat{\boldsymbol{p}})]^2 - |\Delta(\hat{\boldsymbol{p}})|^2}}. \tag{3.14}$$

The distribution functions obey the Boltzmann-like transport equations [20]

$$\frac{\partial\phi_{B1}}{\partial t} + \left(\nu^{-1}\frac{\partial u}{\partial t} + \frac{\partial a}{\partial t} + \frac{|\Delta|}{\epsilon - a}\frac{\partial|\Delta|}{\partial t}\right)\frac{\partial\phi_{B1}}{\partial\epsilon} + \nu^{-1}v_F\hat{\boldsymbol{p}}\cdot\boldsymbol{\nabla}\phi_{B1} = I_{B1}, \tag{3.15}$$

$$\frac{\partial\phi_{B2}}{\partial t} - \left(\nu^{-1}\frac{\partial u}{\partial t} - \frac{\partial a}{\partial t} - \frac{|\Delta|}{\epsilon - a}\frac{\partial|\Delta|}{\partial t}\right)\frac{\partial\phi_{B2}}{\partial\epsilon} - \nu^{-1}v_F\hat{\boldsymbol{p}}\cdot\boldsymbol{\nabla}\phi_{B2} = I_{B2}. \tag{3.16}$$

Here, $I_{Bi} = I_{Bi}(\phi_{B1},\phi_{B2})$ are the collision integrals, the definitions of which can be found in Ref. [20]. The quasiparticle potentials u and a are symmetric and antisymmetric, respectively, in $\hat{\boldsymbol{p}}$, that is, $u(-\hat{\boldsymbol{p}}) = u(\hat{\boldsymbol{p}})$ and $a(-\hat{\boldsymbol{p}}) = -a(\hat{\boldsymbol{p}})$. The energy gap $|\Delta|$ is symmetric in $\hat{\boldsymbol{p}}$, that is, $|\Delta(-\hat{\boldsymbol{p}})| = |\Delta(\hat{\boldsymbol{p}})|$. It is related to the order parameter A through [20]

$$|\Delta(\hat{\boldsymbol{p}})|^2 = \hat{\boldsymbol{p}}\cdot\mathsf{A}^\dagger\mathsf{A}\cdot\hat{\boldsymbol{p}}. \tag{3.17}$$

The quasiparticle potentials u and a, and the order parameter A, obey the self-consistency equations [20]

$$
\begin{aligned}
u(\hat{\boldsymbol{p}}) &= \frac{U}{1+F_0^s} \\
&\quad + \frac{1}{2}\int \frac{d\Omega_p'}{4\pi} A^s(\hat{\boldsymbol{p}}\cdot\hat{\boldsymbol{p}}') \int_{-E_c}^{E_c} d\epsilon \Theta(\hat{\boldsymbol{p}}',\epsilon)[\phi_{B1}(\hat{\boldsymbol{p}}',\epsilon) - \phi_{B2}(\hat{\boldsymbol{p}}',\epsilon)], \qquad (3.18)\\
a(\hat{\boldsymbol{p}}) &= -v_F \boldsymbol{A}\cdot\hat{\boldsymbol{p}} \\
&\quad + \frac{1}{2}\int \frac{d\Omega_p'}{4\pi} A^s(\hat{\boldsymbol{p}}\cdot\hat{\boldsymbol{p}}') \int_{-E_c}^{E_c} d\epsilon N(\hat{\boldsymbol{p}}',\epsilon)[\phi_{B1}(\hat{\boldsymbol{p}}',\epsilon) + \phi_{B2}(\hat{\boldsymbol{p}}',\epsilon)], \qquad (3.19)\\
\mathsf{A} &= -\frac{3}{2}V_1 \mathsf{A}\cdot \int \frac{d\Omega_p'}{4\pi}\hat{\boldsymbol{p}}'\hat{\boldsymbol{p}}' \int_{-E_c}^{E_c} d\epsilon \frac{N(\hat{\boldsymbol{p}}',\epsilon)}{\epsilon - a(\hat{\boldsymbol{p}}')}[\phi_{B1}(\hat{\boldsymbol{p}}',\epsilon) + \phi_{B2}(\hat{\boldsymbol{p}}',\epsilon)]. \qquad (3.20)
\end{aligned}
$$

Here, E_c is the weak-coupling cut-off energy satisfying $|a| + |\Delta| \ll E_c \ll \epsilon_F$. The parameter V_1 describes the strength of the effective attractive interaction between Landau quasiparticles. The scalar and vector potentials U and $\boldsymbol{A}$ are given by

$$U = U_{\text{ext}} + \frac{\hbar}{2}\dot{\psi}, \qquad (3.21)$$

$$\boldsymbol{A} = \boldsymbol{A}_{\text{ext}} - \frac{\hbar}{2}\boldsymbol{\nabla}\psi, \qquad (3.22)$$

where U_{ext} and $\boldsymbol{A}_{\text{ext}}$ are the external potentials, and ψ is the phase, related to the superfluid velocity via

$$\boldsymbol{v}_s = \frac{\hbar}{2m}\boldsymbol{\nabla}\psi. \qquad (3.23)$$

The coefficient A^s is defined by

$$A^s(\hat{\boldsymbol{p}}\cdot\hat{\boldsymbol{p}}') = \sum_{l=0}^{\infty} \frac{F_l^s}{1+F_l^s/(2l+1)} P_l(\hat{\boldsymbol{p}}\cdot\hat{\boldsymbol{p}}'), \qquad (3.24)$$

where $P_l(x)$ are Legendre polynomials and F_l^s are symmetric Fermi liquid parameters. Finally, $\int d\Omega_p'$ denotes integration over the unit sphere of directions $\hat{\boldsymbol{p}}'$.

The phase ψ is also a dynamical variable, and so we need an additional equation to determine its motion. This is the continuity equation [20]

$$\dot{\rho} + \boldsymbol{\nabla}\cdot\boldsymbol{j} = 0, \qquad (3.25)$$

where ρ is the mass density,

$$
\begin{aligned}
\rho &= \frac{mp_F^3}{3\pi^2\hbar^3} - \frac{2mN(0)}{1+F_0^s}U \\
&\quad + \frac{mN(0)}{1+F_0^s}\int \frac{d\Omega_p}{4\pi}\int_{-E_c}^{E_c} d\epsilon \Theta(\hat{\boldsymbol{p}},\epsilon)[\phi_{B1}(\hat{\boldsymbol{p}},\epsilon) - \phi_{B2}(\hat{\boldsymbol{p}},\epsilon)],
\end{aligned}
\qquad (3.26)
$$

and $\boldsymbol{j}$ is the mass current density,

$$\boldsymbol{j} = mv_F N(0) \int \frac{d\Omega_p}{4\pi} \hat{\boldsymbol{p}} \int_{-E_c}^{E_c} d\epsilon N(\hat{\boldsymbol{p}}, \epsilon)[\phi_{B1}(\hat{\boldsymbol{p}}, \epsilon) + \phi_{B2}(\hat{\boldsymbol{p}}, \epsilon)]. \tag{3.27}$$

Once the distribution functions, the quasiparticle potentials, and the order parameter are known, one can calculate the stress tensor $\overset{\leftrightarrow}{\mathbf{\Pi}}$ [76],

$$\overset{\leftrightarrow}{\mathbf{\Pi}} = v_F p_F N(0) \int \frac{d\Omega_p}{4\pi} \hat{\boldsymbol{p}}\hat{\boldsymbol{p}} \int_{-E_c}^{E_c} d\epsilon \Theta(\hat{\boldsymbol{p}}, \epsilon)[\phi_{B1}(\hat{\boldsymbol{p}}, \epsilon) - \phi_{B2}(\hat{\boldsymbol{p}}, \epsilon)]. \tag{3.28}$$

The force exerted on a surface A is given by the surface integral

$$\boldsymbol{F} = \int_A d\boldsymbol{A} \cdot \overset{\leftrightarrow}{\mathbf{\Pi}}. \tag{3.29}$$

3.3.2 Application to the B phase

Let us apply the theory to the B phase at zero temperature. The order parameter of the B phase is given by Eq. (2.1). Consequently, Eq. (3.17) implies that $|\Delta(\hat{\boldsymbol{p}})| = \Delta_B$. We study steady state, and assume that there are no external potentials present. Equations (3.21), (3.22), and (3.23) show that $U = 0$ and $\boldsymbol{A} = -m\boldsymbol{v}_s$.

If the fluid is at rest and in thermal equilibrium, then $\boldsymbol{v}_s = \mathbf{0}$ and $\phi_{Bi} = 1/2 - \theta(\epsilon)$. The transport equations (3.15) and (3.16) are automatically satisfied, since the distribution functions are of the local equilibrium form, and therefore the collision integrals vanish [20]. The self-consistency equations (3.18), (3.19), and (3.20) are solved by $u = a = 0$, provided that Δ_B satisfies the familiar zero-temperature, weak-coupling gap equation [1]

$$V_1^{-1} = -\log\left(\frac{\Delta_B}{2E_c}\right). \tag{3.30}$$

Using these, Eqs. (3.26) and (3.27) imply that $\rho = mp_F^3/3\pi^2\hbar^3$ and $\boldsymbol{j} = \mathbf{0}$, and so the continuity equation (3.25) is satisfied. Equation (3.28) shows that the stress tensor vanishes, $\overset{\leftrightarrow}{\mathbf{\Pi}} = \overset{\leftrightarrow}{\mathbf{0}}$.

If this same fluid is observed from a frame of reference moving at velocity $\boldsymbol{v}$ with respect to the fluid, then $\boldsymbol{v}_s = -\boldsymbol{v}$ and $\phi_{Bi} = 1/2 - \theta(\epsilon + p_F \hat{\boldsymbol{p}} \cdot \boldsymbol{v})$. The transport equations are again automatically satisfied, and the self-consistency equations are solved by $u = 0$ and $a = -p_F \boldsymbol{v} \cdot \hat{\boldsymbol{p}}$, provided that Δ_B satisfies the gap equation (3.30). The mass density, the mass current density, and the stress tensor are given by $\rho = mp_F^3/3\pi^2\hbar^3$, $\boldsymbol{j} = -(2/3)mv_F p_F N(0)\boldsymbol{v}$, and $\overset{\leftrightarrow}{\mathbf{\Pi}} = \overset{\leftrightarrow}{\mathbf{0}}$. The continuity equation is satisfied. Note that by setting $\boldsymbol{v} = \mathbf{0}$, we obtain the same results as above.

If, on the other hand, the fluid is in thermal equilibrium in the moving frame, then $\boldsymbol{v}_s = -\boldsymbol{v}$ and $\phi_{Bi} = 1/2 - \theta(\epsilon)$. Everything is identical to the previous situation provided the velocity is less than the Landau velocity v_L. At higher velocities, Eqs. (3.18), (3.19), and (3.20) have no self-consistent solution if we assume that the order parameter is of the B phase form (2.1). In this case, the order parameter is modified so that the gap is suppressed along the flow. Details can be found in Refs. [22, 23].

Finally, ideal fluid is fluid where there are no quasiparticles present. This can be modelled by setting $\phi_{Bi} = 1/2 - \theta(\epsilon - a)$, since this implies $n_{Bi} = 0$ for $\epsilon \geq a + \Delta_B$. The transport equations (3.15) and (3.16) are automatically satisfied. The self-consistency equations (3.18), (3.19), and (3.20) are solved by $u = 0$ and $a = p_F \boldsymbol{v}_s \cdot \hat{\boldsymbol{p}}$ if Δ_B satisfies the gap equation (3.30). The mass density and the mass current density are given by $\rho = mp_F^3/3\pi^2\hbar^3$ and $\boldsymbol{j} = (2/3)mv_Fp_FN(0)\boldsymbol{v}_s$, and so the continuity equation (3.25) is satisfied if $\boldsymbol{\nabla} \cdot \boldsymbol{v}_s = 0$, or

$$\nabla^2\psi = 0. \tag{3.31}$$

The stress tensor vanishes.

3.3.3 Approximations

Solving Eqs. (3.15), (3.16), (3.18), (3.19), (3.20), and (3.25) in the case of the macroscopic cylinder is necessarily a numerical task. In order to reduce the complexity of the problem, we make several assumptions. First of all, we study static flow (in the object frame) at zero temperature. We assume that there are no external potentials, and that the only non-vanishing symmetric Landau parameters are F_0^s and F_1^s. Finally, we assume that there are no collisions between quasiparticles, $I_{Bi} = 0$, and that the magnitude of the energy gap is constant, $|\Delta(\hat{\boldsymbol{p}}, \boldsymbol{r})| = \Delta$. We return to the effect of collisions briefly in Sec. 3.7, where we study whether it is possible that quasiparticle collisions could lead to a situation in which the quasiparticle states in the near region are in thermal equilibrium in the object frame.

Assuming static flow and no collisions between quasiparticles, the transport equations (3.15) and (3.16) reduce to

$$\hat{\boldsymbol{p}} \cdot \boldsymbol{\nabla}\phi_{Bi} = 0. \tag{3.32}$$

Thus, at fixed ϵ and $\hat{\boldsymbol{p}}$, the distribution functions ϕ_{Bi} are piecewise constant along straight-line trajectories $\boldsymbol{r} = \boldsymbol{r}_0 + s\hat{\boldsymbol{p}}$, $s \in \mathbb{R}$. The reason they are piecewise constant, not simply constant, is that there might be some regions along the trajectory where $|\epsilon - a| < |\Delta|$. This is an unphysical region in which ϕ_{Bi} are not well-defined. In Fig. 3.6, this happens at energies just below ϵ_3, where part of the trajectory is in region L, part of the trajectory is in region N, and there is a forbidden region between the two.

Since only F_0^s and F_1^s are non-zero, Eqs. (3.18) and (3.19) imply that the quasiparticle potentials can be written as $u(\hat{\boldsymbol{p}}, \boldsymbol{r}) = u(\boldsymbol{r})$ and $a(\hat{\boldsymbol{p}}, \boldsymbol{r}) = \boldsymbol{\alpha}(\boldsymbol{r}) \cdot \hat{\boldsymbol{p}}$, with

$$u = \frac{1}{2}\frac{F_0^s}{1+F_0^s}\int \frac{d\Omega_p}{4\pi}\int_{-E_c}^{E_c} d\epsilon\Theta(\hat{\boldsymbol{p}},\epsilon)[\phi_{B1}(\hat{\boldsymbol{p}},\epsilon)-\phi_{B2}(\hat{\boldsymbol{p}},\epsilon)], \tag{3.33}$$

$$\boldsymbol{\alpha} = mv_F\boldsymbol{v}_s + \frac{1}{2}\frac{F_1^s}{1+F_1^s/3}\int \frac{d\Omega_p}{4\pi}\hat{\boldsymbol{p}}\int_{-E_c}^{E_c} d\epsilon N(\hat{\boldsymbol{p}},\epsilon)[\phi_{B1}(\hat{\boldsymbol{p}},\epsilon)+\phi_{B2}(\hat{\boldsymbol{p}},\epsilon)]. \tag{3.34}$$

Equation (3.33) is no longer a self-consistency equation, since the right-hand side is independent of u due to the simpler form of the transport equation (3.32). It is therefore not needed for solving the flow field. It is convenient to express Eq. (3.34) in terms of n_{Bi}. Substituting $\phi_{Bi} = n_{Bi} - 1/2$ and simplifying, we obtain

$$\boldsymbol{\alpha} = p_F\boldsymbol{v}_s + F_1^s\boldsymbol{I}, \tag{3.35}$$

where

$$\boldsymbol{I} = \int \frac{d\Omega_p}{4\pi}\hat{\boldsymbol{p}}\int_{a(\hat{\boldsymbol{p}})+\Delta}^{E_c} d\epsilon N(\hat{\boldsymbol{p}},\epsilon)[n_{B1}(\hat{\boldsymbol{p}},\epsilon)+n_{B2}(\hat{\boldsymbol{p}},\epsilon)]. \tag{3.36}$$

If there are no quasiparticles present, then $n_{Bi} = 0$, and hence $\boldsymbol{I} = \boldsymbol{0}$. The vector field $\boldsymbol{\alpha}$ can be interpreted as the effective velocity field influencing the quasiparticles.

For static flow, the continuity equation (3.25) reduces to

$$\boldsymbol{\nabla}\cdot\boldsymbol{j} = 0. \tag{3.37}$$

We can express the mass current density (3.27) in terms of $\boldsymbol{I}$ as

$$\boldsymbol{j} = \frac{2}{3}mv_F N(0)(\boldsymbol{\alpha}+3\boldsymbol{I}). \tag{3.38}$$

Thus, mass is carried by both the condensate ($\boldsymbol{\alpha}$) and by quasiparticles ($3\boldsymbol{I}$).

3.4 Mesoscopic boundary condition

To study an object moving in superfluid ^{3}He, we need a boundary condition to describe the effect of the object on the distribution functions ϕ_{Bi}. A detailed model would study the surface layer (or the similar region around a microscopic cylinder), but this can lead to complicated analysis. The complications generally arise from the fact that a quasiparticle scattered from the surface of the object is not necessarily able to escape the surface layer, but can instead be Andreev reflected back to the surface from the surface layer. This process can occur multiple times in succession. Some examples of such calculations can be found in Refs. [63, 77, 78, 79, 80, 81].

We are not interested in the details of the complex processes occurring in the surface layer. Instead, we would like to formulate a boundary condition that captures the essential features as seen outside the surface layer, that is, at mesoscopic scale. In this section, we introduce a simple mesoscopic boundary condition that describes diffuse, elastic scattering of quasiparticles from the surface, satisfies conservation of mass and excitation number [76], and takes into account pair breaking at velocities above the Landau velocity (or, more accurately, when $\alpha > \Delta$).

3.4.1 Planar wall

Let us first formulate the boundary condition for a piece of planar wall with unit normal $\hat{\boldsymbol{n}}$. This could, for example, be a portion of the surface of a macroscopic cylinder. We work in the rest frame of the wall, and use the excitation picture. The boundary condition should express the distribution functions ϕ_{Bi} of excitations leaving the the surface layer (scattered excitations, $\hat{\boldsymbol{n}} \cdot \hat{\boldsymbol{p}} > 0$ for excitations of type $B1$ and $\hat{\boldsymbol{n}} \cdot \hat{\boldsymbol{p}} < 0$ for excitations of type $B2$) in terms of the distribution functions of excitations entering the surface layer (incident excitations, $\hat{\boldsymbol{n}} \cdot \hat{\boldsymbol{p}} < 0$ for excitations of type $B1$ and $\hat{\boldsymbol{n}} \cdot \hat{\boldsymbol{p}} > 0$ for excitations of type $B2$).

What properties should the boundary condition satisfy? Conservation of mass [Eq. (3.37)] tells us that no mass should flow through the wall. Conservation of excitation number [76] states that no excitations should flow through the wall. If a quasiparticle with energy ϵ hits the wall, it should scatter out as a quasiparticle with equal energy, but with random direction and possibly a different branch. Finally, once the velocity of the wall with respect to the fluid reaches the Landau velocity (or, more accurately, when the magnitude of $\boldsymbol{\alpha}$ reaches Δ), the wall should start to break Cooper pairs. It turns out that these conditions are satisfied if

$$\hat{\boldsymbol{n}} \cdot \boldsymbol{j}(\epsilon) = 0, \tag{3.39}$$
$$\hat{\boldsymbol{n}} \cdot \boldsymbol{j}_e(\epsilon) = 0. \tag{3.40}$$

Here, $\boldsymbol{j}(\epsilon)$ and $\boldsymbol{j}_e(\epsilon)$ are the mass current density per unit energy and the excitation number current density per unit energy, respectively. They are defined as [76]

$$\boldsymbol{j}(\epsilon) = m v_F N(0) \int \frac{d\Omega_p}{4\pi} \hat{\boldsymbol{p}} N(\hat{\boldsymbol{p}}, \epsilon)[\phi_{B1}(\hat{\boldsymbol{p}}, \epsilon) + \phi_{B2}(\hat{\boldsymbol{p}}, \epsilon)], \tag{3.41}$$
$$\boldsymbol{j}_e(\epsilon) = v_F N(0) \int \frac{d\Omega_p}{4\pi} \hat{\boldsymbol{p}} \Theta(\hat{\boldsymbol{p}}, \epsilon)[\phi_{B1}(\hat{\boldsymbol{p}}, \epsilon) - \phi_{B2}(\hat{\boldsymbol{p}}, \epsilon)]. \tag{3.42}$$

Note that by integrating $\boldsymbol{j}(\epsilon)$ over energy from $-E_c$ to E_c, one obtains the mass current density (3.27). The energy integral of $\boldsymbol{j}_e(\epsilon)$, on the other hand, vanishes identically due to the identity $\phi_{B2}(\hat{\boldsymbol{p}}, \epsilon) = -\phi_{B1}(-\hat{\boldsymbol{p}}, -\epsilon)$. This shows that the excitation number current density $\boldsymbol{j}_e$ defined in Eq. (12) of Pub. II is, in fact, identically zero. This does not, however, affect any results of Pub. II, since we only used $\boldsymbol{j}_e(\epsilon)$, not $\boldsymbol{j}_e$, in formulating the boundary condition.

Equations (3.39) and (3.40) do not uniquely fix the form of the scattered distributions, and so there are different possibilities for the boundary condition. We propose a one where the scattered distributions are given by

$$\phi_{B1}(\hat{\boldsymbol{p}}, \hat{\boldsymbol{n}} \cdot \hat{\boldsymbol{p}} > 0, \epsilon) = \phi_{B1}^{bc}(\hat{\boldsymbol{p}}, \epsilon) = \frac{g(\epsilon)}{2} \left[\nu^{-1}(\hat{\boldsymbol{p}}, \epsilon) A(\epsilon) + B(\epsilon)\right], \tag{3.43}$$
$$\phi_{B2}(\hat{\boldsymbol{p}}, \hat{\boldsymbol{n}} \cdot \hat{\boldsymbol{p}} < 0, \epsilon) = \phi_{B2}^{bc}(\hat{\boldsymbol{p}}, \epsilon) = \frac{g(\epsilon)}{2} \left[-\nu^{-1}(\hat{\boldsymbol{p}}, \epsilon) A(\epsilon) + B(\epsilon)\right]. \tag{3.44}$$

Here, the coefficients A and B are determined by the incident distributions,

$$A(\epsilon) = \int_{\hat{\boldsymbol{n}}\cdot\hat{\boldsymbol{p}}<0} d\Omega_p |\hat{\boldsymbol{n}}\cdot\hat{\boldsymbol{p}}| N(\hat{\boldsymbol{p}},\epsilon)\phi_{B1}(\hat{\boldsymbol{p}},\epsilon) - \int_{\hat{\boldsymbol{n}}\cdot\hat{\boldsymbol{p}}>0} d\Omega_p |\hat{\boldsymbol{n}}\cdot\hat{\boldsymbol{p}}| N(\hat{\boldsymbol{p}},\epsilon)\phi_{B2}(\hat{\boldsymbol{p}},\epsilon), \tag{3.45}$$

$$B(\epsilon) = \int_{\hat{\boldsymbol{n}}\cdot\hat{\boldsymbol{p}}<0} d\Omega_p |\hat{\boldsymbol{n}}\cdot\hat{\boldsymbol{p}}| \Theta(\hat{\boldsymbol{p}},\epsilon)\phi_{B1}(\hat{\boldsymbol{p}},\epsilon) + \int_{\hat{\boldsymbol{n}}\cdot\hat{\boldsymbol{p}}>0} d\Omega_p |\hat{\boldsymbol{n}}\cdot\hat{\boldsymbol{p}}| \Theta(\hat{\boldsymbol{p}},\epsilon)\phi_{B2}(\hat{\boldsymbol{p}},\epsilon), \tag{3.46}$$

and g is a normalisation factor,

$$g^{-1}(\epsilon) = \int_{\hat{\boldsymbol{n}}\cdot\hat{\boldsymbol{p}}>0} d\Omega_p \hat{\boldsymbol{n}}\cdot\hat{\boldsymbol{p}}\, \Theta(\hat{\boldsymbol{p}},\epsilon). \tag{3.47}$$

Equations (3.39) and (3.40) are satisfied if $\hat{\boldsymbol{n}}\cdot\boldsymbol{\alpha} = 0$ and $|\Delta(\underline{\hat{\boldsymbol{p}}})| = |\Delta(\hat{\boldsymbol{p}})|$, where $\underline{\hat{\boldsymbol{p}}} = \hat{\boldsymbol{p}} - 2\hat{\boldsymbol{n}}(\hat{\boldsymbol{n}}\cdot\hat{\boldsymbol{p}})$ is the direction of specular reflection (see App. B for details). The former condition simply means that there is no superflow through the wall, as can be seen from Eqs. (3.35) and (3.38). The latter condition restricts the possible form of the order parameter on the surface, but not too drastically.

Let us study some of the properties of the boundary condition. The incident distributions enter Eqs. (3.43) and (3.44) only through A and B, where they are integrated over $\hat{\boldsymbol{p}}$. This implies diffuse reflection. There can be branch conversion from $B1$ to $B2$ and vice versa. Since the scattered distributions at fixed energy ϵ depend on the incident distributions at equal energy, the boundary condition describes elastic scattering of quasiparticles. Conservation of mass and excitation number are satisfied, since Eqs. (3.39) and (3.40) hold by construction (see App. B for details). Consider a situation in which there are no incident quasiparticles hitting the wall. This can be modelled with distribution functions $\phi_{Bi} = 1/2 - \theta(\epsilon - a)$, since these imply $n_{Bi} = 0$ if $\epsilon \geq a + \Delta$. Substituting the distributions into Eqs. (3.45) and (3.46) yields

$$A(\epsilon) = 0, \tag{3.48}$$

$$B(\epsilon) = 2\int_{\hat{\boldsymbol{n}}\cdot\hat{\boldsymbol{p}}>0} d\Omega_p |\hat{\boldsymbol{n}}\cdot\hat{\boldsymbol{p}}| \Theta(\hat{\boldsymbol{p}},\epsilon)\left[\frac{1}{2} - \theta(\epsilon - \boldsymbol{\alpha}\cdot\hat{\boldsymbol{p}})\right]. \tag{3.49}$$

Since $A = 0$, we find that the scattered distributions (3.43) and (3.44) are equal and depend only on energy, $\phi^{bc}_{B1}(\hat{\boldsymbol{p}},\epsilon) = \phi^{bc}_{B2}(\hat{\boldsymbol{p}},\epsilon) = \phi^{bc}_{Bi}(\epsilon) = g(\epsilon)B(\epsilon)/2$. It is easy to see that if $\alpha \leq \Delta$, then $\phi^{bc}_{Bi} = 1/2 - \theta(\epsilon)$, and there are no quasiparticles created by the wall. If $\alpha > \Delta$, Cooper pairs start to break. Quasiparticles are created at energies $\Delta - \alpha \leq \epsilon \leq \alpha - \Delta$, just as we expect. Figure 3.7 shows the scattered distributions ϕ^{bc}_{Bi} as a function of energy at different values of α.

3.4.2 Microscopic cylinder

In the case of a microscopic cylinder ($R \ll \xi_0$), we have to modify the boundary condition slightly due to the small size of the cylinder, just like in the case of the

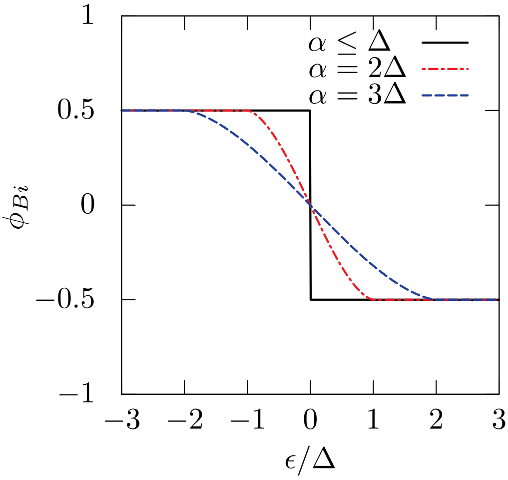

Figure 3.7: The scattered distribution functions $\phi^{bc}_{B1}(\hat{\boldsymbol{p}}, \epsilon) = \phi^{bc}_{B2}(\hat{\boldsymbol{p}}, \epsilon) = \phi^{bc}_{Bi}(\epsilon) = g(\epsilon)B(\epsilon)/2$ for a planar wall as a function of energy, assuming there are no incident quasiparticles. The distributions are determined by the mesoscopic boundary condition, Eqs. (3.43) and (3.44)

small object in Pub. II. Instead of requiring $\hat{\boldsymbol{n}} \cdot \boldsymbol{j}(\epsilon) = \hat{\boldsymbol{n}} \cdot \boldsymbol{j}_e(\epsilon) = 0$ at each point on the surface of the cylinder, we again require that the conservation laws of mass and excitation number are satisfied at mesoscopic scale. This can be enforced by requiring that there is no net flow of mass or excitations through a cylindrical surface of radius $\lambda \sim \xi_0 \gg R$ around the cylinder. Working in the object frame, this means that

$$\int_{r=\lambda} dA \hat{\boldsymbol{r}} \cdot \boldsymbol{j}(\epsilon) = 0, \tag{3.50}$$

$$\int_{r=\lambda} dA \hat{\boldsymbol{r}} \cdot \boldsymbol{j}_e(\epsilon) = 0, \tag{3.51}$$

where the integrals are over the surface $r = \lambda$. Since we assume that the system is translationally invariant in the z direction, the integration over z produces a constant, and thus Eqs. (3.50) and (3.51) reduce to

$$\int_{r=\lambda} ds \hat{\boldsymbol{r}} \cdot \boldsymbol{j}(\epsilon) = 0, \tag{3.52}$$

$$\int_{r=\lambda} ds \hat{\boldsymbol{r}} \cdot \boldsymbol{j}_e(\epsilon) = 0, \tag{3.53}$$

where the integration is over the circumference of a circle of radius λ. Although λ is very large compared to R, it is still small compared to the length scale at which we expect $\boldsymbol{\alpha}$ and A to vary. We therefore assume that $\boldsymbol{\alpha}$ and A are constants on the circle $r = \lambda$.

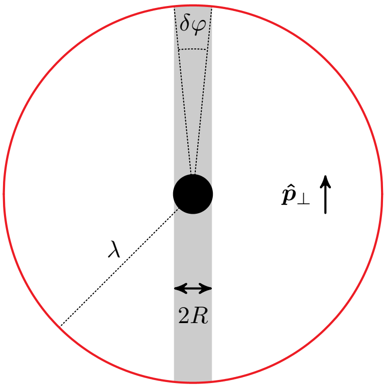

Figure 3.8: The two arcs of the circle $r = \lambda$ under the shaded region indicate the points where excitations with a fixed direction $\hat{\boldsymbol{p}}_\perp$ travel either towards or away from a disk of radius $R \ll \lambda$. The angle $\delta\varphi = 2\arcsin(R/\lambda)$ denotes the angular diameter of the arcs as seen from the centre of the circle.

The boundary condition should again express the distribution functions of the excitations created by the cylinder in terms of the incident distributions, but this time on the surface $r = \lambda$. Consider a fixed direction $\hat{\boldsymbol{p}} = p_{\|}\hat{\boldsymbol{z}} + \boldsymbol{p}_\perp$, where $\boldsymbol{p}_\perp \cdot \hat{\boldsymbol{z}} = 0$ and $p_{\|}^2 + p_\perp^2 = 1$. The only points on the circle $r = \lambda$ where $\hat{\boldsymbol{p}}$ can be a direction of either a scattered or an incident excitation are shown under the shaded region in Fig. 3.8. In the limit $R/\lambda \to 0$, the region reduces to two points, $\boldsymbol{r} = \pm\lambda\hat{\boldsymbol{p}}_\perp$. We propose a boundary condition

$$\phi_{B1}(\hat{\boldsymbol{p}}, \epsilon, \lambda\hat{\boldsymbol{p}}_\perp) = \phi_{B1}^{bc}(\hat{\boldsymbol{p}}, \epsilon) = \frac{g(\epsilon)}{2}\left[\nu^{-1}(\hat{\boldsymbol{p}}, \epsilon)A(\epsilon) + B(\epsilon)\right], \tag{3.54}$$

$$\phi_{B2}(\hat{\boldsymbol{p}}, \epsilon, -\lambda\hat{\boldsymbol{p}}_\perp) = \phi_{B2}^{bc}(\hat{\boldsymbol{p}}, \epsilon) = \frac{g(\epsilon)}{2}\left[-\nu^{-1}(\hat{\boldsymbol{p}}, \epsilon)A(\epsilon) + B(\epsilon)\right], \tag{3.55}$$

where

$$A(\epsilon) = \int d\Omega_p p_\perp N(\hat{\boldsymbol{p}}, \epsilon)\left[\phi_{B1}(\hat{\boldsymbol{p}}, \epsilon, -\lambda\hat{\boldsymbol{p}}_\perp) - \phi_{B2}(\hat{\boldsymbol{p}}, \epsilon, \lambda\hat{\boldsymbol{p}}_\perp)\right], \tag{3.56}$$

$$B(\epsilon) = \int d\Omega_p p_\perp \Theta(\hat{\boldsymbol{p}}, \epsilon)\left[\phi_{B1}(\hat{\boldsymbol{p}}, \epsilon, -\lambda\hat{\boldsymbol{p}}_\perp) + \phi_{B2}(\hat{\boldsymbol{p}}, \epsilon, \lambda\hat{\boldsymbol{p}}_\perp)\right], \tag{3.57}$$

$$g^{-1}(\epsilon) = \int d\Omega_p p_\perp \Theta(\hat{\boldsymbol{p}}, \epsilon), \tag{3.58}$$

and

$$\boldsymbol{p}_\perp = \hat{\boldsymbol{p}} - \hat{\boldsymbol{z}}(\hat{\boldsymbol{z}} \cdot \hat{\boldsymbol{p}}). \tag{3.59}$$

This is a straightforward generalisation of the boundary condition of Sec. 3.4.1, and shares the same properties. More details can be found in App. B.

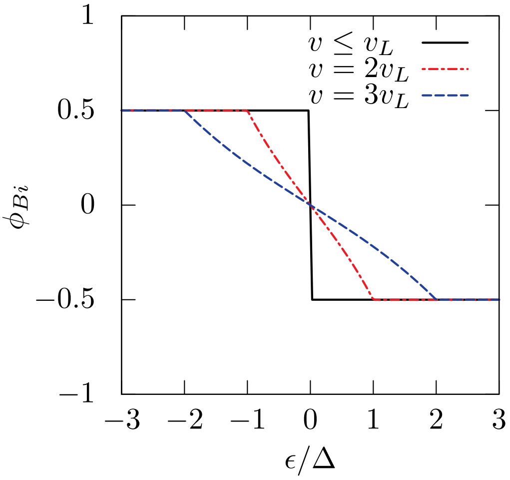

Figure 3.9: The scattered distribution functions $\phi^{bc}_{B1}(\hat{\boldsymbol{p}}, \epsilon) = \phi^{bc}_{B2}(\hat{\boldsymbol{p}}, \epsilon) = \phi^{bc}_{Bi}(\epsilon) = g(\epsilon)B(\epsilon)/2$ for a microscopic cylinder as a function of energy at zero temperature. The distributions are determined by the mesoscopic boundary condition, Eqs. (3.54) and (3.55).

3.5 Force exerted on a microscopic cylinder

Let us apply the mesoscopic boundary condition, Eqs. (3.54) and (3.55), to calculate the force exerted on a microscopic cylinder ($R \ll \xi_0$). Due to its small size, the cylinder does not affect the flow field at mesoscopic scale. Working in the object frame, we have $\boldsymbol{v}_s = -\boldsymbol{v}$ and $\boldsymbol{\alpha} = p_F \boldsymbol{v}_s$. The incident distributions are $\phi_{B1}(\hat{\boldsymbol{p}}, \epsilon, -\lambda\hat{\boldsymbol{p}}_\perp) = \phi_{B2}(\hat{\boldsymbol{p}}, \epsilon, \lambda\hat{\boldsymbol{p}}_\perp) = 1/2 - \theta(\epsilon + p_F \boldsymbol{v} \cdot \hat{\boldsymbol{p}})$. Substituting these into Eqs. (3.56) and (3.57) yields

$$A(\epsilon) = 0, \tag{3.60}$$

$$B(\epsilon) = 2 \int d\Omega_p p_\perp \Theta(\hat{\boldsymbol{p}}, \epsilon) \left[\frac{1}{2} - \theta(\epsilon - \boldsymbol{\alpha} \cdot \hat{\boldsymbol{p}}) \right]. \tag{3.61}$$

Since $A = 0$, the scattered distributions (3.54) and (3.55) are equal and depend only on energy, $\phi^{bc}_{B1}(\hat{\boldsymbol{p}}, \epsilon) = \phi^{bc}_{B2}(\hat{\boldsymbol{p}}, \epsilon) = \phi^{bc}_{Bi}(\epsilon) = g(\epsilon)B(\epsilon)/2$. If $v \leq v_L$, then $\phi^{bc}_{Bi} = 1/2 - \theta(\epsilon)$, and no quasiparticles are created. At higher velocities, Cooper pairs start to break, and quasiparticles are created at energies $\Delta - p_F v \leq \epsilon \leq p_F v - \Delta$, as expected. Figure 3.9 shows the scattered distributions $\phi^{bc}_{Bi}(\epsilon)$ as a function of energy at different values of v.

To calculate the force exerted on the cylinder, we integrate the stress tensor (3.28) over a cylindrical surface of radius $\lambda \sim \xi_0 \gg R$, see App. B for details. The force per unit length is given by

$$\begin{aligned}\boldsymbol{f} \approx 2Rv_F p_F N(0) \int_{-E_c}^{E_c} d\epsilon \int \frac{d\Omega_p}{4\pi} p_\perp \hat{\boldsymbol{p}} \Theta(\hat{\boldsymbol{p}}, \epsilon) \\ \times \Big\{ - [\phi_{B1}(\hat{\boldsymbol{p}}, \epsilon, -\lambda \hat{\boldsymbol{p}}_\perp) + \phi_{B2}(\hat{\boldsymbol{p}}, \epsilon, \lambda \hat{\boldsymbol{p}}_\perp)] \\ + [\phi_{B1}(\hat{\boldsymbol{p}}, \epsilon, \lambda \hat{\boldsymbol{p}}_\perp) + \phi_{B2}(\hat{\boldsymbol{p}}, \epsilon, -\lambda \hat{\boldsymbol{p}}_\perp)] \Big\}.\end{aligned} \tag{3.62}$$

Substituting the distributions and simplifying, we obtain

$$\boldsymbol{f} \approx 4Rv_F p_F N(0) \int_0^{E_c} d\epsilon \int \frac{d\Omega_p}{4\pi} p_\perp \hat{\boldsymbol{p}} \Theta(\hat{\boldsymbol{p}}, \epsilon) \left[g(\epsilon) B(\epsilon) - 1 + 2\theta(\epsilon - \boldsymbol{\alpha} \cdot \hat{\boldsymbol{p}}) \right]. \tag{3.63}$$

We find that $\boldsymbol{f} = \boldsymbol{0}$ if $v \leq v_L$. At higher velocities, the force starts to increase. This shows that the Landau velocity v_L is the critical velocity for a microscopic cylinder. Figure 3.10 shows the force as a function of velocity. The unit of force used in the figure is

$$F_0 = v_F p_F^2 N(0) \sigma v_L, \tag{3.64}$$

where σ is the cross section of the object in the plane perpendicular to $\boldsymbol{v}$ ($\sigma = 2Rl$ for a cylinder of length l). For the sake of comparison, the figure also shows the force exerted on a small ion-like object, which we calculated in Sec. IV of Pub. II. We see that the results are very similar. In both cases, we can calculate analytically the force in the normal state, F_n, by setting $\Delta = 0$. As a result, we obtain

$$F_n = \begin{cases} \frac{3\pi}{16} v_F p_F^2 N(0) \sigma v, & \text{Microscopic cylinder,} \\ \frac{2}{3} v_F p_F^2 N(0) \sigma v, & \text{Ion.} \end{cases} \tag{3.65}$$

An identical result for the ion was also obtained in Ref. [82].

3.6 Force exerted on a macroscopic cylinder

In this section, we study a macroscopic cylinder ($R \gg \xi_0$). We work in the object frame. The flow field is determined by the equations of Sec. 3.3.3. Combining Eqs. (3.35), (3.37), and (3.38), we obtain

$$\boldsymbol{\alpha} = p_F \boldsymbol{v}_s + F_1^s \boldsymbol{I}, \tag{3.66}$$

$$\nabla^2 \psi = -\frac{2m}{\hbar p_F} (3 + F_1^s) \boldsymbol{\nabla} \cdot \boldsymbol{I}, \tag{3.67}$$

$$\boldsymbol{v}_s = \frac{\hbar}{2m} \boldsymbol{\nabla} \psi. \tag{3.68}$$

To calculate $\boldsymbol{I}$, we need the quasiparticle distribution functions $n_{Bi} = \phi_{Bi} + 1/2$. Let us consider a point $\boldsymbol{r}_0$ outside the cylinder, and fix a direction $\hat{\boldsymbol{p}}$. At each

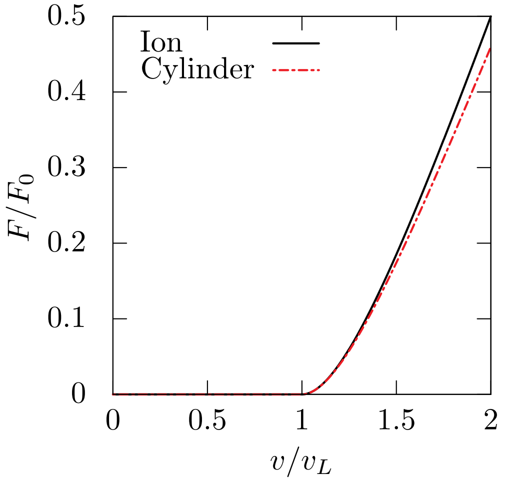

Figure 3.10: The force exerted on a microscopic cylinder and on an ion as a function of velocity.

energy ϵ, the distribution functions are piecewise constants along the straight-line trajectories $\boldsymbol{r} = \boldsymbol{r}_0 + s\hat{\boldsymbol{p}}$, $s \in \mathbb{R}$. This means that the distribution function n_{Bi} at $\boldsymbol{r}_0$ is determined by the origin of quasiparticles along the trajectory. At zero temperature, the only source of quasiparticles is the cylinder. A quasiparticle created by the cylinder can arrive to a point $\boldsymbol{r}_0$ either directly or via Andreev reflection.

As an example, consider a trajectory which intersects the cylinder with $\hat{\boldsymbol{p}}$ pointing away from the cylinder. Figure 3.6 shows a possible variation of $a + \Delta$ along such a trajectory. In region M, the quasiparticles of type $B1$ originate from the cylinder, and thus $n_{B1} = n_{B1}^{bc} = \phi_{B1}^{bc} + 1/2$, where ϕ_{B1}^{bc} is determined by the mesoscopic boundary condition (3.43). The quasiparticles of type $B2$, on the other hand, originate from the far region. Since there are no quasiparticles generated in the far region, $n_{B2} = 0$. In region N, the quasiparticles of type $B2$ originate from the far region, and so $n_{B2} = 0$. The quasiparticles of type $B1$ also originate from the far region, but indirectly. They are initially quasiparticles of type $B2$ which travel towards the cylinder from the far region, but are Andreev reflected before they reach the cylinder. The distribution function n_{B1} at $\boldsymbol{r}_0$ is therefore equal to the distribution function n_{B2} in the far region, that is, $n_{B1} = 0$. In region L, the quasiparticles of type $B1$ originate from the cylinder, and so $n_{B1} = n_{B1}^{bc}$. The quasiparticles of type $B2$ originate from the cylinder indirectly via Andreev reflection, so that $n_{B2} = n_{B1}^{bc}$. Finally, there are states in the region K which are not in contact with either the cylinder or the far region. Instead, they are localised somewhere in the flow field. Their occupation cannot be determined as straightforwardly as the occupation of the states we have consider so far. In fact, the occupation of these states depends on the transient phase, that is, how the steady state has been achieved. We consider two different models. In model 1, the states K are empty with $n_{B1} = n_{B2} = 0$, since after the steady state has been achieved, these states cannot be filled by the cylinder. However, it could be possible that the states K are filled, at least to some degree, as the cylinder is accelerated from rest. This is considered in model 2, where we assume that the states K are in thermal equilibrium in the object frame, $n_{Bi} = 1 - \theta(\epsilon)$.

The same deduction can be used to determine the distribution functions if $\hat{\boldsymbol{p}}$ points towards the cylinder. On trajectories which do not intersect the cylinder, states can only belong to either region N or region K. In region N, there are no quasiparticles, and so $n_{Bi} = 0$. We assume that the same is true for states K, since on acceleration, the cylinder can only fill states K if the trajectory intersects the cylinder.

Substituting the distributions into Eq. (3.36) yields

$$\begin{aligned}\boldsymbol{I} = &\int_{\text{hit}+} \frac{d\Omega_p}{4\pi}\hat{\boldsymbol{p}}\left[\int_{\epsilon_{\max}(\hat{\boldsymbol{p}})}^{E_c} d\epsilon\,\nu(\hat{\boldsymbol{p}},\epsilon)n_{B1}^{bc}(\hat{\boldsymbol{p}},\epsilon) + 2\int_{\epsilon_2(\hat{\boldsymbol{p}})}^{\epsilon_{\max}(\hat{\boldsymbol{p}})} d\epsilon\,\nu(\hat{\boldsymbol{p}},\epsilon)n_{B1}^{bc}(\hat{\boldsymbol{p}},\epsilon)\right]\\ &+\int_{\text{hit}-} \frac{d\Omega_p}{4\pi}\hat{\boldsymbol{p}}\left[\int_{\epsilon_{\max}(\hat{\boldsymbol{p}})}^{E_c} d\epsilon\,\nu(\hat{\boldsymbol{p}},\epsilon)n_{B2}^{bc}(\hat{\boldsymbol{p}},\epsilon) + 2\int_{\epsilon_2(\hat{\boldsymbol{p}})}^{\epsilon_{\max}(\hat{\boldsymbol{p}})} d\epsilon\,\nu(\hat{\boldsymbol{p}},\epsilon)n_{B2}^{bc}(\hat{\boldsymbol{p}},\epsilon)\right]\\ &+\int_{\text{hit}} \frac{d\Omega_p}{4\pi}\hat{\boldsymbol{p}}\left[2\int_{\epsilon_0(\hat{\boldsymbol{p}})}^{\epsilon_{\min}(\hat{\boldsymbol{p}})} d\epsilon\,\nu(\hat{\boldsymbol{p}},\epsilon)n_{Bi}^{K}(\hat{\boldsymbol{p}},\epsilon)\right].\end{aligned} \tag{3.69}$$

Here, $\int_{\text{hit}+}$ ($\int_{\text{hit}-}$) means integration over trajectories that intersect the cylinder with $\hat{\boldsymbol{n}}\cdot\hat{\boldsymbol{p}} > 0$ ($\hat{\boldsymbol{n}}\cdot\hat{\boldsymbol{p}} < 0$), $\hat{\boldsymbol{n}} = \hat{\boldsymbol{r}}$ is the unit normal to the surface $r = R$, and $\int_{\text{hit}} = \int_{\text{hit}+} + \int_{\text{hit}-}$. The distribution functions n_{Bi}^K are the distributions in region K. The limits of energy integration are defined as $\epsilon_0(\hat{\boldsymbol{p}}) = a(\hat{\boldsymbol{p}}) + \Delta$, $\epsilon_2(\hat{\boldsymbol{p}}) = a_{\max<}(\hat{\boldsymbol{p}}) + \Delta$, $\epsilon_3(\hat{\boldsymbol{p}}) = a_{\max>}(\hat{\boldsymbol{p}}) + \Delta$, $\epsilon_{\min}(\hat{\boldsymbol{p}}) = \min\{\epsilon_2(\hat{\boldsymbol{p}}), \epsilon_3(\hat{\boldsymbol{p}})\}$, and $\epsilon_{\max}(\hat{\boldsymbol{p}}) = \max\{\epsilon_2(\hat{\boldsymbol{p}}), \epsilon_3(\hat{\boldsymbol{p}})\}$, where $a_{\max<}(\hat{\boldsymbol{p}})$ $[a_{\max>}(\hat{\boldsymbol{p}})]$ is the maximum of $a(\hat{\boldsymbol{p}})$ towards (away from) the cylinder along $\boldsymbol{r} = \boldsymbol{r}_0 + s\hat{\boldsymbol{p}}$, and $\boldsymbol{r}_0$ is the point where $\boldsymbol{I}$ is evaluated.

To proceed, we need to determine the distribution functions $n_{Bi}^{bc} = \phi_{Bi}^{bc} + 1/2$ using the mesoscopic boundary condition of Sec. 3.4.1, see Eqs. (3.43) and (3.44). To calculate A and B, we need the incident distributions on the surface of the cylinder. Consider an incident quasiparticle of type $B2$ with energy ϵ and direction $\hat{\boldsymbol{p}}$ ($\hat{\boldsymbol{n}}\cdot\hat{\boldsymbol{p}} > 0$). A possible situation is again shown in Fig. 3.6. In region M $[\epsilon > \epsilon_3(\hat{\boldsymbol{p}})]$, the quasiparticle originates from the far region, and thus $n_{B2} = 0$. In region L $[\epsilon_0(\hat{\boldsymbol{p}}) = \epsilon_2(\hat{\boldsymbol{p}}) \le \epsilon \le \epsilon_3(\hat{\boldsymbol{p}})]$, the quasiparticle originates from the cylinder indirectly via Andreev reflection, and so $n_{B2} = n_{B1}^{bc}$. These are quasiparticles bound to the near region. Note that on the surface of the cylinder, the regions N and K are not relevant. The same argument can be made for incident quasiparticles of type $B1$. In this case, $n_{B1} = 0$ in region M and $n_{B1} = n_{B2}^{bc}$ in region L.

For the boundary condition, we need to translate the above discussion into the language of the excitation picture. For every quasiparticle state with energy ϵ and direction $\hat{\boldsymbol{p}}$, there is a corresponding state with energy $-\epsilon$ and direction $-\hat{\boldsymbol{p}}$. This means that the region M satisfies either $\epsilon > \epsilon_3(\hat{\boldsymbol{p}})$ or $\epsilon < -\epsilon_3(-\hat{\boldsymbol{p}})$. We call these free states. Region L satisfies either $\epsilon_0(\hat{\boldsymbol{p}}) \le \epsilon \le \epsilon_3(\hat{\boldsymbol{p}})$ or $-\epsilon_3(-\hat{\boldsymbol{p}}) \le \epsilon \le -\epsilon_0(-\hat{\boldsymbol{p}})$. We call these bound states. For free states, the incident distribution functions are $\phi_{Bi} = \phi_{Bi}^{\infty} = 1/2 - \theta(\epsilon + p_F \boldsymbol{v}\cdot\hat{\boldsymbol{p}})$. For bound states, the incident distribution functions are $\phi_{B1} = \phi_{B2}^{bc}$ and $\phi_{B2} = \phi_{B1}^{bc}$. Substituting the incident distributions into Eqs. (3.45) and (3.46), and simplifying a bit, we obtain a system of self-consistency equations for A and B,

$$\begin{aligned}\int_{\text{free}} d\Omega_p \hat{\boldsymbol{n}}\cdot\hat{\boldsymbol{p}}\,\nu(\hat{\boldsymbol{p}},\epsilon)\phi_{Bi}^{\infty}(\hat{\boldsymbol{p}},\epsilon) &= \left[\int_{\text{free}} d\Omega_p \hat{\boldsymbol{n}}\cdot\hat{\boldsymbol{p}}\,\nu(\hat{\boldsymbol{p}},\epsilon)\right]\frac{g(\epsilon)B(\epsilon)}{2} \\ &\quad + \left[-4g^{-1}(\epsilon) + \int_{\text{free}} d\Omega_p |\hat{\boldsymbol{n}}\cdot\hat{\boldsymbol{p}}|\right]\frac{g(\epsilon)A(\epsilon)}{2},\end{aligned} \tag{3.70}$$

$$\begin{aligned}\int_{\text{free}} d\Omega_p |\hat{\boldsymbol{n}}\cdot\hat{\boldsymbol{p}}|\phi_{Bi}^{\infty}(\hat{\boldsymbol{p}},\epsilon) &= \left[\int_{\text{free}} d\Omega_p |\hat{\boldsymbol{n}}\cdot\hat{\boldsymbol{p}}|\right]\frac{g(\epsilon)B(\epsilon)}{2} \\ &\quad + \left[\int_{\text{free}} d\Omega_p \hat{\boldsymbol{n}}\cdot\hat{\boldsymbol{p}}\,\nu^{-1}(\hat{\boldsymbol{p}},\epsilon)\right]\frac{g(\epsilon)A(\epsilon)}{2}.\end{aligned} \tag{3.71}$$

We have seen that, at fixed energy ϵ, the free states can be divided into two categories, $F_1 = \{\hat{\boldsymbol{p}}\,|\,\epsilon_3(\hat{\boldsymbol{p}}) < \epsilon\}$ and $F_2 = \{\hat{\boldsymbol{p}}\,|\,\epsilon_3(-\hat{\boldsymbol{p}}) < -\epsilon\}$. Using the definition of ϵ_3, these can be written as $F_1 = \{\hat{\boldsymbol{p}}\,|\,a_{\max>}(\hat{\boldsymbol{p}}) < \epsilon - \Delta\}$ and $F_2 = \{\hat{\boldsymbol{p}}\,|\,a_{\max>}(-\hat{\boldsymbol{p}}) < -\epsilon - \Delta\} = \{\hat{\boldsymbol{p}}\,|\,a_{\min>}(\hat{\boldsymbol{p}}) > \epsilon + \Delta\}$. If both F_1 and F_2 are empty, then Eq. (3.70) shows that $A = 0$, but neither (3.70) nor (3.71) fixes the value of B. Since all states are bound, we make the natural assumption that $gB/2 = 1/2 - \theta(\epsilon)$, so that $\phi_{Bi}^{bc} = 1/2 - \theta(\epsilon)$. If either F_1 or F_2 is empty, it is straightforward to see that Eqs. (3.70) and (3.71) are satisfied by $A = 0$ and $gB/2 = 1/2 - \theta(\epsilon)$. Let us define

$$\mathcal{E} = -\min_{\hat{\boldsymbol{p}}} \epsilon_3(\hat{\boldsymbol{p}}). \tag{3.72}$$

We find that if $|\epsilon| < \mathcal{E}$, then neither F_1 nor F_2 is empty. The solution to Eqs. (3.70) and (3.71) is no longer trivial, and we need to resort to numerical methods. Note that if $\mathcal{E} \le 0$, the condition $|\epsilon| < \mathcal{E}$ cannot be satisfied. In this case, at least one of F_1 and F_2 is empty, and so $\phi_{Bi}^{bc} = 1/2 - \theta(\epsilon)$.

The force exerted on the cylinder can be calculated using Eqs. (3.28) and (3.29). First of all, Eq. (3.29) shows that the force per unit length is

$$\boldsymbol{f} = \int_{-\pi}^{\pi} R d\varphi \hat{\boldsymbol{n}}\cdot\overleftrightarrow{\boldsymbol{\Pi}}. \tag{3.73}$$

The stress tensor is determined by Eq. (3.28). Substituting the distributions and simplifying leads to

$$\begin{aligned}\overleftrightarrow{\boldsymbol{\Pi}} = 2v_F p_F N(0)\theta(\mathcal{E})\int_0^{\mathcal{E}} d\epsilon \int_{\text{free}} \frac{d\Omega_p}{4\pi}\hat{\boldsymbol{p}}\hat{\boldsymbol{p}}\bigg\{&\frac{g(\epsilon)A(\epsilon)}{2}\nu^{-1}(\hat{\boldsymbol{p}},\epsilon) \\ &+ \operatorname{sgn}(\hat{\boldsymbol{n}}\cdot\hat{\boldsymbol{p}})\left[\frac{g(\epsilon)B(\epsilon)}{2} - \phi_{Bi}^{\infty}(\hat{\boldsymbol{p}},\epsilon)\right]\bigg\}.\end{aligned} \tag{3.74}$$

We find that the force vanishes if $\mathcal{E} \leq 0$ at each point on the surface of the cylinder, meaning that the critical velocity can be defined as the smallest velocity at which $\mathcal{E} > 0$ somewhere on the surface. This is identical to the definition that we proposed in Sec. 3.2. Note that the critical velocity has to be at least as large as the Landau velocity. To see this, consider the condition $\mathcal{E} > 0$. This implies $\min_{\hat{\boldsymbol{p}}} a_{\max>}(\hat{\boldsymbol{p}}) < -\Delta$, and thus there exists a direction $\hat{\boldsymbol{p}}_0$ such that $a_{\max>}(\hat{\boldsymbol{p}}_0) < -\Delta$. The value of $a(\hat{\boldsymbol{p}}_0)$ in the far region is $a_\infty(\hat{\boldsymbol{p}}_0) = -p_F \boldsymbol{v} \cdot \hat{\boldsymbol{p}}_0$. This has to smaller than or equal to $a_{\max>}(\hat{\boldsymbol{p}}_0)$, and so $-p_F \boldsymbol{v} \cdot \hat{\boldsymbol{p}}_0 < -\Delta$, which cannot be satisfied if $v \leq v_L$.

Our main objective is to determine the critical velocity. Below the critical velocity, $\mathcal{E} \leq 0$ everywhere on the surface of the cylinder, and therefore the scattered distributions are $\phi_{Bi}^{bc} = 1/2 - \theta(\epsilon)$. Above the critical velocity, there are points on the cylinder where the scattered distributions ϕ_{Bi}^{bc} are significantly more complicated, since they depend on the entire flow field around the cylinder (this is because A and B depend on the maximum and minimum of a along different trajectories). In order to simplify calculations, we approximate $\phi_{Bi}^{bc} = 1/2 - \theta(\epsilon)$ also at supercritical velocities. This is a reasonable approximation if the velocity is not too large, since the true scattered distributions deviate from the approximate ones only in the interval $|\epsilon| < \mathcal{E}$, which is narrow. In this approximation, the stress tensor (3.74) simplifies to

$$\overleftrightarrow{\boldsymbol{\Pi}} = -2 v_F p_F N(0) \int \frac{d\Omega_p}{4\pi} \hat{\boldsymbol{p}}\hat{\boldsymbol{p}}\, \theta[-\epsilon_3(\hat{\boldsymbol{p}})] \operatorname{sgn}(\hat{\boldsymbol{n}} \cdot \hat{\boldsymbol{p}}) \epsilon_3(\hat{\boldsymbol{p}}). \tag{3.75}$$

Substituting $\phi_{Bi}^{bc} = 1/2 - \theta(\epsilon)$ into Eq. (3.69) yields $\boldsymbol{I} = \boldsymbol{I}_1$ in model 1 and $\boldsymbol{I} = \boldsymbol{I}_2$ in model 2, where

$$\begin{aligned}\boldsymbol{I}_1 = &\int_{\text{hit}} \frac{d\Omega_p}{2\pi} \hat{\boldsymbol{p}}\, \theta\left[-\epsilon_2(\hat{\boldsymbol{p}})\right] \left\{ \sqrt{a(\hat{\boldsymbol{p}})^2 - \Delta^2} - \sqrt{\left[\epsilon_2(\hat{\boldsymbol{p}}) - a(\hat{\boldsymbol{p}})\right]^2 - \Delta^2} \right\} \\ &- \int_{\text{hit}} \frac{d\Omega_p}{4\pi} \hat{\boldsymbol{p}}\, \theta\left[-\epsilon_{\max}(\hat{\boldsymbol{p}})\right] \left\{ \sqrt{a(\hat{\boldsymbol{p}})^2 - \Delta^2} - \sqrt{\left[\epsilon_{\max}(\hat{\boldsymbol{p}}) - a(\hat{\boldsymbol{p}})\right]^2 - \Delta^2} \right\}\end{aligned}$$

and

$$\begin{aligned}\boldsymbol{I}_2 = &\int_{\text{hit}} \frac{d\Omega_p}{2\pi} \hat{\boldsymbol{p}}\, \theta\left[-\epsilon_0(\hat{\boldsymbol{p}})\right] \left\{ \sqrt{a(\hat{\boldsymbol{p}})^2 - \Delta^2} \right\} \\ &- \int_{\text{hit}} \frac{d\Omega_p}{2\pi} \hat{\boldsymbol{p}}\, \theta\left[-\epsilon_3(\hat{\boldsymbol{p}})\right] \left\{ \sqrt{a(\hat{\boldsymbol{p}})^2 - \Delta^2} - \sqrt{\left[\epsilon_3(\hat{\boldsymbol{p}}) - a(\hat{\boldsymbol{p}})\right]^2 - \Delta^2} \right\} \\ &+ \int_{\text{hit}} \frac{d\Omega_p}{4\pi} \hat{\boldsymbol{p}}\, \theta\left[-\epsilon_{\max}(\hat{\boldsymbol{p}})\right] \left\{ \sqrt{a(\hat{\boldsymbol{p}})^2 - \Delta^2} - \sqrt{\left[\epsilon_{\max}(\hat{\boldsymbol{p}}) - a(\hat{\boldsymbol{p}})\right]^2 - \Delta^2} \right\}.\end{aligned}$$

Using $\boldsymbol{I}_1$ and $\boldsymbol{I}_2$, we can solve the flow field for models 1 and 2 from Eqs. (3.66), (3.67), and (3.68). These form a set of nonlinear, nonlocal integro-differential equations, and need to be solved numerically. We have used $F_1^s = 5.4$, which is the zero-pressure value in ^{3}He. For details on the numerical methods used, see Sec. VI of Pub. II.

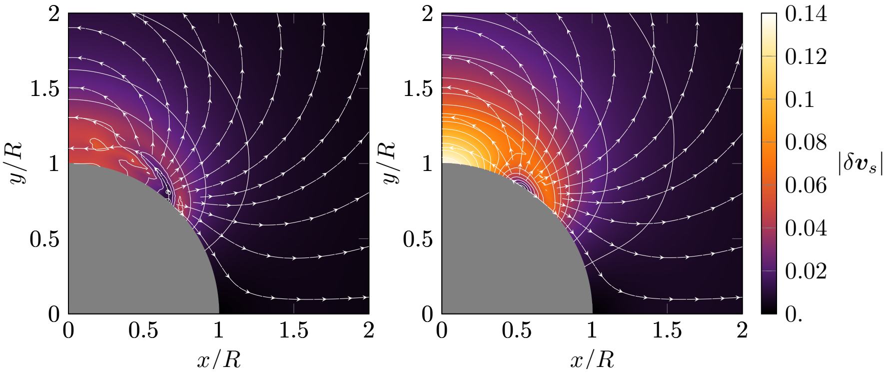

(a) Model 1 (b) Model 2

Figure 3.11: The deviation $\delta \boldsymbol{v}_s$ of the superfluid velocity field from the ideal fluid velocity field (3.11) at $v = 0.8v_L$ in (a) model 1 and (b) model 2. The unit of velocity is v. The cylinder is represented by the grey segment of a disk of radius R. The color map represents the magnitude of $\delta \boldsymbol{v}_s$. Contour lines of constant $|\delta \boldsymbol{v}_s|$ are shown at intervals $0.01v$, and the stream lines indicate the direction of $\delta \boldsymbol{v}_s$. The vector field $\delta \boldsymbol{v}_s$ is symmetric under reflection over the x axis and antisymmetric under reflection over the y axis. The figure was originally published in Pub. II.

Figure 3.11 shows the deviation of the superfluid velocity field from the ideal fluid velocity field (3.11) for models 1 and 2 at $v = 0.8v_L$. We see that the velocity fields differ from each other, and from the ideal fluid velocity field, in the region $|x| \lesssim R$, $|y| \lesssim 2R$. Figure 3.12 shows the vector field $\boldsymbol{\alpha}$ for ideal fluid, model 1, and model 2 at $v = 0.8v_L$. Again, the fields differ from one another only in the region $|x| \lesssim R$, $|y| \lesssim 2R$.

To obtain the critical velocity v_c, we calculate the maximum of $\mathcal{E}$ [see Eq. (3.72)] on the surface of the cylinder at different values of v using the numerically calculated vector field $\boldsymbol{\alpha}$, and determine the velocity at which it crosses zero. We find that the critical velocities for the ideal fluid, model 1, and model 2 are approximately equal, $v_c \approx 1.12v_L$. This implies that the critical velocity is predominantly determined by the flow field outside the region where the fields $\boldsymbol{\alpha}$ differ from one another. To calculate the force exerted on the cylinder at fixed v, we use Eqs. (3.73) and (3.75) together with the numerically obtained vector field $\boldsymbol{\alpha}$. Figure 3.13 shows the force exerted on a macroscopic cylinder as a function of velocity for ideal fluid, model 1, and model 2. As a comparison, the result for a microscopic cylinder is also shown. We see that the spatial variation of the flow field has a significant effect on the force. Models 1 and 2 produce nearly identical forces, somewhat smaller than the ideal flow field.

It is instructive to compare the force in the superfluid state to the force in the normal state. The normal-state force is significantly easier to calculate since one does not need to know the flow field. This follows from the fact that if $\Delta = 0$, then $\Theta(\hat{\boldsymbol{p}}, \epsilon) = N(\hat{\boldsymbol{p}}, \epsilon) = 1$. Using Eqs. (3.28) and (3.29) together with the boundary condition of Sec. 3.4.1, Eqs. (3.43) and (3.44), we obtain

$$F_n = \frac{43\pi}{144} v_F p_F^2 N(0)\sigma v, \tag{3.76}$$

which is identical to the result calculated in Ref. [82]. In each of the three cases considered here (ideal fluid, model 1, and model 2), the ratio F/F_n is zero if $v \leq v_c \approx 1.12 v_L$, is of the order of 10^{-2} at $v = 2v_L$, and approaches unity as $v \to \infty$.

How do the results obtained here compare with the experimental data by the Lancaster group [43]? In the experiments, a NbTi wire of radius 50 μm ($\gg \xi_0 \approx 80$ nm) is moved at constant velocity (excluding the brief periods of initial and final acceleration) through ^{3}He-B at zero pressure and at temperature $\sim 150\ \mu\text{K} \approx 0.15 T_c$. The force exerted on the wire is deduced from the measured temperature response. No clear sign of a critical velocity is seen (see Fig. 3(b) in Ref. [43]). Instead, the force increases gradually as the velocity of the wire is increased from zero to $2.5 v_L$ (since $T > 0$, there is some additional damping due to thermal quasiparticles). At $v = 2v_L$, the ratio F/F_n is of the order of 10^{-5}, which is three orders of magnitude smaller than our model calculations predict. This discrepancy is likely due to the several approximations introduced in Sec. 3.3.3.

3.7 Equilibrium in the near region

Thus far, we have assumed that there are no collisions between quasiparticles. In reality, we expect the collisions to play some role, since there are plenty of quasiparticles present in the near region at high velocities. A proper calculation would take the collisions into account in the transport equations (3.15) and (3.16), but this complicates the analysis significantly. Here, we only study whether the collisions could lead to a steady state where all the quasiparticle states in the near region are in thermal equilibrium in the object frame, but the far region is not affected by the cylinder. This could be possible at velocities less than v_L. Contrary to the previous sections, we now allow the gap to become anisotropic due to the flow.

We work in the object frame. The distribution functions in the near region are given by $\phi_{Bi} = 1/2 - \theta(\epsilon)$. Note that these are also consistent with the mesoscopic boundary condition of Sec. 3.4.1, Eqs. (3.43) and (3.44). In the far region, the flow velocity is $\boldsymbol{v}_s = -\boldsymbol{v}$, the gap is isotropic, $|\Delta(\hat{\boldsymbol{p}})| = \Delta (= \Delta_B)$, and $\boldsymbol{\alpha} = -p_F \boldsymbol{v}$. Since we assume that $v < v_L$, we have $a + \Delta > 0$ always, and so a quasiparticle with non-positive energy cannot exist in the far region. Since there are only quasiparticles with negative energies in the near region, these cannot escape to the far region. This is consistent with our assumption that the far region is unaffected by the cylinder. We can use the distribution functions $\phi_{Bi} = 1/2 - \theta(\epsilon)$ also in the far region, since $n_{Bi} = 1 - \theta(\epsilon) = 0$ if $\epsilon \geq a + \Delta > 0$, which is the requirement that there are no quasiparticles present.

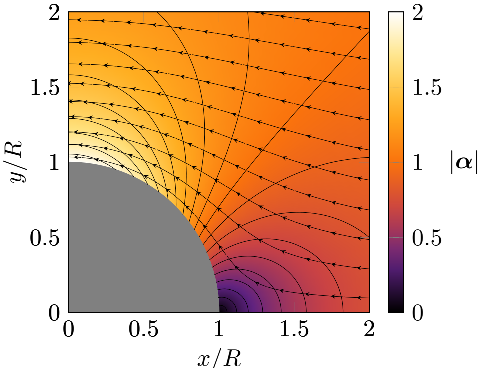

(a) Ideal fluid

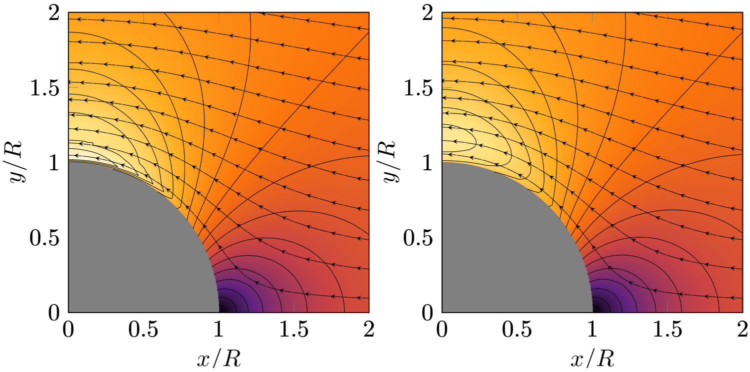

(b) Model 1

(c) Model 2

Figure 3.12: The vector field $\boldsymbol{\alpha}$ at $v = 0.8v_L$ in (a) ideal fluid, (b) model 1, and (c) model 2. The unit of $\boldsymbol{\alpha}$ is $p_F v$. The cylinder is represented by the grey segment of a disk of radius R. The color map represents the magnitude of $\boldsymbol{\alpha}$. Contour lines of constant $|\boldsymbol{\alpha}|$ are shown at intervals $0.1v$, and the stream lines indicate the direction of $\boldsymbol{\alpha}$. The vector field $\boldsymbol{\alpha}$ is symmetric under reflection over the x axis and antisymmetric under reflection over the y axis. The figure was originally published in Pub. II.

If $\phi_{Bi} = 1/2 - \theta(\epsilon)$, Eqs. (3.35) and (3.20) imply that we can write the gap as

$$|\Delta(\hat{\boldsymbol{p}})|^2 = \Delta_\parallel^2 p_\parallel^2 + \Delta_\perp^2 p_\perp^2, \tag{3.77}$$

where we have decomposed the momentum as $\hat{\boldsymbol{p}} = p_\parallel \hat{\boldsymbol{\alpha}} + \boldsymbol{p}_\perp$, with $\boldsymbol{p}_\perp \cdot \hat{\boldsymbol{\alpha}} = 0$ and $p_\parallel^2 + p_\perp^2 = 1$. Substituting the gap and the distribution functions into Eq. (3.36) yields

$$\boldsymbol{I} = -\frac{1}{3}\theta(\alpha - \Delta_\parallel)\frac{(\alpha^2 - \Delta_\parallel^2)^{3/2}}{\alpha^2 + \Delta_\perp^2 - \Delta_\parallel^2}\hat{\boldsymbol{\alpha}}. \tag{3.78}$$

Equation (3.35) shows that $\boldsymbol{\alpha}$ and $\boldsymbol{v}_s$ point in the same direction,

$$\boldsymbol{\alpha} = \alpha \hat{\boldsymbol{v}}_s. \tag{3.79}$$

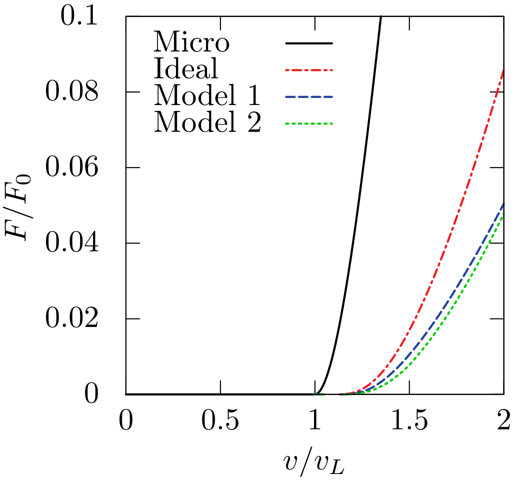

Figure 3.13: The force exerted on a cylinder moving in zero-temperature superfluid as a function of velocity. We show results for a microscopic cylinder (micro, see Sec. 3.5) and for a macroscopic cylinder in three different approximations, ideal fluid, model 1, and model 2 (see Sec. 3.6).

Consequently, we can write the mass current density (3.38) as

$$\boldsymbol{j} = \rho_s \boldsymbol{v}_s, \tag{3.80}$$

where

$$\rho_s = \frac{2}{3} m v_F p_F N(0) \left[1 + (3 + F_1^s) \frac{I}{p_F v_s} \right]. \tag{3.81}$$

Equations (3.35) and (3.20) determine α, $\Delta_\parallel$, and $\Delta_\perp$ as a function of v_s. The solution at general temperatures has been discussed in Refs. [22, 23]. Figure 3.14 (a) shows α, j, ρ_s, $\Delta_\parallel$, and $\Delta_\perp$ as a function of v_s. We have used $F_1^s = 5.4$, which is the zero-pressure value in ^{3}He. As a comparison, Fig. 3.14 (b) shows α, j, and ρ_s as a function of v_s assuming that the gap is isotropic, $\Delta_\parallel = \Delta_\perp = \Delta$.

To determine the flow field, we need to solve the continuity equation (3.37). Combining this with Eqs. (3.23) and (3.80) leads to

$$\boldsymbol{\nabla} \cdot [\rho_s(v_s) \boldsymbol{v}_s] = 0, \tag{3.82}$$

$$\boldsymbol{v}_s = \frac{\hbar}{2m} \boldsymbol{\nabla} \psi, \tag{3.83}$$

which have to be solved with the boundary conditions $\hat{\boldsymbol{n}} \cdot \boldsymbol{v}_s = 0$ at the surface of the cylinder and $\boldsymbol{v}_s = -\boldsymbol{v}$ far away from the cylinder.

If $v \leq v_L/2$, the velocity field is given by the ideal fluid velocity field (3.11). This stems from the fact that ρ_s is constant if $v_s \leq v_L$ (see Fig. 3.14). At higher velocities, one needs to rely on numerical methods (see Publication II for details). For self-consistent gap, we have not been able to find a solution if $v > v_L/2$. This

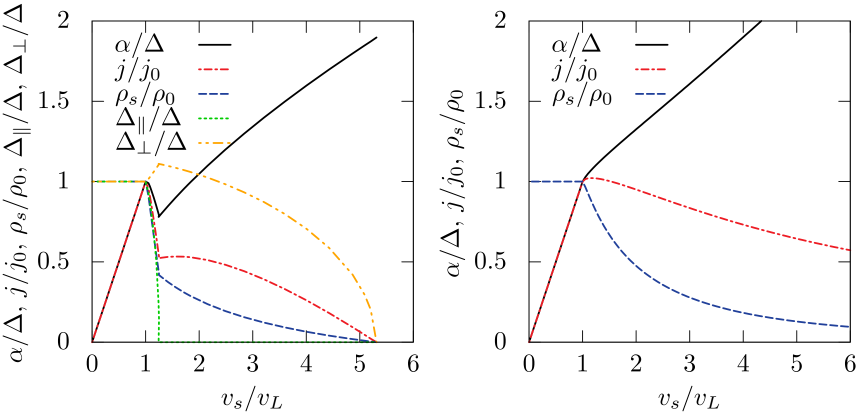

(a) Self-consistent gap (b) Isotropic gap

Figure 3.14: The dependence of the variables α, j, and ρ_s on the superfluid velocity v_s, assuming $\phi_{Bi} = 1/2 - \theta(\epsilon)$ and (a) anisotropic, self-consistent gap (3.77), (b) isotropic gap Δ. In addition, (a) shows the dependence of the components $\Delta_\parallel$ and $\Delta_\perp$ of the gap on v_s. The units of j and ρ_s are $j_0 = (2/3)mv_F N(0)\Delta$ and $\rho_0 = (2/3)mv_F p_F N(0)$, respectively. We have used $F_1^s = 5.4$, which is the zero-pressure value in ^{3}He.

simply means that our initial assumptions have been incorrect. A steady state in which the quasiparticle states in the near region are in thermal equilibrium in the object frame is not possible at zero temperature. A more detailed model to include quasiparticle collisions should be considered. If we assume isotropic gap, a solution can be found at velocities $v \lesssim 0.7 v_L$. For further discussion, see Pub. II.

Chapter 4

Conclusions

The work presented in this thesis comprised two projects related to superfluid ^{3}He. In the first project (Pubs. I and III, Chap. 2), we studied how an isolated vortex line affects the spin dynamics of ^{3}He-B. We found that under uniformly precessing magnetisation, the vortex radiates spin waves. These spin waves, carrying energy with them, cause magnetic relaxation in the system. We compared the predicted energy dissipation rate with experimental data, and found an agreement between the two.

In the second project (Pub. II, Chap. 3), we studied the drag force exerted on an object moving through zero-temperature superfluid ^{3}He. We found that the Landau criterion, although correctly predicting the velocity at which Cooper pair breaking becomes possible, cannot be used as such to predict the critical velocity for a macroscopic object. This is because the spatially varying flow field around the object can prevent the quasiparticles created at the surface of the object from escaping to the far region, thus effectively preventing momentum transfer from the object to the fluid and therefore suppressing (or even completely eliminating) the drag.

Plenty of work still remains to be done. In the first project, we solved the equation of motion (2.61) in two different approximations. Since the coefficients in Eq. (2.61) are periodic in time, one could search for an exact solution using Floquet theory [83, 84]. The predicted dissipation could also be compared to other experiments. Perhaps the most interesting theoretical exercise would be to include the Leggett–Takagi mechanism directly into the equations of motion. Spin diffusion could also be taken into account. In the second project, we showed how the critical velocity can increase from the Landau velocity owing to the spatial dependence of the flow field. However, the effect observed in the experiment by the Lancaster group [43] was even more dramatic than the prediction obtained with our simplified model. This means that, in future, one should relax the various assumptions we made in Sec. 3.3.3. As a first step, one could include quasiparticle collisions into the model, and take into account anisotropy of the energy gap.

Appendix A

Details on the Brinkman–Smith mode

In this appendix, we study the Leggett equations (2.40) and (2.41) assuming that the spin density $\boldsymbol{S}$ precesses uniformly about the external, static magnetic field $\boldsymbol{B}$ with a tipping angle β.

Let us write $\boldsymbol{S}(t) = \mathsf{R}(\boldsymbol{\omega}_{BS} t) \cdot \boldsymbol{S}_0$, where $\boldsymbol{\omega}_{BS} = \omega_{BS}\hat{\boldsymbol{B}}$ and $\hat{\boldsymbol{S}}_0 \cdot \hat{\boldsymbol{S}}_{eq} = \cos\beta$, with $\hat{\boldsymbol{S}}_{eq} = -\hat{\boldsymbol{B}}$ [see Eq. (2.42)] and $0 < \beta < \pi$. Due to the form of $\boldsymbol{S}(t)$, it is convenient to define a new vector $\boldsymbol{\psi}(t)$ which satisfies $\boldsymbol{\theta}(t) = \mathsf{R}(\boldsymbol{\omega}_{BS} t) \cdot \boldsymbol{\psi}(t)$. We shall show that $\boldsymbol{\psi}$ must be independent of time. Plugging $\boldsymbol{S}$ and $\boldsymbol{\theta}$ into Eqs. (2.40) and (2.41) yields

$$(\boldsymbol{\omega}_{BS} - \boldsymbol{\omega}_L) \times \boldsymbol{S}_0 = 4\lambda_D \frac{\sin\psi}{\psi}(1 + 4\cos\psi)\boldsymbol{\psi}, \tag{A.1}$$

$$\begin{aligned}\dot{\boldsymbol{\psi}} + \boldsymbol{\omega}_{BS} \times \boldsymbol{\psi} &= \frac{\psi}{2}\cot\left(\frac{\psi}{2}\right)\boldsymbol{s}_0 + \frac{1}{2}\boldsymbol{s}_0 \times \boldsymbol{\psi} \\ &+ \frac{1 - (\psi/2)\cot(\psi/2)}{\psi^2}\boldsymbol{\psi}(\boldsymbol{\psi}\cdot\boldsymbol{s}_0),\end{aligned} \tag{A.2}$$

where we have denoted $\boldsymbol{s}_0 = \mu_0\gamma_0^2\boldsymbol{S}_0/\chi + \boldsymbol{\omega}_L$. We find that the system has a trivial solution $\boldsymbol{\psi} = \boldsymbol{0}$, $\boldsymbol{s}_0 = \boldsymbol{0}$. From now on, let us assume that $\boldsymbol{\psi}$ is not identically zero. We can also assume that $\boldsymbol{s}_0 \neq \boldsymbol{0}$, since $\boldsymbol{s}_0 = \boldsymbol{0}$ would correspond to static equilibrium with $\beta = 0$ [see Eq. (2.42)] .

Let us take the norm on both sides of Eq. (A.1). We obtain

$$|\omega_{BS} - \omega_L| S_0 \sin\beta = 4\lambda_D |\sin\psi(1 + 4\cos\psi)|, \tag{A.3}$$

which implies that ψ must be independent of time, $\psi(t) = \psi_0 \neq 0$. Substituting this back into Eqs. (A.1) and (A.2) yields

$$(\boldsymbol{\omega}_{BS}-\boldsymbol{\omega}_L)\times\boldsymbol{S}_0 = 4\lambda_D\sin\psi_0(1+4\cos\psi_0)\hat{\boldsymbol{\psi}}, \tag{A.4}$$

$$\begin{aligned}\psi_0\dot{\hat{\boldsymbol{\psi}}}+\psi_0\boldsymbol{\omega}_{BS}\times\hat{\boldsymbol{\psi}} &= \frac{\psi_0}{2}\cot\left(\frac{\psi_0}{2}\right)\boldsymbol{s}_0+\frac{\psi_0}{2}\boldsymbol{s}_0\times\hat{\boldsymbol{\psi}}\\ &\quad+\left[1-\frac{\psi_0}{2}\cot\left(\frac{\psi_0}{2}\right)\right]\hat{\boldsymbol{\psi}}(\hat{\boldsymbol{\psi}}\cdot\boldsymbol{s}_0).\end{aligned} \tag{A.5}$$

Let us calculate the dot product of Eq. (A.5) with $\hat{\boldsymbol{\psi}}$. Since $\hat{\boldsymbol{\psi}}$ is a unit vector, we must have $\hat{\boldsymbol{\psi}}\cdot\dot{\hat{\boldsymbol{\psi}}}=0$, and so we find that

$$\hat{\boldsymbol{\psi}}\cdot\boldsymbol{s}_0=0. \tag{A.6}$$

Plugging this back into Eqs. (A.4) and (A.5) results in

$$(\boldsymbol{\omega}_{BS}-\boldsymbol{\omega}_L)\times\boldsymbol{S}_0 = 4\lambda_D\sin\psi_0(1+4\cos\psi_0)\hat{\boldsymbol{\psi}}, \tag{A.7}$$

$$\dot{\hat{\boldsymbol{\psi}}} = \frac{1}{2}\cot\left(\frac{\psi_0}{2}\right)\boldsymbol{s}_0+\left(\frac{\boldsymbol{s}_0}{2}-\boldsymbol{\omega}_{BS}\right)\times\hat{\boldsymbol{\psi}}. \tag{A.8}$$

Equation (A.6) implies $\dot{\hat{\boldsymbol{\psi}}}\cdot\boldsymbol{s}_0=0$. Taking the dot product between Eq. (A.8) and $\boldsymbol{s}_0$ shows that

$$\hat{\boldsymbol{\psi}}\cdot(\boldsymbol{s}_0\times\boldsymbol{\omega}_{BS}) = \frac{1}{2}\cot\left(\frac{\psi_0}{2}\right)s_0^2. \tag{A.9}$$

Since $0<\beta<\pi$, we must have $\boldsymbol{s}_0 \nparallel \boldsymbol{\omega}_{BS}$. This means that the vectors $\hat{\boldsymbol{e}}_1=\hat{\boldsymbol{s}}_0$, $\hat{\boldsymbol{e}}_2=(\boldsymbol{s}_0\times\boldsymbol{\omega}_{BS})/|\boldsymbol{s}_0\times\boldsymbol{\omega}_{BS}|$, and $\hat{\boldsymbol{e}}_3=\hat{\boldsymbol{e}}_1\times\hat{\boldsymbol{e}}_2$ form an orthonormal basis. We can expand $\hat{\boldsymbol{\psi}}$ in this basis as $\hat{\boldsymbol{\psi}}=a_1\hat{\boldsymbol{e}}_1+a_2\hat{\boldsymbol{e}}_2+a_3\hat{\boldsymbol{e}}_3$. Equation (A.6) shows that $a_1=0$, while Eq. (A.9) shows that a_2 is a constant. Since $\hat{\boldsymbol{\psi}}$ is a unit vector, then a_3 must also be a constant, and hence $\dot{\hat{\boldsymbol{\psi}}}=\boldsymbol{0}$. We have therefore shown that $\boldsymbol{\psi}$ is a constant.

Writing $\boldsymbol{\psi}=\boldsymbol{\theta}_0$ as in Sec. 2.3.3, the Leggett equations can be written as

$$(\boldsymbol{\omega}_{BS}-\boldsymbol{\omega}_L)\times\boldsymbol{S}_0 = 4\lambda_D\sin\theta_0(1+4\cos\theta_0)\hat{\boldsymbol{\theta}}_0, \tag{A.10}$$

$$\boldsymbol{0} = \frac{1}{2}\cot\left(\frac{\theta_0}{2}\right)\boldsymbol{s}_0+\left(\frac{\boldsymbol{s}_0}{2}-\boldsymbol{\omega}_{BS}\right)\times\hat{\boldsymbol{\theta}}_0, \tag{A.11}$$

$$\hat{\boldsymbol{\theta}}_0\cdot\boldsymbol{s}_0=0, \tag{A.12}$$

or

$$(\boldsymbol{\omega}_{BS}-\boldsymbol{\omega}_L)\times\boldsymbol{s}_0 = \frac{4\Omega^2}{15}\sin\theta_0(1+4\cos\theta_0)\hat{\boldsymbol{\theta}}_0, \tag{A.13}$$

$$\boldsymbol{0} = \frac{1}{2}\cot\left(\frac{\theta_0}{2}\right)\boldsymbol{s}_0+\left(\frac{\boldsymbol{s}_0}{2}-\boldsymbol{\omega}_{BS}\right)\times\hat{\boldsymbol{\theta}}_0, \tag{A.14}$$

$$\hat{\boldsymbol{\theta}}_0\cdot\boldsymbol{s}_0=0, \tag{A.15}$$

where Ω is the longitudinal resonance frequency defined in Eq. (2.44).

Appendix B

Details on the mesoscopic boundary condition

In this appendix, we prove some properties of the mesoscopic boundary condition introduced in Sec. 3.4.

B.1 Planar wall

Using Eqs. (3.41) and (3.42), the conservation laws (3.39) and (3.40) can be written as

$$\int \frac{d\Omega_p}{4\pi}(\hat{\boldsymbol{n}}\cdot\hat{\boldsymbol{p}})N(\hat{\boldsymbol{p}},\epsilon)[\phi_{B1}(\hat{\boldsymbol{p}},\epsilon)+\phi_{B2}(\hat{\boldsymbol{p}},\epsilon)] = 0, \tag{B.1}$$

$$\int \frac{d\Omega_p}{4\pi}(\hat{\boldsymbol{n}}\cdot\hat{\boldsymbol{p}})\Theta(\hat{\boldsymbol{p}},\epsilon)[\phi_{B1}(\hat{\boldsymbol{p}},\epsilon)-\phi_{B2}(\hat{\boldsymbol{p}},\epsilon)] = 0. \tag{B.2}$$

Let us split the integrals over incoming (incident) excitations ($\hat{\boldsymbol{n}}\cdot\hat{\boldsymbol{p}} < 0$ for excitations of type $B1$ and $\hat{\boldsymbol{n}}\cdot\hat{\boldsymbol{p}} > 0$ for excitations of type $B2$) and outgoing (scattered) excitations ($\hat{\boldsymbol{n}}\cdot\hat{\boldsymbol{p}} > 0$ for excitations of type $B1$ and $\hat{\boldsymbol{n}}\cdot\hat{\boldsymbol{p}} < 0$ for excitations of type $B2$),

$$\begin{aligned} 0 = &\int_{\hat{\boldsymbol{n}}\cdot\hat{\boldsymbol{p}}<0}\frac{d\Omega_p}{4\pi}(\hat{\boldsymbol{n}}\cdot\hat{\boldsymbol{p}})N(\hat{\boldsymbol{p}},\epsilon)\phi_{B1}(\hat{\boldsymbol{p}},\epsilon) + \int_{\hat{\boldsymbol{n}}\cdot\hat{\boldsymbol{p}}>0}\frac{d\Omega_p}{4\pi}(\hat{\boldsymbol{n}}\cdot\hat{\boldsymbol{p}})N(\hat{\boldsymbol{p}},\epsilon)\phi_{B2}(\hat{\boldsymbol{p}},\epsilon) \\ &+ \int_{\hat{\boldsymbol{n}}\cdot\hat{\boldsymbol{p}}>0}\frac{d\Omega_p}{4\pi}(\hat{\boldsymbol{n}}\cdot\hat{\boldsymbol{p}})N(\hat{\boldsymbol{p}},\epsilon)\phi_{B1}(\hat{\boldsymbol{p}},\epsilon) + \int_{\hat{\boldsymbol{n}}\cdot\hat{\boldsymbol{p}}<0}\frac{d\Omega_p}{4\pi}(\hat{\boldsymbol{n}}\cdot\hat{\boldsymbol{p}})N(\hat{\boldsymbol{p}},\epsilon)\phi_{B2}(\hat{\boldsymbol{p}},\epsilon), \end{aligned} \tag{B.3}$$

$$\begin{aligned} 0 = &\int_{\hat{\boldsymbol{n}}\cdot\hat{\boldsymbol{p}}<0}\frac{d\Omega_p}{4\pi}(\hat{\boldsymbol{n}}\cdot\hat{\boldsymbol{p}})\Theta(\hat{\boldsymbol{p}},\epsilon)\phi_{B1}(\hat{\boldsymbol{p}},\epsilon) - \int_{\hat{\boldsymbol{n}}\cdot\hat{\boldsymbol{p}}>0}\frac{d\Omega_p}{4\pi}(\hat{\boldsymbol{n}}\cdot\hat{\boldsymbol{p}})\Theta(\hat{\boldsymbol{p}},\epsilon)\phi_{B2}(\hat{\boldsymbol{p}},\epsilon) \\ &+ \int_{\hat{\boldsymbol{n}}\cdot\hat{\boldsymbol{p}}>0}\frac{d\Omega_p}{4\pi}(\hat{\boldsymbol{n}}\cdot\hat{\boldsymbol{p}})\Theta(\hat{\boldsymbol{p}},\epsilon)\phi_{B1}(\hat{\boldsymbol{p}},\epsilon) - \int_{\hat{\boldsymbol{n}}\cdot\hat{\boldsymbol{p}}<0}\frac{d\Omega_p}{4\pi}(\hat{\boldsymbol{n}}\cdot\hat{\boldsymbol{p}})\Theta(\hat{\boldsymbol{p}},\epsilon)\phi_{B2}(\hat{\boldsymbol{p}},\epsilon). \end{aligned} \tag{B.4}$$

Using the definitions (3.45) and (3.46) of A and B, Eqs. (B.3) and (B.4) can be written as

$$A(\epsilon) = \int_{\hat{\boldsymbol{n}}\cdot\hat{\boldsymbol{p}}>0} d\Omega_p (\hat{\boldsymbol{n}}\cdot\hat{\boldsymbol{p}}) N(\hat{\boldsymbol{p}},\epsilon)\phi_{B1}(\hat{\boldsymbol{p}},\epsilon) + \int_{\hat{\boldsymbol{n}}\cdot\hat{\boldsymbol{p}}<0} d\Omega_p (\hat{\boldsymbol{n}}\cdot\hat{\boldsymbol{p}}) N(\hat{\boldsymbol{p}},\epsilon)\phi_{B2}(\hat{\boldsymbol{p}},\epsilon), \tag{B.5}$$

$$B(\epsilon) = \int_{\hat{\boldsymbol{n}}\cdot\hat{\boldsymbol{p}}>0} d\Omega_p (\hat{\boldsymbol{n}}\cdot\hat{\boldsymbol{p}}) \Theta(\hat{\boldsymbol{p}},\epsilon)\phi_{B1}(\hat{\boldsymbol{p}},\epsilon) - \int_{\hat{\boldsymbol{n}}\cdot\hat{\boldsymbol{p}}<0} d\Omega_p (\hat{\boldsymbol{n}}\cdot\hat{\boldsymbol{p}}) \Theta(\hat{\boldsymbol{p}},\epsilon)\phi_{B2}(\hat{\boldsymbol{p}},\epsilon). \tag{B.6}$$

Substituting the distributions from the boundary condition, Eqs. (3.43) and (3.44), we obtain

$$A(\epsilon) = \frac{g(\epsilon)}{2} A(\epsilon) \int d\Omega_p |\hat{\boldsymbol{n}}\cdot\hat{\boldsymbol{p}}| \Theta(\hat{\boldsymbol{p}},\epsilon) + \frac{g(\epsilon)}{2} B(\epsilon) \int d\Omega_p (\hat{\boldsymbol{n}}\cdot\hat{\boldsymbol{p}}) N(\hat{\boldsymbol{p}},\epsilon), \tag{B.7}$$

$$B(\epsilon) = \frac{g(\epsilon)}{2} A(\epsilon) \int d\Omega_p (\hat{\boldsymbol{n}}\cdot\hat{\boldsymbol{p}}) \frac{\Theta(\hat{\boldsymbol{p}},\epsilon)}{\nu(\hat{\boldsymbol{p}},\epsilon)} + \frac{g(\epsilon)}{2} B(\epsilon) \int d\Omega_p |\hat{\boldsymbol{n}}\cdot\hat{\boldsymbol{p}}| \Theta(\hat{\boldsymbol{p}},\epsilon). \tag{B.8}$$

Consider the second integral in Eq. (B.7). Let us make a change of variables from $\hat{\boldsymbol{p}}$ to $\underline{\hat{\boldsymbol{p}}} = \hat{\boldsymbol{p}} - 2\hat{\boldsymbol{n}}(\hat{\boldsymbol{n}}\cdot\hat{\boldsymbol{p}})$. The region of integration stays the same (unit sphere), $\hat{\boldsymbol{n}}\cdot\hat{\boldsymbol{p}} = -\hat{\boldsymbol{n}}\cdot\underline{\hat{\boldsymbol{p}}}$, and $d\Omega_p = d\Omega_{\underline{p}}$. If we assume that $\hat{\boldsymbol{n}}\cdot\boldsymbol{\alpha} = 0$ and $|\Delta(\underline{\hat{\boldsymbol{p}}})| = |\Delta(\hat{\boldsymbol{p}})|$, then $\boldsymbol{\alpha}\cdot\hat{\boldsymbol{p}} = \boldsymbol{\alpha}\cdot\underline{\hat{\boldsymbol{p}}}$, $\Theta(\hat{\boldsymbol{p}},\epsilon) = \Theta(\underline{\hat{\boldsymbol{p}}},\epsilon)$, and $N(\hat{\boldsymbol{p}},\epsilon) = N(\underline{\hat{\boldsymbol{p}}},\epsilon)$. This means that

$$\int d\Omega_p (\hat{\boldsymbol{n}}\cdot\hat{\boldsymbol{p}}) N(\hat{\boldsymbol{p}},\epsilon) = -\int d\Omega_{\underline{p}} (\hat{\boldsymbol{n}}\cdot\underline{\hat{\boldsymbol{p}}}) N(\underline{\hat{\boldsymbol{p}}},\epsilon), \tag{B.9}$$

and so the integral vanishes. The same is true for the first integral in Eq. (B.8). We are left with

$$A(\epsilon) = \frac{g(\epsilon)}{2} A(\epsilon) \int d\Omega_p |\hat{\boldsymbol{n}}\cdot\hat{\boldsymbol{p}}| \Theta(\hat{\boldsymbol{p}},\epsilon), \tag{B.10}$$

$$B(\epsilon) = \frac{g(\epsilon)}{2} B(\epsilon) \int d\Omega_p |\hat{\boldsymbol{n}}\cdot\hat{\boldsymbol{p}}| \Theta(\hat{\boldsymbol{p}},\epsilon). \tag{B.11}$$

Comparing the integrals here with the definition of g in Eq. (3.47) shows that the integrals are equal to $2g^{-1}$, and thus Eqs. (B.10) and (B.11) reduce to

$$A(\epsilon) = A(\epsilon), \tag{B.12}$$

$$B(\epsilon) = B(\epsilon). \tag{B.13}$$

This shows that the mesoscopic boundary condition, Eqs. (3.43) and (3.44), satisfies the conservation laws (3.39) and (3.40).

B.2 Microscopic cylinder

B.2.1 Conservation laws

Using Eqs. (3.41) and (3.42), the conservation laws (3.52) and (3.53) can be written as

$$\int_{r=\lambda} ds \int \frac{d\Omega_p}{4\pi} (\hat{\boldsymbol{r}}\cdot\hat{\boldsymbol{p}}) N(\hat{\boldsymbol{p}},\epsilon)[\phi_{B1}(\hat{\boldsymbol{p}},\epsilon,\boldsymbol{r}) + \phi_{B2}(\hat{\boldsymbol{p}},\epsilon,\boldsymbol{r})] = 0, \tag{B.14}$$

$$\int_{r=\lambda} ds \int \frac{d\Omega_p}{4\pi} (\hat{\boldsymbol{r}}\cdot\hat{\boldsymbol{p}}) \Theta(\hat{\boldsymbol{p}},\epsilon)[\phi_{B1}(\hat{\boldsymbol{p}},\epsilon,\boldsymbol{r}) - \phi_{B2}(\hat{\boldsymbol{p}},\epsilon,\boldsymbol{r})] = 0. \tag{B.15}$$

Note that N and Θ do not depend on $\boldsymbol{r}$, since $\boldsymbol{\alpha}$ and A are constants on the circle $r=\lambda$ due to the smallness of λ. Changing the order of integration yields

$$\int \frac{d\Omega_p}{4\pi} N(\hat{\boldsymbol{p}},\epsilon) \int_{r=\lambda} ds (\hat{\boldsymbol{r}}\cdot\hat{\boldsymbol{p}})[\phi_{B1}(\hat{\boldsymbol{p}},\epsilon,\boldsymbol{r}) + \phi_{B2}(\hat{\boldsymbol{p}},\epsilon,\boldsymbol{r})] = 0, \tag{B.16}$$

$$\int \frac{d\Omega_p}{4\pi} \Theta(\hat{\boldsymbol{p}},\epsilon) \int_{r=\lambda} ds (\hat{\boldsymbol{r}}\cdot\hat{\boldsymbol{p}})[\phi_{B1}(\hat{\boldsymbol{p}},\epsilon,\boldsymbol{r}) - \phi_{B2}(\hat{\boldsymbol{p}},\epsilon,\boldsymbol{r})] = 0. \tag{B.17}$$

Let us fix a direction $\hat{\boldsymbol{p}}$, and consider the integral

$$I_i = \int_{r=\lambda} ds (\hat{\boldsymbol{r}}\cdot\hat{\boldsymbol{p}}) \phi_{Bi}(\hat{\boldsymbol{p}},\epsilon,\boldsymbol{r}). \tag{B.18}$$

We decompose $\hat{\boldsymbol{p}}$ as $\hat{\boldsymbol{p}} = p_{\parallel}\hat{\boldsymbol{z}} + \boldsymbol{p}_{\perp}$, where $\boldsymbol{p}_{\perp}\cdot\hat{\boldsymbol{z}} = 0$ and $p_{\parallel}^2 + p_{\perp}^2 = 1$. If $\boldsymbol{p}_{\perp} = \boldsymbol{0}$, then $\hat{\boldsymbol{r}}\cdot\hat{\boldsymbol{p}} = 0$, and consequently $I_i = 0$. If $\boldsymbol{p}_{\perp} \neq \boldsymbol{0}$, we write $\hat{\boldsymbol{p}}_{\perp} = \cos\varphi_p \hat{\boldsymbol{x}} + \sin\varphi_p \hat{\boldsymbol{y}}$, so that $\hat{\boldsymbol{r}}\cdot\hat{\boldsymbol{p}} = p_{\perp}\cos(\varphi - \varphi_p)$. We split the line integral into four parts, corresponding to the two shaded regions and the two unshaded regions in Fig. 3.8,

$$\begin{aligned} I_i = {} & p_{\perp}\lambda \int_{\varphi_p-\delta\varphi/2}^{\varphi_p+\delta\varphi/2} d\varphi \cos(\varphi-\varphi_p)\phi_{Bi}(\hat{\boldsymbol{p}},\epsilon,\lambda,\varphi) \\ & + p_{\perp}\lambda \int_{\varphi_p+\pi-\delta\varphi/2}^{\varphi_p+\pi+\delta\varphi/2} d\varphi \cos(\varphi-\varphi_p)\phi_{Bi}(\hat{\boldsymbol{p}},\epsilon,\lambda,\varphi) \\ & + p_{\perp}\lambda \int_{\varphi_p+\delta\varphi/2}^{\varphi_p+\pi-\delta\varphi/2} d\varphi \cos(\varphi-\varphi_p)\phi_{Bi}(\hat{\boldsymbol{p}},\epsilon,\lambda,\varphi) \\ & + p_{\perp}\lambda \int_{\varphi_p+\pi+\delta\varphi/2}^{\varphi_p+2\pi-\delta\varphi/2} d\varphi \cos(\varphi-\varphi_p)\phi_{Bi}(\hat{\boldsymbol{p}},\epsilon,\lambda,\varphi). \end{aligned} \tag{B.19}$$

Shifting the integration variables ($\varphi \to \tilde{\varphi} = \varphi - \varphi_p$, $\varphi \to \tilde{\varphi} = \varphi - \varphi_p - \pi$, $\varphi \to \tilde{\varphi} = \varphi - \varphi_p - \pi/2$, and $\varphi \to \tilde{\varphi} = \varphi - \varphi_p + \pi/2$, respectively), this can be written as

$$\begin{aligned} I_i = p_\perp\lambda \int_{-\delta\varphi/2}^{\delta\varphi/2} d\tilde{\varphi} \cos\tilde{\varphi}\phi_{Bi}(\hat{\boldsymbol{p}}, \epsilon, \lambda, \varphi_p + \tilde{\varphi}) \\ - p_\perp\lambda \int_{-\delta\varphi/2}^{\delta\varphi/2} d\tilde{\varphi} \cos\tilde{\varphi}\phi_{Bi}(\hat{\boldsymbol{p}}, \epsilon, \lambda, \varphi_p + \pi + \tilde{\varphi}) \\ - p_\perp\lambda \int_{-\pi/2+\delta\varphi/2}^{\pi/2-\delta\varphi/2} d\tilde{\varphi} \sin\tilde{\varphi}\phi_{Bi}(\hat{\boldsymbol{p}}, \epsilon, \lambda, \varphi_p + \frac{\pi}{2} + \tilde{\varphi}) \\ + p_\perp\lambda \int_{-\pi/2+\delta\varphi/2}^{\pi/2-\delta\varphi/2} d\tilde{\varphi} \sin\tilde{\varphi}\phi_{Bi}(\hat{\boldsymbol{p}}, \epsilon, \lambda, \varphi_p - \frac{\pi}{2} + \tilde{\varphi}). \end{aligned} \tag{B.20}$$

Simplifying slightly, we obtain

$$\begin{aligned} I_i = p_\perp\lambda \int_{-\delta\varphi/2}^{\delta\varphi/2} d\tilde{\varphi} \cos\tilde{\varphi}[\phi_{Bi}(\hat{\boldsymbol{p}}, \epsilon, \lambda, \varphi_p + \tilde{\varphi}) - \phi_{Bi}(\hat{\boldsymbol{p}}, \epsilon, \lambda, \varphi_p + \pi + \tilde{\varphi})] \\ - p_\perp\lambda \int_{0}^{\pi/2-\delta\varphi/2} d\tilde{\varphi} \sin\tilde{\varphi}\Big[\phi_{Bi}(\hat{\boldsymbol{p}}, \epsilon, \lambda, \varphi_p + \frac{\pi}{2} + \tilde{\varphi}) \\ - \phi_{Bi}(\hat{\boldsymbol{p}}, \epsilon, \lambda, \varphi_p + \frac{\pi}{2} - \tilde{\varphi})\Big] \\ + p_\perp\lambda \int_{0}^{\pi/2-\delta\varphi/2} d\tilde{\varphi} \sin\tilde{\varphi}\Big[\phi_{Bi}(\hat{\boldsymbol{p}}, \epsilon, \lambda, \varphi_p - \frac{\pi}{2} + \tilde{\varphi}) \\ - \phi_{Bi}(\hat{\boldsymbol{p}}, \epsilon, \lambda, \varphi_p - \frac{\pi}{2} - \tilde{\varphi})\Big]. \end{aligned} \tag{B.21}$$

The points $(r = \lambda, \varphi = \varphi_p + \frac{\pi}{2} + \tilde{\varphi})$ and $(r = \lambda, \varphi = \varphi_p + \frac{\pi}{2} - \tilde{\varphi})$ lie on the same straight line along $\boldsymbol{p}_\perp$, as do the points $(r = \lambda, \varphi = \varphi_p - \frac{\pi}{2} + \tilde{\varphi})$ and $(r = \lambda, \varphi = \varphi_p - \frac{\pi}{2} - \tilde{\varphi})$. Since the distribution functions are constants along straight-line trajectories [see Eq. (3.32)], the second and third integrals vanish, and we are left with

$$I_i = p_\perp\lambda \int_{-\delta\varphi/2}^{\delta\varphi/2} d\tilde{\varphi} \cos\tilde{\varphi}[\phi_{Bi}(\hat{\boldsymbol{p}}, \epsilon, \lambda, \varphi_p + \tilde{\varphi}) - \phi_{Bi}(\hat{\boldsymbol{p}}, \epsilon, \lambda, \varphi_p + \pi + \tilde{\varphi})]. \tag{B.22}$$

Since $\delta\varphi$ is small, we can approximate

$$\begin{aligned} I_i &\approx p_\perp\lambda\delta\varphi \cos(0)[\phi_{Bi}(\hat{\boldsymbol{p}}, \epsilon, \lambda, \varphi_p + 0) - \phi_{Bi}(\hat{\boldsymbol{p}}, \epsilon, \lambda, \varphi_p + \pi + 0)] \\ &= p_\perp\lambda\delta\varphi[\phi_{Bi}(\hat{\boldsymbol{p}}, \epsilon, \lambda, \varphi_p) - \phi_{Bi}(\hat{\boldsymbol{p}}, \epsilon, \lambda, \varphi_p + \pi)]. \end{aligned} \tag{B.23}$$

Based on Fig. 3.8, we have $\delta\varphi/2 \approx \sin(\delta\varphi/2) = R/\lambda$, and so

$$\begin{aligned} I_i &\approx 2Rp_\perp[\phi_{Bi}(\hat{\boldsymbol{p}}, \epsilon, \lambda, \varphi_p) - \phi_{Bi}(\hat{\boldsymbol{p}}, \epsilon, \lambda, \varphi_p + \pi)] \\ &= 2Rp_\perp[\phi_{Bi}(\hat{\boldsymbol{p}}, \epsilon, \lambda\hat{\boldsymbol{p}}_\perp) - \phi_{Bi}(\hat{\boldsymbol{p}}, \epsilon, -\lambda\hat{\boldsymbol{p}}_\perp)]. \end{aligned} \tag{B.24}$$

Using Eqs. (B.18) and (B.24), Eqs. (B.16) and (B.17) can be written as

$$\begin{aligned} 0 &= \int \frac{d\Omega_p}{4\pi} N(\hat{\boldsymbol{p}},\epsilon) p_\perp [\phi_{B1}(\hat{\boldsymbol{p}},\epsilon,-\lambda\hat{\boldsymbol{p}}_\perp) - \phi_{B2}(\hat{\boldsymbol{p}},\epsilon,\lambda\hat{\boldsymbol{p}}_\perp)] \\ &\quad - \int \frac{d\Omega_p}{4\pi} N(\hat{\boldsymbol{p}},\epsilon) p_\perp [\phi_{B1}(\hat{\boldsymbol{p}},\epsilon,\lambda\hat{\boldsymbol{p}}_\perp) - \phi_{B2}(\hat{\boldsymbol{p}},\epsilon,-\lambda\hat{\boldsymbol{p}}_\perp)], \end{aligned} \tag{B.25}$$

$$\begin{aligned} 0 &= \int \frac{d\Omega_p}{4\pi} \Theta(\hat{\boldsymbol{p}},\epsilon) p_\perp [\phi_{B1}(\hat{\boldsymbol{p}},\epsilon,-\lambda\hat{\boldsymbol{p}}_\perp) + \phi_{B2}(\hat{\boldsymbol{p}},\epsilon,\lambda\hat{\boldsymbol{p}}_\perp)] \\ &\quad - \int \frac{d\Omega_p}{4\pi} \Theta(\hat{\boldsymbol{p}},\epsilon) p_\perp [\phi_{B1}(\hat{\boldsymbol{p}},\epsilon,\lambda\hat{\boldsymbol{p}}_\perp) + \phi_{B2}(\hat{\boldsymbol{p}},\epsilon,-\lambda\hat{\boldsymbol{p}}_\perp)]. \end{aligned} \tag{B.26}$$

In both of the above equations, the first integral involves only incoming excitations, while the second integral involves only outgoing excitations. Using the definitions (3.56) and (3.57) of A and B, Eqs. (B.25) and (B.26) can be written as

$$A(\epsilon) = \int d\Omega_p N(\hat{\boldsymbol{p}},\epsilon) p_\perp [\phi_{B1}(\hat{\boldsymbol{p}},\epsilon,\lambda\hat{\boldsymbol{p}}_\perp) - \phi_{B2}(\hat{\boldsymbol{p}},\epsilon,-\lambda\hat{\boldsymbol{p}}_\perp)], \tag{B.27}$$

$$B(\epsilon) = \int d\Omega_p \Theta(\hat{\boldsymbol{p}},\epsilon) p_\perp [\phi_{B1}(\hat{\boldsymbol{p}},\epsilon,\lambda\hat{\boldsymbol{p}}_\perp) + \phi_{B2}(\hat{\boldsymbol{p}},\epsilon,-\lambda\hat{\boldsymbol{p}}_\perp)]. \tag{B.28}$$

Substituting the distributions from the boundary condition, Eqs. (3.54) and (3.55), we obtain

$$A(\epsilon) = g(\epsilon) A(\epsilon) \int d\Omega_p p_\perp \Theta(\hat{\boldsymbol{p}},\epsilon), \tag{B.29}$$

$$B(\epsilon) = g(\epsilon) B(\epsilon) \int d\Omega_p p_\perp \Theta(\hat{\boldsymbol{p}},\epsilon). \tag{B.30}$$

Comparing the integrals here with the definition of g in Eq. (3.58) shows that the integrals are equal to g^{-1}, and so the equations reduce to

$$A(\epsilon) = A(\epsilon), \tag{B.31}$$

$$B(\epsilon) = B(\epsilon). \tag{B.32}$$

This shows that the mesoscopic boundary condition, Eqs. (3.54) and (3.55), satisfies the conservation laws (3.52) and (3.53).

B.2.2 Force

Combining Eqs. (3.28) and (3.29), the force $\boldsymbol{F}$ exerted on a cylindrical surface of radius λ around the cylinder is

$$\boldsymbol{F} = v_F p_F N(0) \int_{r=\lambda} dA \int \frac{d\Omega_p}{4\pi} (\hat{\boldsymbol{r}}\cdot\hat{\boldsymbol{p}})\hat{\boldsymbol{p}} \int_{-E_c}^{E_c} d\epsilon \Theta(\hat{\boldsymbol{p}},\epsilon)[\phi_{B1}(\hat{\boldsymbol{p}},\epsilon) - \phi_{B2}(\hat{\boldsymbol{p}},\epsilon)]. \tag{B.33}$$

Due to the translational invariance in the z direction, the integral over z gives a constant, and thus the force per unit length is

$$\boldsymbol{f} = v_F p_F N(0) \int_{r=\lambda} ds \int \frac{d\Omega_p}{4\pi} (\hat{\boldsymbol{r}} \cdot \hat{\boldsymbol{p}}) \hat{\boldsymbol{p}} \int_{-E_c}^{E_c} d\epsilon \Theta(\hat{\boldsymbol{p}}, \epsilon) [\phi_{B1}(\hat{\boldsymbol{p}}, \epsilon) - \phi_{B2}(\hat{\boldsymbol{p}}, \epsilon)]. \tag{B.34}$$

Here, the outermost integral is over the circumference of a circle of radius λ. Changing the order of integration yields

$$\boldsymbol{f} = v_F p_F N(0) \int_{-E_c}^{E_c} d\epsilon \int \frac{d\Omega_p}{4\pi} \hat{\boldsymbol{p}} \Theta(\hat{\boldsymbol{p}}, \epsilon) \int_{r=\lambda} ds (\hat{\boldsymbol{r}} \cdot \hat{\boldsymbol{p}}) [\phi_{B1}(\hat{\boldsymbol{p}}, \epsilon) - \phi_{B2}(\hat{\boldsymbol{p}}, \epsilon)]. \tag{B.35}$$

Using Eqs. (B.18) and (B.24), we obtain

$$\begin{aligned} \boldsymbol{f} \approx 2R v_F p_F N(0) \int_{-E_c}^{E_c} d\epsilon \int \frac{d\Omega_p}{4\pi} p_\perp \hat{\boldsymbol{p}} \Theta(\hat{\boldsymbol{p}}, \epsilon) & \\ \times \Big\{ - [\phi_{B1}(\hat{\boldsymbol{p}}, \epsilon, -\lambda \hat{\boldsymbol{p}}_\perp) + \phi_{B2}(\hat{\boldsymbol{p}}, \epsilon, \lambda \hat{\boldsymbol{p}}_\perp)] & \\ + [\phi_{B1}(\hat{\boldsymbol{p}}, \epsilon, \lambda \hat{\boldsymbol{p}}_\perp) + \phi_{B2}(\hat{\boldsymbol{p}}, \epsilon, -\lambda \hat{\boldsymbol{p}}_\perp)] \Big\}. & \end{aligned} \tag{B.36}$$

Bibliography

[1] D. Vollhardt and P. Wölfle, *The Superfluid Phases of Helium 3* (Dover, New York, 2013).

[2] E. M. Lifshitz and L. P. Pitaevskii, *Statistical Physics, Part 2* (Pergamon, Oxford, 1980).

[3] G. Baym and C. Pethick, *Landau Fermi-Liquid Theory* (Wiley, New York, 1991).

[4] L. D. Landau, Zh. Eksp. Teor. Fiz. **30**, 1058 (1956) [Sov. Phys. JETP **3**, 920 (1957)].

[5] L. D. Landau, Zh. Eksp. Teor. Fiz. **32**, 59 (1957) [Sov. Phys. JETP **5**, 101 (1957)].

[6] L. N. Cooper, Phys. Rev. **104**, 1189 (1956).

[7] A. L. Fetter and J. D. Walecka, *Quantum Theory of Many-Particle Systems* (McGraw-Hill, New York, 1971).

[8] A. J. Leggett, Rev. Mod. Phys. **47**, 331 (1975).

[9] J. Bardeen, L. N. Cooper, and J. R. Schrieffer, Phys. Rev. **106**, 162 (1957).

[10] J. Bardeen, L. N. Cooper, and J. R. Schrieffer, Phys. Rev. **108**, 1175 (1957).

[11] J. B. Ketterson and S. N. Song, *Superconductivity* (Cambridge, Cambridge, 1999).

[12] G. E. Volovik, *The Universe in a Helium Droplet* (Clarendon Press, Oxford, 2003).

[13] P. W. Anderson and P. Morel, Physica **26**, 671 (1960).

[14] P. W. Anderson and P. Morel, Phys. Rev. **123**, 1911 (1961).

[15] D. D. Osheroff, R. C. Richardson, and D. M. Lee, Phys. Rev. Lett. **28**, 885 (1972).

[16] R. Balian and N. R. Werthamer, Phys. Rev. **131**, 1553 (1963).

[17] W. J. Gully, D. D. Osheroff, D. T. Lawson, R. C. Richardson, and D. M. Lee, Phys. Rev. A **8**, 1633 (1973).

[18] V. Ambegaokar and N. D. Mermin, Phys. Rev. Lett. **30**, 81 (1973).

[19] V. Ambegaokar, P. G. deGennes, and D. Rainer, Phys. Rev. A **9**, 2676 (1974).

[20] J. W. Serene and D. Rainer, Phys. Rep. **101**, 221 (1983).

[21] A. L. Fetter, in *Quantum Statistics and the Many-Body Problem*, edited by S. B. Trickey, W. P. Kirk, and J. W. Dufty (Plenum Press, New York, 1975), pp. 127-138.

[22] D. Vollhardt, K. Maki, and N. Schopohl, J. Low Temp. Phys. **39**, 79 (1980).

[23] H. Kleinert, J. Low Temp. Phys. **39**, 451 (1980).

[24] J. V. Porto and J. M. Parpia, Phys. Rev. Lett. **74**, 4667 (1995).

[25] E. V. Thuneberg, S. K. Yip, M. Fogelström, and J. A. Sauls, Phys. Rev. Lett. **80**, 2861 (1998).

[26] W. P. Halperin, J. M. Parpia, and J. A. Sauls, Phys. Today **71**, 30 (2018).

[27] V. V. Dmitriev, A. A. Senin, A. A. Soldatov, and A. N Yudin, Phys. Rev. Lett. **115**, 165304 (2015).

[28] N. Zhelev, M. Reichl, T. S. Abhilash, E. N. Smith, K. X. Nguyen, E. J. Mueller, and J. M. Parpia, Nat. Commun. **7**, 12975 (2016).

[29] K. Aoyama and R. Ikeda, Phys. Rev. B **73**, 060504 (2006).

[30] A. L. Fetter, in *Progress in Low Temperature Physics* **X**, edited by D. F. Brewer (Elsevier, Amsterdam, 1986), pp. 1-72.

[31] O. V. Lounasmaa and E. Thuneberg, Proc. Natl. Acad. Sci. USA **96**, 7760 (1999).

[32] O. T. Ikkala, G. E. Volovik, P. J. Hakonen, Yu. M. Bunkov, S. T. Islander, and G. A. Kharadze, Pis'ma Zh. Eksp. Teor. Fiz. **35**, 338 (1982) [JETP Lett. **35**, 416 (1982)].

[33] P. J. Hakonen, M. Krusius, M. M. Salomaa, J. T. Simola, Yu. M. Bunkov, V. P. Mineev, and G. E. Volovik, Phys. Rev. Lett. **51**, 1362 (1983).

[34] M. M. Salomaa and G. E. Volovik, Phys. Rev. B **31**, 203 (1985).

[35] E. V. Thuneberg, Phys. Rev. B **36**, 3583 (1987).

[36] S. Autti, V. V. Dmitriev, J. T. Mäkinen, A. A. Soldatov, G. E. Volovik, A. N. Yudin, V. V. Zavjalov, and V. B. Eltsov, Phys. Rev. Lett. **117**, 255301 (2016).

[37] J. C. Wheatley, Rev. Mod. Phys. **47**, 415 (1975).

[38] D. M. Lee and R. C. Richardson, in *The Physics of Liquid and Solid Helium, Part 2*, edited by K. H. Bennemann and J. B. Ketterson (Wiley, New York, 1978), pp. 287-496.

[39] A. F. Borghesani, *Ions and Electrons in Liquid Helium* (Oxford University Press, Oxford, 2007).

[40] V. V. Dmitriev, Y. Kondo, J. S. Korhonen, M. Krusius, Yu. M. Mukharskiy, E. B. Sonin, and G. E. Volovik, Physica B **165 - 166**, 655 (1990).

[41] Y. Kondo, J. S. Korhonen, M. Krusius, V. V. Dmitriev, Y. M. Mukharsky, E. B. Sonin, and G. E. Volovik, Phys. Rev. Lett. **67**, 81 (1991).

[42] L. Landau, J. Phys. USSR **5**, 71 (1941).

[43] D. I. Bradley, S. N. Fisher, A. M. Guénault, R. P. Haley, C. R. Lawson, G. R. Pickett, R. Schanen, M. Skyba, V. Tsepelin, and D. E. Zmeev, Nat. Phys. **12**, 1017 (2016).

[44] E. V. Thuneberg, J. Low Temp. Phys. **122**, 657 (2001).

[45] H. Goldstein, C. P. Poole, and J. L. Safko, *Classical Mechanics*, 3rd ed. (Addison-Wesley, New York, 2002).

[46] M. Fogelström and J. Kurkijärvi, J. Low Temp. Phys. **98**, 195 (1995).

[47] M. A. Silaev, E. V. Thuneberg, and M. Fogelström, Phys. Rev. Lett. **115**, 235301 (2015).

[48] Y. Hasegawa, Prog. Theor. Phys. **73**, 1258 (1985).

[49] A. J. Leggett, Ann. Phys. (NY) **85**, 11 (1974).

[50] A. J. Leggett and S. Takagi, Ann. Phys. (NY) **106**, 79 (1977).

[51] K. Maki, Phys. Rev. B **11**, 4264 (1975).

[52] A. L. Fetter and J. D. Walecka, *Theoretical Mechanics of Particles and Continua* (McGraw-Hill, New York, 1980).

[53] W. F. Brinkman and H. Smith, Phys. Lett. A **53**, 43 (1975).

[54] G. B. Whitham, *Linear and Nonlinear Waves* (Wiley, New York, 1974).

[55] L. D. Landau and E. M. Lifshitz, *The Classical Theory of Fields*, 3rd ed. (Pergamon Press, Oxford, 1971).

[56] J. D. Jackson, *Classical Electrodynamics*, 3rd ed. (Wiley, New York, 1999).

[57] G. Arfken, *Mathematical Methods for Physicists*, 2nd ed. (Academic Press, New York, 1970).

[58] M. Abramowitz and I. A. Stegun, *Handbook of Mathematical Functions with Formulas, Graphs, and Mathematical Tables* (Dover, New York, 1965).

[59] N. Bleistein and R. A. Handelsman, *Asymptotic Expansions of Integrals* (Dover, New York, 1986).

[60] A. S. Borovik-Romanov, Yu. M. Bunkov, V. V. Dmitriev, and Yu. M. Mukharskii, Pis'ma Zh. Eksp. Teor. Fiz. **40**, 256 (1984) [JETP Lett. **40**, 1033 (1984)].

[61] I. A. Fomin, Pis'ma Zh. Eksp. Teor. Fiz. **40**, 260 (1984) [JETP Lett. **40**, 1037 (1984)].

[62] N. N. Bogoliubov, Zh. Eksp. Teor. Fiz. **34**, 58 (1958) [Sov. Phys. JETP **7**, 41 (1958)].

[63] G. Kieselmann and D. Rainer, Z. Phys. B **52**, 267 (1983).

[64] N. A. Greaves and A. J. Leggett, J. Phys. C **16**, 4383 (1983).

[65] A. F. Andreev, Zh. Eksp. Teor. Fiz. **46**, 1823 (1964) [Sov. Phys. JETP **19**, 1228 (1964)].

[66] D. I. Bradley, A. M. Guénault, R. P. Haley, G. R. Pickett, and V. Tsepelin, Annu. Rev. Cond. Mat. Phys. **8**, 407 (2017).

[67] M. Tinkham, *Introduction to Superconductivity* (McGraw-Hill, New York, 1996), Second Edition.

[68] E. V. Thuneberg, J. Kurkijärvi, and D. Rainer, J. Phys. C **14**, 5615 (1981).

[69] B. Ashauer, J. Phys. C **21**, 5129 (1988).

[70] L. D. Landau and E. M. Lifshitz, *Fluid Mechanics* (Pergamon Press, Oxford, 1987).

[71] G. K. Batchelor, *An Introduction to Fluid Dynamics* (Cambridge, London, 1967).

[72] S. N. Fisher, A. M. Guénault, C. J. Kennedy, and G. R. Pickett, Phys. Rev. Lett. **63**, 2566 (1989).

[73] S. N. Fisher, G. R. Pickett, and R. J. Watts-Tobin, J. Low Temp. Phys. **83**, 225 (1991).

[74] M. P. Enrico, S. N. Fisher, and R. J. Watts-Tobin, J. Low Temp. Phys. **98**, 81 (1995).

[75] M. P. Enrico and R. J. Watts-Tobin, J. Low Temp. Phys. **102**, 103 (1996).

[76] B. Ashauer, Ph.D. thesis, University of Bayreuth, 1989.

[77] J. Kurkijärvi and D. Rainer, in *Helium Three*, edited by W.P. Halperin and L.P. Pitaevskii (Elsevier, Amsterdam, 1990), pp. 313-352.

[78] K. Nagai, Y. Nagato, M. Yamamoto, and S. Higashitani, J. Phys. Soc. Jpn. **77**, 111003 (2008).

[79] A. Shelankov and M. Ozana, Phys. Rev. B **61**, 7077 (2000).

[80] M. Eschrig, Phys. Rev. B **80**, 134511 (2009).

[81] W. Zhang, J. Kurkijärvi, D. Rainer, and E. V. Thuneberg, Phys. Rev. B **37**, 3336 (1988).

[82] T. H. Virtanen and E. V. Thuneberg, *24th International Conference on Low Temperature Physics - LT24* AIP Conf. Proc. No. 850, (AIP, New York, 2006), p. 113.

[83] G. Floquet, Ann. Sci. Ecole Norm. Sup. **12**, 47 (1883).

[84] V. A. Yakubovich and V. M. Starzhinskii, *Linear Differential Equations with Periodic Coefficients* (Wiley, New York, 1975), Vols. 1 and 2.